

# **Manipulation and coherence of a two-electron logical spin qubit using GaAs double quantum dots**

A dissertation presented  
by

Sandra Elisabetta Foletti

to

The Department of Physics  
in partial fulfillment of the requirements  
for the degree of  
Doctor of Philosophy  
in the subject of

Physics

Harvard University  
Cambridge, Massachusetts

April 2010

© 2010 by Sandra Elisabetta Foletti  
All rights reserved.

Dissertation Advisor:

**Professor Amir Yacoby**

Author:

**Sandra Elisabetta Foletti**

Manipulation and coherence of a two-electron logical spin qubit using  
GaAs double quantum dots

## Abstract

Spin qubits have been considered promising candidates for quantum computation due to their expected long coherence times. In a solid state environment, such as GaAs, electrons confined to quantum dots interact with an ensemble of about a million nuclei through hyperfine interaction. The polarization of the nuclear bath fluctuates around a zero mean which was considered to be a serious obstacle towards extending the qubit's coherence time  $T_2$  beyond approximately 1 microsecond. In addition, the inhomogeneous coherence time  $T_2^*$  has been measured to be in the range of 10 ns, ultimately limiting the fidelity of the qubit.

Here we explore, using two electron logical spin qubits in GaAs, the possibility of achieving universal control of the qubit's state and of prolonging the qubits coherence times. Our main results include:

- Dynamical polarization of the nuclei to reach local magnetic field gradients up to 200 mT.
- The use of local field gradients to perform universal quantum control and quantum state tomography of the qubit.
- The use of a quantum feedback mechanism intrinsic to our system in order to pump

the nuclear bath and simultaneously narrow its distribution, thereby reducing the amplitude of its stochastic fluctuations that lead to inhomogeneous dephasing.

- Using decoupling techniques well established in NMR we show that we can extend the homogeneous coherence time of the qubit by three orders of magnitude compared to previous reports.
- Unraveling the contribution of spin-orbit coupling to the nuclear dynamic polarization using a pumping scheme that never exchanges electrons with the reservoir. The modulation of the polarization efficiency by the nuclear Larmor precession period is interpreted as arising from the coherent interplay of spin-orbit and hyperfine interaction.

# Contents

Abstract . . . . .	iii
Table of Contents . . . . .	v
List of Figures . . . . .	viii
Acknowledgments . . . . .	x
<b>1 Introduction</b>	<b>1</b>
1.1 Historical introduction . . . . .	1
1.2 The physical implementation of a quantum computer . . . . .	3
1.3 Outline of this thesis . . . . .	4
<b>2 Background</b>	<b>7</b>
2.1 Quantum computation . . . . .	7
2.1.1 Quantum two-level system . . . . .	8
2.1.2 Requirements for a scalable quantum computer . . . . .	10
2.1.3 Interactions with the environment . . . . .	11
2.2 Quantum dots . . . . .	12
2.2.1 GaAs two dimensional electron gas . . . . .	12
2.2.2 General introduction to quantum dots . . . . .	14
2.2.3 Double quantum dots . . . . .	16
2.2.4 The spin configurations at the (0,2) to (1,1) charge transition . . . . .	18
2.2.5 Determining the charge configuration with a charge sensing technique	22
2.3 Two-electron spin qubit . . . . .	24
2.3.1 Motivation . . . . .	24
2.3.2 Electron-nuclei hyperfine interaction . . . . .	25
2.3.3 Qubit manipulations . . . . .	27
2.3.4 Dynamic nuclear polarization . . . . .	29
2.3.5 Spin flip due to spin-orbit coupling . . . . .	31
2.3.6 Preparation, manipulation and read-out: a summary . . . . .	33
2.4 Decoherence . . . . .	35
2.4.1 Local magnetic field changes due to hyperfine interaction . . . . .	35
2.4.2 Local magnetic field changes due to dipole-dipole interaction . . . . .	36
2.4.3 Determining the ensemble coherence time $T_2^*$ . . . . .	37
2.4.4 Determining the coherence time $T_2$ . . . . .	38
<b>3 Device fabrication</b>	<b>42</b>
3.1 Defining the conducting region . . . . .	42
3.2 Ohmic contacts . . . . .	43
3.3 E-beam and optical gates . . . . .	45

3.4	Few-electron quantum dot design . . . . .	46
3.5	Sample stability . . . . .	48
<b>4</b>	<b>Experimental set-up and procedures</b>	<b>50</b>
4.1	Set-up in the Frossati dilution refrigerator with high frequency gate lines . . . . .	51
4.1.1	DC wiring . . . . .	51
4.1.2	High frequency gate lines . . . . .	53
4.1.3	The cold finger . . . . .	56
4.2	Set-up in the Oxford dilution refrigerator with high frequency gate lines and RF read-out . . . . .	59
4.2.1	DC wiring . . . . .	59
4.2.2	High frequency gate lines . . . . .	60
4.2.3	RF read-out . . . . .	63
4.2.4	The cold finger . . . . .	72
4.3	Data acquisition programs . . . . .	72
<b>5</b>	<b>Universal quantum control of two-electron spin quantum bits using dynamic nuclear polarization</b>	<b>74</b>
5.1	Introduction . . . . .	75
5.2	Description of the system . . . . .	76
5.3	Pumping schemes . . . . .	79
5.3.1	$S$ -pumping scheme . . . . .	79
5.3.2	$T_+$ -pumping scheme . . . . .	79
5.4	Measurement scheme . . . . .	80
5.5	Steady state nuclear magnetic field gradients . . . . .	82
5.5.1	Gradient build-up with and $S$ and $T_+$ pumping . . . . .	82
5.5.2	Loss of contrast . . . . .	83
5.6	Measurement of the average local magnetic field . . . . .	85
5.6.1	Tuning . . . . .	88
5.7	State tomography . . . . .	89
5.7.1	Model for the analysis of the tomography data . . . . .	92
5.8	Conclusions . . . . .	94
<b>6</b>	<b>Enhancing the coherence of Spin Qubits by Narrowing the Nuclear Spin Bath Using a Quantum Feedback Loop</b>	<b>96</b>
6.1	Introduction . . . . .	97
6.2	Description of the system . . . . .	99
6.3	Probing the local nuclear magnetic field gradient . . . . .	101
6.4	$S$ and $T_+$ pumping cycles . . . . .	101
6.5	Local magnetic field fluctuations . . . . .	103
6.6	Feedback schemes . . . . .	104
6.6.1	Software feedback . . . . .	104
6.6.2	Pulse feedback . . . . .	104
6.6.3	Measurement of the pump rates . . . . .	105
6.7	Stable gradients . . . . .	108
6.8	Conclusions . . . . .	109
<b>7</b>	<b>Long coherence of electron spins coupled to a nuclear spin bath</b>	<b>110</b>

7.1	Introduction . . . . .	111
7.2	Description of the system . . . . .	113
7.3	Experimental procedures . . . . .	114
7.4	Hahn-echo measurements . . . . .	116
7.4.1	Low magnetic field measurements . . . . .	116
7.4.2	High magnetic field measurements . . . . .	118
7.4.3	Fit to the data . . . . .	118
7.4.4	Fit procedures . . . . .	119
7.5	Pulse design and optimization . . . . .	120
7.5.1	Pulse design . . . . .	120
7.5.2	Pulse optimization . . . . .	123
7.6	CPMG pulses . . . . .	125
7.7	Normalization and background measurements . . . . .	127
7.8	Conclusions . . . . .	130
<b>8</b>	<b>Observation of dynamic nuclear polarization using a single pair of electrons</b>	<b>131</b>
8.1	Introduction . . . . .	132
8.2	Description of the system . . . . .	134
8.3	Measurement of the $S-T_+$ degeneracy point . . . . .	136
8.4	Dynamic nuclear polarization using a single pair of electrons . . . . .	138
8.4.1	Total measurement time dependence . . . . .	139
8.4.2	Variation of the probing time . . . . .	140
8.5	Conclusions . . . . .	141
<b>A</b>	<b>Double dot fabrication recipe</b>	<b>143</b>
<b>B</b>	<b>Double dot tuning procedure</b>	<b>147</b>

# List of Figures

2.1	Bloch sphere . . . . .	9
2.2	2 Dimensional Electron Gas . . . . .	13
2.3	Single quantum dots . . . . .	14
2.4	Double quantum dots . . . . .	16
2.5	Charge transition . . . . .	19
2.6	Energy diagram . . . . .	20
2.7	Spin blockade . . . . .	21
2.8	Bloch sphere in the $\{ S\rangle,  T_0\rangle\}$ basis . . . . .	28
2.9	Spin-orbit interaction . . . . .	33
2.10	Measurement scheme . . . . .	34
2.11	Measurement of $T_2^*$ . . . . .	38
2.12	CP and CPMG pulse schemes . . . . .	40
3.1	Photolithography mask . . . . .	44
3.2	Processing scheme . . . . .	46
3.3	SEM image of the sample . . . . .	47
3.4	Different quantum dot designs . . . . .	48
4.1	Pictures of the Frossati dilution refrigerator wiring . . . . .	52
4.2	Wiring scheme of the Frossati dilution refrigerator . . . . .	54
4.3	Cold finger of the Frossati dilution refrigerator . . . . .	57
4.4	Rotatable sample holder . . . . .	58
4.5	Pictures of the MX50 dilution refrigerator wiring . . . . .	61
4.6	Wiring scheme of the MX50 dilution refrigerator . . . . .	62
4.7	MX50 dilution refrigerator electronics . . . . .	64
4.8	Details of the MX50 dilution refrigerator wiring . . . . .	66
4.9	Frequency response of the tank circuit . . . . .	68
4.10	Sapphire strip-line . . . . .	69
4.11	MX50 cold finger . . . . .	71
5.1	Pump and measurement schemes . . . . .	78
5.2	Build-up of a gradient with two different pumping cycles . . . . .	81
5.3	Contrast loss as a function of polarization . . . . .	84
5.4	Calibration of the $S-T_+$ transition shift . . . . .	85
5.5	Comparison of the gradient and the average nuclear field . . . . .	86
5.6	Two different tuning conditions . . . . .	89
5.7	State tomography and universal gate . . . . .	90
5.8	Pulse shapes extracted from fits to the tomography data . . . . .	91

6.1	Basic principles of the experiment . . . . .	98
6.2	Polarization rates . . . . .	102
6.3	$T_2^*$ enhancement . . . . .	106
7.1	Qubit control . . . . .	115
7.2	Echo amplitude . . . . .	117
7.3	Pulse design . . . . .	122
7.4	Pulse optimization . . . . .	124
7.5	CPMG decoupling experiments with 6, 10 and 16 $\pi$ -pulses at $B_{ext} = 0.4$ T	126
7.6	Background subtraction . . . . .	129
8.1	Description of the system . . . . .	133
8.2	Pump cycle without reload . . . . .	137
8.3	Detailed measurement of the oscillations . . . . .	140
8.4	Variation of the probing time . . . . .	141
B.1	Tuning procedure . . . . .	149

# Acknowledgments

Many people contributed to the completion of this work and first amongst all my advisor, Amir Yacoby. Amir is an excellent physicist, who has a good intuition for the pursuit of interesting and challenging long term goals and always has a careful and critical look at data and theories. I thank him for giving me the chance to work in his group and for his guidance during the past five years. I thank Amir, Bert Halperin and Charlie Marcus for serving on my thesis committee.

I worked closely with Merav Dolev at the beginning of my PhD and with Hendrik Bluhm towards the end of it: I thank them for their hard work necessary to start this new project and subsequently use the tools to explore interesting physics. I also thank Jeff Miller for introducing me to the secrets of fabrication.

A good and collaborative atmosphere within the group has always been very important to me. I thank Basile Verdene, Yoav Gordin, Tali Dadosh, Hadar Steinberg, Amit Finkler, Nitzan Akerman, Gilad Barak, Vivek Venkatachalam, Sean Hart, Mike Grinolds, Patrick Maletinsky, Sungkun Hong, Monica Allen, Jonah Waissman, Mikey Shulman, Thomas Weitz and Ben Feldman for their contributions. Special thanks go to Jens Martin, who was there from the lab's very beginning and is an invaluable source of knowledge we all turn to so many times.

Special thanks go to Alessandro Romito, Eros Mariani, Hansres Engel, Izhar Neder, Mark Rudner and Jacob Krich whose help and discussions to understand the theory behind my work (and not only) was invaluable. I am grateful for the time I could spend with them.

Additionally, I thank all fellow students and post-docs I interacted with for discussions and useful information exchanges.

I would like to thank Sheila Ferguson for all her assistance, help and admirable patience even when things became urgent.

All our work could not proceed as it did without the help and support from the Sub-micron Center team led by Moty Heiblum and all the people with equivalent counterparts at the physics department at Harvard. I would like to thank Diana Mahalu, Olga Raslin, Vladimir Umansky, Roby Tsabary, Hadas Shtrikman, the late Michael Shneiderman, Yoram Rotblat, Yossi Rolnik, the three helium musketeers Yossi Gal, Solomon Shpiner and Ronen Havkin, Carolyn Moore, Danielle Reuter, James Gotfredson, Jess Martin, Kelly Labrecque and Noah Clay and his whole team.

During the semester I spent teaching I met many people with different backgrounds that made the experience something special. I am grateful to Melissa Franklin, Andrew Berry and Logan McCarty for sharing so much of their knowledge and experience with me and my fellow TFs Eleanor Millman, Yundan Pi, Jacob Sanders and Daniel Rosenberg for their hard work. I would like to thank also Rob Hart, Angela Allen, Jan Ragusa and Carol Davis for their help and support.

I would like to thank all friends in Israel and the US for the dinners, the parties and more in general for the pleasant time we spent together: I will miss you but I know we will keep in touch despite the distances. Many thanks go to all the very good friends and family members back in Europe who always supported me and can still stand me after all these

years of never being there and never having enough time.

My most special thank you goes to Michele, without whom this would have been a much harder journey. I thank him for his patience, help and everything I forgot to mention, or maybe I should just summarize it in his own words “for being the best husband ever” ;-).

# Chapter 1

## Introduction

### 1.1 Historical introduction

Since the 1970-80's quantum computation and information processing has emerged as a new paradigm of physics and computer science. The first pioneering ideas of quantum computation and its use were put forward by Richard Feynman, Steve Wiesner and David Deutsch [1]. In his famous lecture at an MIT workshop in 1981 about "Simulating physics with computers" [2] Richard Feynman posed the questions whether quantum mechanical systems could be successfully simulated with computers that were themselves quantum mechanical. The problem is that for a classical computer, the computation time grows exponentially with the number of simulated particles  $N$ , rather than in a polynomial fashion, restricting the simulation of large scale problems [3].

In the early 1970s Steve Wiesner, a physicist who was no longer actively working in academia, but nonetheless thinking of interesting problems, wrote a manuscript entitled "On conjugate coding" [1], where he explored the implications of simple quantum mechanical laws for secrecy. He was the first one to address the relation between quantum mechanical

laws and cryptography. In the 1980's Charles Bennett and Gilles Brassard turned Wiesner's seminal ideas into a theory that explains the distribution of a quantum key [4].

The first person to closely examine the concept of a quantum bit and the logic system related to it is David Deutsch. The fundamental carrier of quantum information, the qubit, is a quantum mechanical state  $|\Psi\rangle = \alpha|0\rangle + \beta|1\rangle$  that is a superposition of two basis states  $|0\rangle$  and  $|1\rangle$  (where  $\alpha$  and  $\beta$  are complex numbers), contrary to classical bits that can assume only two values (either 0 or 1). Deutsch recognized that quantum computation opened the way to new logic gates, such as gates that take two state and create a superposition of them: an entangled state. A state  $|\Psi\rangle$  of two qubits,  $a$  and  $b$ , is said to be entangled if it cannot be written as a tensor product of a state of qubit  $a$  and a state of qubit  $b$ , i.e.  $|\Psi\rangle \neq |\Psi_a\rangle \otimes |\Psi_b\rangle$  [5].

These early thinkers were driven by the thought that quantum mechanical computers should be more powerful than classical ones since classical mechanics is a special limit of quantum mechanics. However quantum computers are not more efficient in performing just any task and require well tailored algorithms. The key point is related to the measurement of a quantum system: a quantum bit can be in a superposition state of the basis states  $|0\rangle$  and  $|1\rangle$ , but a measurement returns the equivalent of one bit of information. It is thus non-trivial to implement algorithms that make use of the increased computational power of a quantum computer and simultaneously allow for the information to be extracted. The discovery of several quantum mechanical algorithms has shown that it can be done. The problem of cracking encrypted codes, for example, would take very long times with a classical computer, but could be solved very efficiently using a quantum mechanical algorithm discovered by Shor in 1994 [6]. The time required to perform Shor's algorithm scales polynomially with the number of digits of the prime number to be factorized, while the time required for the

best classical algorithms scales exponentially with the number of digits. An example of another quantum algorithms that can outperform its classical counterparts is Lov Grover's algorithm for searching a database [7].

To Feynman, the simulation of real quantum mechanical systems with a quantum computer looked like a wonderful problem, because it seemed intractable [2]. The implementation of a quantum computer is indeed difficult and many different approaches are been taken by the scientific community to solve it. In the following section a brief introduction to the physical implementation of a quantum computer is given, followed by the outline of this thesis.

## 1.2 The physical implementation of a quantum computer

The requirements for the physical implementation of a quantum bit are rather conflicting. On one hand, the qubit needs to be reliably prepared, accessed for manipulation and read out. On the other hand, it should be well isolated from the environment in order to avoid the destruction of the delicate quantum state with the subsequent loss of information. Moreover, for a scalable implementation of a quantum computer, many bits need to work in concert.

Over the past decade many physical realizations have been proposed and studied. These include for example atoms in optical lattices [8], nuclear spins of molecules in solution [9], nitrogen vacancies in diamond [10], Josephson junctions [11] and many more. In 1998 Loss and DiVincenzo [12] theoretically suggested using the spin of a single electron as the building block of a quantum computer. This is a very interesting approach considering the conflicting requirements mentioned above: the information is encoded in the magnetic moment of an electron which is small and interacts weakly with the environment, but at

the same time can be manipulated using electric fields.

For the realization of this proposal, the confinement and the manipulation of single electrons are necessary. Quantum dots are small islands where single electrons can be isolated: they are characterized by discrete energy spectra analogous to atomic spectra. These structures, often engineered within a semiconductor, are accordingly referred to as artificial atoms. Their advantage over atoms is the tunability and control of various parameters that are otherwise fixed by nature. An important disadvantage is the difference in environments: atoms can be isolated from their environment, whereas electrons in quantum dots are embedded in a solid-state environment where interactions are hard to avoid.

In this thesis a slightly modified version of the spin quantum bit is studied: a logical spin qubit where the information is encoded in the  $m_z=0$  spin states, the singlet and the triplet state of two electrons confined in a double quantum dot. The advantage over the single spin realization is that the two-electron spin qubit is protected against external uniform magnetic field fluctuations and its manipulation can be done electrostatically in subnanosecond time scales. For both the single and two-electron spin qubits the major environmental challenge are the nuclear spins in the underlying host lattice. Uncontrolled interactions between the electrons and the nuclei can pose significant problems to the use of these devices as building blocks of a quantum computer: understanding and controlling the interactions is thus of major importance.

### 1.3 Outline of this thesis

When our group entered the field, the major concern to using GaAs based qubits was the unavoidable presence of the hyperfine interaction with the surrounding nuclei limiting the coherence time of the qubit. On the other hand, there was the feeling that nuclear spins

could be a resource for the implementation of fast operations, as pumping of the nuclear lattice had already been proven possible. Moreover, it was proposed that the different time scales for the electronic and nuclear dynamics would allow dynamic decoupling techniques common in NMR for large atomic ensembles.

The ultimate question, whether two-electrons spin states in double quantum dots are viable candidates for the implementations of qubits requires to prove manipulations of the qubit around arbitrary Bloch sphere axes and the possibility of implementing a sufficiently large number of gate operations within the coherence time necessary for error correction. It also implies studying the fundamental interactions between single electrons and their nuclear bath environment.

Chap. 2 reviews the necessary theoretical background for the understanding of the experiments presented in this work, Chap. 3 explains the sample fabrication procedures and Chap. 4 describes in details the setups we built and used for the experiments presented in this thesis.

Full quantum control of the qubit with in-situ generated gradients in the local magnetic field is presented in Chap. 5. Using dynamic nuclear polarisation, we show that we can induce local magnetic field gradients up to 200 mT for the first time in lateral double quantum dots. This gradient, together with previously shown rapid exchange of the two electrons [13], allows us to perform arbitrary rotations with nanosecond time scales. We demonstrate this by performing quantum state tomography.

Pumping of the nuclear polarization with a quantum feedback loop is presented in Chap. 6. We modify the dynamic nuclear polarization pulse cycle previously presented and integrate a quantum feedback loop to condition the nuclear polarization rate on a quantum limited measurement of the local nuclear magnetic field gradient performed by the qubit

itself. With this new pulse cycle, we show an effective narrowing of the nuclear distribution and an enhancement of  $T_2^*$  by nearly one order of magnitude.

Measuring the coherence time  $T_2$  is the subject of Chap. 7. We present Hahn-echo measurements at magnetic fields ranging from 50 to 700 mT. At low magnetic fields, the Hahn-echo time traces show collapses and revivals associated with the Larmor precession of the nuclear polarization, in agreement with recent theoretical work [14]. Using Carr-Purcell-Meiboom-Gill pulse sequences, we measure coherence times of several hundreds of microseconds.

In Chap. 8, we present measurements showing dynamical nuclear polarisation achieved with a single pair of electrons. This measurement shows for the first time that transitions between a singlet and a triplet  $T_+$  state are not mediated by hyperfine coupling alone. We observe a dependence of the dynamical nuclear polarization rate on the Larmor precession period of the nuclei: theoretical work has shown that effects of this type can arise from a coherent interplay between hyperfine and spin-orbit interaction.

# Chapter 2

## Background

This chapter provides an introduction to the system used for our physical implementation of a qubit, where the information is encoded in the spin states with  $m_z = 0$  of two electrons confined in a double quantum dot. We provide the background information necessary for the understanding of the experimental work presented in Chap. 5 to 8. We start with a brief introduction to quantum computation, followed by an introduction of the quantum dot properties and our spin qubit. In the second part of the chapter we present how the qubit and its interaction with the environment can be manipulated.

### 2.1 Quantum computation

The work presented in this thesis explores one particular implementation of a quantum bit. Before diving into the theory related to this particular implementation, we give a brief introduction to the general properties of a qubit and the requirements that a system needs to fulfill in order to be considered as a viable candidate for the implementation of a quantum computer.

### 2.1.1 Quantum two-level system

In classical computers information is encoded in two-level systems that can be either in a state 0 or in a state 1. One can, for example, think of a switch that is either closed (0) or open (1). In quantum computers, information is stored in a quantum two-level system with two distinguishable eigenstates. These could be two different energy levels of an atom, the two different spin states of a spin 1/2 particle or the two different polarizations of a photon [15]. The most generic state  $|\Psi\rangle$  is a linear combination (or superposition) of the two basis states  $|0\rangle$  and  $|1\rangle$ :

$$|\Psi\rangle = \alpha|0\rangle + \beta|1\rangle \quad (2.1)$$

where  $\alpha$  and  $\beta$  are in general complex numbers and  $|\alpha|^2 + |\beta|^2 = 1$ . This allows us to rewrite eq. (2.1) in the following way [16]:

$$|\Psi\rangle = \cos \frac{\theta}{2} |0\rangle + e^{i\varphi} \sin \frac{\theta}{2} |1\rangle,$$

with  $\theta, \varphi$  real numbers. This way of expressing the wave function of a generic state  $|\Psi\rangle$  is useful for a geometrical visualization that will be largely used in this thesis. The two angles  $\theta$  and  $\varphi$ , uniquely define any point on a unit three dimensional sphere known as the Bloch sphere (shown in Fig. 2.1).

We now need to know two more ingredients: how the state  $|\Psi\rangle$  evolves in time, and what form the Hamiltonians must have to implement arbitrary manipulations (i.e. gate operations). Any unitary operation on state  $|\Psi\rangle$  is a quantum gate operation which corresponds to a controlled rotation around specific axes within the Bloch sphere. The evolution of a state  $|\Psi\rangle$  between time  $t_0$  and a later time  $t$  is given by:

$$|\Psi(t)\rangle = U(t - t_0)|\Psi(t_0)\rangle \quad (2.2)$$

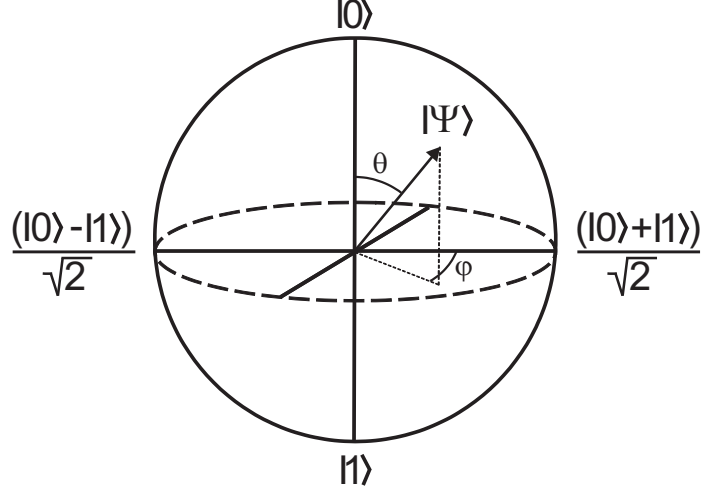


Figure 2.1: Bloch sphere representation of a generic state  $|\Psi\rangle = \alpha|0\rangle + \beta|1\rangle$ .

where the time evolution operator  $U(t - t_0)$  solves the Schrödinger equation:

$$i\hbar \frac{d}{dt} U(t - t_0) = H(t)U(t - t_0)$$

To implement gate operations, one can evolve  $|\Psi\rangle$  under the correct Hamiltonian for a given time  $\delta t$ , because the time evolution operator is also a unitary operation. For instance

$$H = \begin{pmatrix} -\frac{E}{2} & 0 \\ 0 & \frac{E}{2} \end{pmatrix} = -\frac{E}{2}\sigma_z$$

generates rotations around the  $z$ -axis. Here,  $U(t) = \exp\left\{\frac{iEt}{2\hbar}\sigma_z\right\} = e^{\frac{iEt}{2\hbar}} \left[|0\rangle\langle 0| + e^{-\frac{iEt}{\hbar}}|1\rangle\langle 1|\right]$ ,

$\sigma_{x,y,z}$  are the Pauli matrices, and

$$|\Psi(\delta t)\rangle = e^{i\frac{E\delta t}{2\hbar}} \left[ \cos\frac{\theta}{2}|0\rangle + e^{i(\varphi - \frac{E\delta t}{\hbar})} \sin\frac{\theta}{2}|1\rangle \right],$$

is a new state rotated around  $z$  by an angle  $-\frac{E\delta t}{\hbar}$ : the overall phase coefficient  $\exp\{i\frac{E\delta t}{2\hbar}\}$  is irrelevant for the calculation of the physical quantities and it can be absorbed by the energy shift  $H \rightarrow H + \frac{E}{2}$ .

Assume now we turn on an *additional* interaction  $H' = \Delta \cdot \sigma_x$ : the rotation axis points along  $\Delta\hat{\mathbf{x}} - \frac{E}{2}\hat{\mathbf{z}}$  and precession around that axis occurs at a rate  $f = \frac{1}{\hbar}\sqrt{4\Delta^2 + E^2}$ .

### 2.1.2 Requirements for a scalable quantum computer

The requirements for the physical implementation of a quantum computer are clearly outlined by the DiVincenzo criteria. We give a brief overview of these criteria mainly following [15]:

- *A scalable physical system with well characterized qubits*

As introduced in the previous section the qubit is a two level system that can be physically implemented in various systems. In order to characterize this qubit its physical parameters, such as the energy eigenstates, the interaction with other qubits, and the interaction with the environment must be well known.

- *The ability to initialize the state of the qubit to a simple fiducial state*

There are two reasons are behind this criterion. First, the registers should be initialized to a known state before starting a computation. Second, quantum error correction requires a continuous supply of qubits in a low entropy state, such as the  $|0\rangle$  state. Discussion of error correction is beyond the scope of this thesis and will not be explored further.

- *A universal set of quantum gates*

A quantum gate is specified as a unitary transformation  $U$  acting on a qubit, and a quantum algorithm is a sequence of unitary transformations. A set of quantum gates is sufficient to implement any algorithm and it includes all single qubit operations (that we have seen can be implemented by controlling two axes of rotation in the Bloch sphere) and one two-qubit gate (e.g. the controlled NOT (cNOT) gate).

- *A qubit specific measurement capability*

It must be possible to read out the final state after the computation has been per-

formed.

- *Decoherence time, much longer than the gate operation time*

The coherent dynamics of a quantum system (in this specific case the qubit) in contact with its environment is characterized by the decoherence time. Roughly speaking, the decoherence time is the time it takes before the qubit state  $|\Psi\rangle = \alpha|0\rangle + \beta|1\rangle$  is transformed into the mixed state represented by the operator  $\rho = |\alpha|^2|0\rangle\langle 0| + |\beta|^2|1\rangle\langle 1|$  and classical behavior takes over. The required length of the decoherence time is system specific and needs to be defined with respect to the time required to implement a single qubit gate. Quantum error correction has been proven to be possible [17, 18] and can be successful if the decoherence time is long enough to allow an order of magnitude of  $10^4$  gate operations (the number can vary depending on the architecture).

### 2.1.3 Interactions with the environment

Uncontrolled interactions with the environment lead to loss of information through relaxation and decoherence processes. If perturbations which are random in time can couple to the system, the phase relation between states  $|0\rangle$  and  $|1\rangle$  is lost after some time, and eq. (2.2) is no longer applicable.

Following the nomenclature introduced for NMR experiments [19] we introduce the relevant time scales:

1. The energy relaxation time  $T_1$  is the time it takes for an excited state to relax to the ground state.
2. The coherence time  $T_2$  is the time after which a quantum superposition loses its phase memory.

3. The ensemble coherence time  $T_2^*$  is the time after which coherence is lost when taking an averaged measurement over an ensemble of qubits, where each qubit interacts with a slightly different environment, or when averaging over time, where for each repetition of the same measurement the qubit interacts with a slightly different environment.

## 2.2 Quantum dots

As our experiments are oriented towards the study of electron spins as a two-level system for quantum computation, we need a structure that allows us to isolate and manipulate single electrons. Quantum dots are structures where electrons are confined in all three spatial directions and charge and spin configurations can be controlled. For the experiments presented in this thesis, quantum dots are realized in a heterostructure of GaAs/AlGaAs that naturally provides confinement in the  $z$ -direction, and added electrostatic gates that provide electrostatic confinement in the  $x$  and  $y$ -directions.

### 2.2.1 GaAs two dimensional electron gas

The wafer used for the fabrication of the samples is a heterostructure of GaAs and AlGaAs grown with molecular beam epitaxy (MBE). The two material have nearly the same lattice constant, which minimizes the lattice mismatch at the interface. As shown in Fig. 2.2, the substrate is a GaAs wafer on which a superlattice is first grown. The role of this superlattice is to reduce the propagation of defects present in the substrate [20]. After this subsequent layers of GaAs/AlGaAs/GaAs are grown. The AlGaAs layer includes a uniform doping stage [21] that is 60 nm away from the interface between the two materials: this particular kind of doping is known as *modulation doping*. Due to the bandgap configuration (AlGaAs has a larger bandgap than GaAs) charge carriers induced by the dopants accumulate at

the interface of the two materials. The triangular well (about 10 nm wide) that forms at the interface confines the electrons in the  $z$ -direction and at low temperatures only the lowest mode is populated. The electrons are thus only free to move in the  $x$  and  $y$ -direction (therefore called two dimensional electron gas (2DEG)). There are various advantages in choosing modulation doping. Placing the donors at a distance from the actual 2DEG decreases scattering: the potential fluctuations of the donor layer are smoothed out since the average distance between donors ( $\approx 3$  nm) is smaller than the distance between the donor layer and the 2DEG (here  $\approx 60$  nm) [22]. By varying the distance between the interface and the donor layer, the density of the 2DEG can be adjusted to the desired value [20].

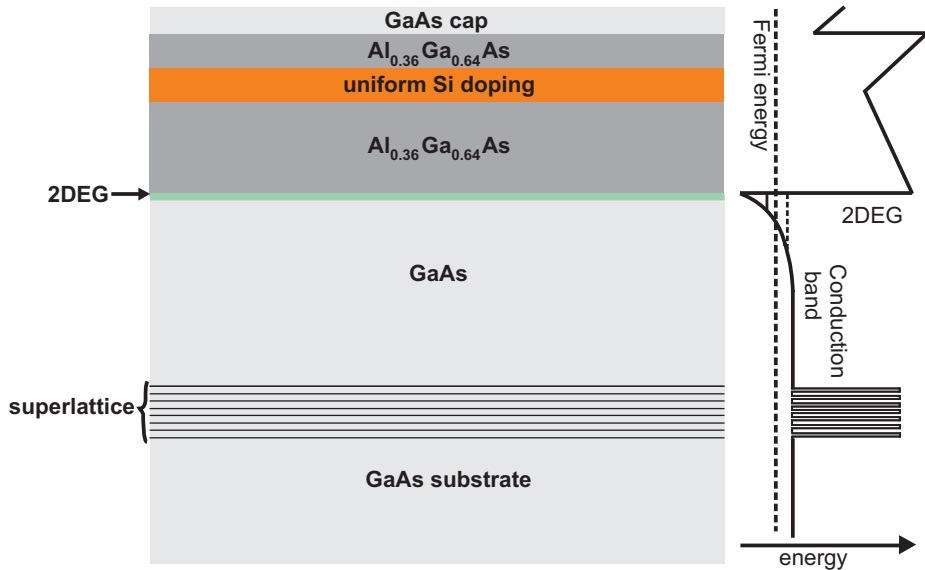


Figure 2.2: Schematic representation of a GaAs/AlGaAs heterostructure employed for our experiments. On a GaAs substrate a superlattice, a sequence of GaAs/Al<sub>0.36</sub>Ga<sub>0.64</sub>As, a doping layer, another layer of Al<sub>0.36</sub>Ga<sub>0.64</sub>As and a capping layer are grown. A two dimensional electron gas (2DEG) forms at the interface between GaAs and AlGaAs, where the conduction band dips below the Fermi energy. Adapted from [22].

## 2.2.2 General introduction to quantum dots

Quantum dots with many electrons ( $\approx 100$ ) were first studied in the early 1990's [23] and then further developed to be able to reach the single electron regime [24]. Few-electron quantum dots have dimensions on the order of 100 nm, and are defined in GaAs 2DEGs via electrostatic confinement given by metal gates evaporated on the wafer surface (for fabrication details see Chap. 3). A quantum dot can be schematically represented as an island coupled capacitively ( $C_L$  and  $C_R$ ) and through tunnel barriers ( $R_L$  and  $R_R$ ) to two leads and only capacitively to a *plunger gate*, as shown in Fig. 2.3a.

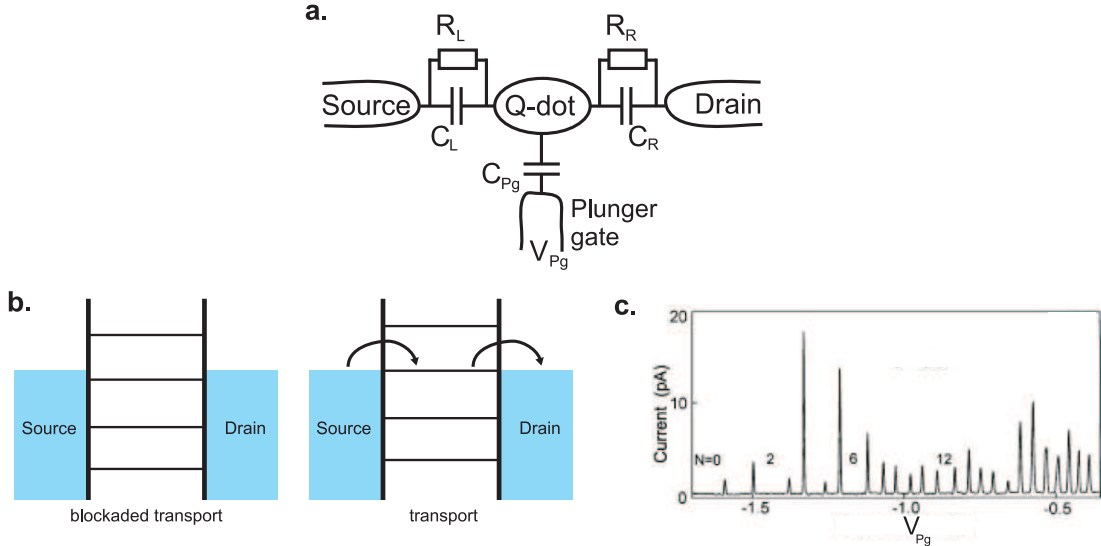


Figure 2.3: a) Schematic view of a quantum dot. The island is coupled capacitively and through tunnel barriers to source and drain, as well as only capacitively to a plunger gate. b) When changing the voltage on the plunger gate the energy levels inside the dot are shifted and electrons can tunnel through the dot when the dot's electrochemical potential is aligned with the chemical potential of the leads (giving a peak in conductance). c) Measurement of the current through a quantum dot as a function of the voltage on the plunger gate.  $N$  is the number of electrons confined in the quantum dot. Adapted from [25].

In order to see effects of the discrete nature of charge a few requirements must be fulfilled. The charging energy to add an excess charge to an otherwise neutral island with

total capacitance  $C$  must be larger than the thermal energy

$$E_c = e^2/C \gg kT \quad (2.3)$$

in order to avoid tunneling of thermally excited electrons through the barrier. Since the capacitance scales with the dimension of the island, the charging energy is inversely proportional to the size of the dot. For GaAs structures with dimensions on the order of tens of nm, the charging energy is typically 1 meV ( $\approx 10$  K).

A second condition that must be fulfilled is that the charge in the dot can only change by the electron unit charge [26] (the electron can thus be found either in one of the leads or in the dot). This condition is realized when the quantum fluctuations in the number of electrons is much smaller than 1 over the time scale of the measurement (roughly the electron charge divided by the current) [27], i.e. the total number of electrons  $N$  is a good quantum number. This can be achieved for a sufficiently large tunnel resistance. The argument is usually presented in the following way: the typical time to charge and discharge the dot is  $\Delta t = R_t C$ , where  $R_t$  the resistance of the tunnel barrier between the dot and the leads. Using the Heisenberg uncertainty relation  $\Delta E \Delta t > h$ , imposing the energy uncertainty  $\Delta E$  to be smaller than the charging energy  $E_c = e^2/C$  and knowing that  $\Delta t = R_t C$ , we find that  $R_t$  must be larger than the resistance quantum  $R_Q = h/e^2$  (where  $h$  Plank's constant and  $e$  the electron charge).

In addition to the charging energy, a discrete energy spectrum is induced when the lateral confinement is comparable to the electron wavelength. Because the qubit initialization relies on the presence of levels with separation larger than  $kT$  we select typical lithographic dimensions of the order of the Fermi wavelength in bulk GaAs, approximately 50 nm.

The plunger gate allows us to shift the energy levels of the dot with respect to the source and drain potentials. Every time the dot's electrochemical potential lines up with

the chemical potential of the leads, an electron can enter into (or exit) the dot (see Fig. 2.3b).

The plunger gate is thus used to change the charge state of the dot (i.e. the number of electrons).

### 2.2.3 Double quantum dots

Our qubit implementation requires double quantum dot structures. Similarly to the previous section, we schematically represent the double dot as two islands each coupled to one lead through a tunnel barrier and capacitively coupled to two different plunger gates. The new element here is an interdot coupling, given by a tunnel barrier, represented by the tunnel resistor  $R_M$  and a mutual capacitance  $C_M$  [28], as indicated schematically in Fig. 2.4a.

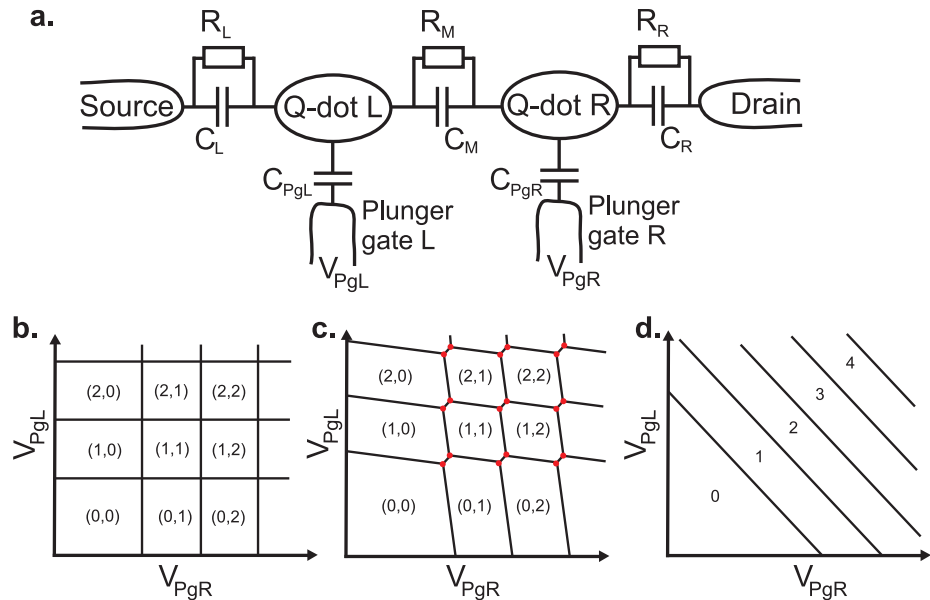


Figure 2.4: a) Schematic view of a double quantum dot. The islands are coupled through tunnel barriers to source or drain and to each other, as well as only capacitively to a plunger gate each. b) Charge stability diagram of a double dot with zero inter-dot coupling. c) Charge stability diagram of a double dot with intermediate inter-dot coupling. The red dots indicate points in gate space where current between source and drain can flow since the electrochemical potentials of the source, the drain and the two dots are aligned. d) Charge stability diagram of one single dot. Current flows only in correspondence to the diagonal lines and Coulomb blockade peaks as shown in Fig. 2.3c are measured.

The electronic occupation of the double dot is described by the *charge stability diagram*.

The double dot occupancy depends on the externally controllable parameters  $V_{PgL}$  and  $V_{PgR}$  for different values of interdot coupling (the explanations refer to Fig. 2.4). In the limit of no interdot coupling (i.e.  $C_m=0$ , see Fig. 2.4b), changes in voltage of plunger 1 (2) affect only the charge configuration of dot 1 (2) leaving the charge configuration of dot 2 (1) unchanged. In the case of intermediate interdot coupling (Fig. 2.4c) the charge configuration of dot 1 is also affected by changes of plunger gate 2, which is visible in two ways on the stability diagram:

- the lines separating different charge configurations are tilted, the slope shows that on dot 1 (2) also plunger 2 (1) has an effect on the charge configuration.
- the crossing between lines splits and the charge state domains become hexagonal (also called *honeycombs*), and the exchange of electrons between the two dots is possible.

When the interdot coupling is large (Fig. 2.4d), a situation is reached where one large single dot is equally coupled to both plunger gates.

Current from source to drain flows only at the so called *triple points* (indicated with red dots in Fig. 2.4c), namely when the electrochemical potential of both dots align with the electrochemical potential of the leads. The distance in plunger gate voltage between the two triple points is a function of the interdot capacitance and tends to zero as  $C_M$  tends to zero, and to a constant for  $C_M$  much larger than  $C_L$  and  $C_R$ .

Let us consider two honeycombs with charge states  $(m, n)$  and  $(m - 1, n + 1)$  where  $m$  ( $n$ ) is the electron number in the left (right) dot: we can transfer one electron from one quantum dot to the other without exchanging any with the leads. All the experiments presented in this thesis focus on the charge configurations  $(0,2)$  and  $(1,1)$ . In the following

section we will focus on this particular region of the charge stability diagram.

#### 2.2.4 The spin configurations at the (0,2) to (1,1) charge transition

As we will see in more detail in the next section, our qubit is encoded in the spin state of two electrons confined in a double quantum dot [13]. Let us first focus on the region of the stability diagram between the (0,2) and (1,1) charge states. Finite tunnel coupling produces an avoided crossing between  $E_{(0,2)}$  and  $E_{(1,1)}$ , so that the two states hybridize, allowing to smoothly pass an electron from one dot to the other. Fig. 2.5b shows the avoided crossing between the energies of the two charge states. The transition between the two charge states is parametrized by a change of gate voltage  $\varepsilon$  along a diagonal line (possible when changing the voltages on the plunger gates L and R simultaneously). Throughout the thesis this specific gate voltage change, indicated with  $\varepsilon$ , will be called *detuning*, with  $\varepsilon = 0$  chosen to be the (0,2)-(1,1) degeneracy point. For  $\varepsilon \gg 0$  the two electrons are both confined to one dot, and for  $\varepsilon \ll 0$  they are completely separated in two different dots.

Neglecting spin, the tunneling Hamiltonian in the basis  $\{(0,2), (1,1)\}$  is:

$$H = \begin{pmatrix} -\frac{e\varepsilon}{2} & t_c \\ t_c & \frac{e\varepsilon}{2} \end{pmatrix}$$

with eigenvalues  $E = \pm \frac{1}{2} \sqrt{(e\varepsilon)^2 + 4t_c^2}$  where  $e$  is the electron charge.

We discuss now the spin configurations of the (0,2) charge configuration in the absence of magnetic field. In the lowest energy state the electrons occupy the lowest orbital level. In order to satisfy the Pauli exclusion principle the two-electron ground state must be a singlet state [29], with a spin wavefunction:

$$|S\rangle = \frac{| \uparrow\downarrow \rangle - | \downarrow\uparrow \rangle}{\sqrt{2}}.$$

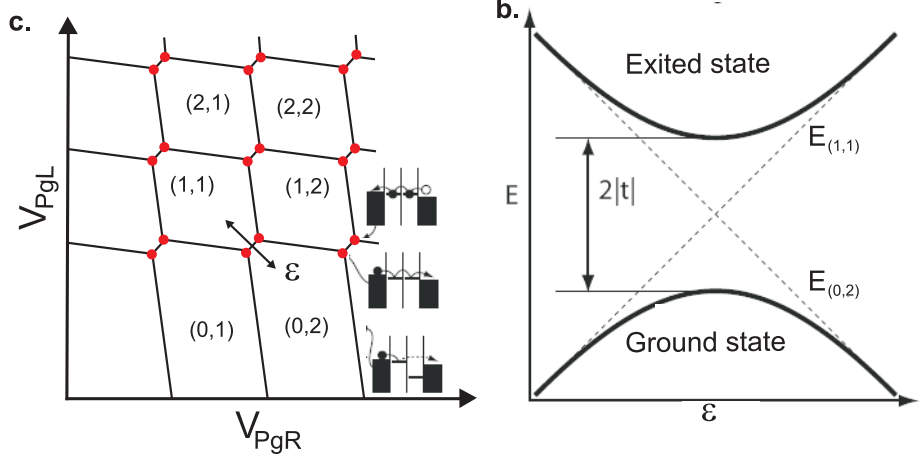


Figure 2.5: a) Schematic representation of the charge stability diagram, showing the different charge states indicated as  $(m, n)$  where  $m$  is the number of electrons in the left dot and  $n$  the number of electrons in the right dot. Current between source and drain flows at the triple points, where the electrochemical potential of source, drain and the two dots are aligned. b) Energy as a function of detuning  $\epsilon$  indicated in gate space in part a). Due to the presence of a finite tunnel coupling the two charge states  $(0,2)$  and  $(1,1)$  hybridize. Adapted from [22].

To guarantee the antisymmetry of the total wavefunction, the electrons in the triplet states occupy both the first and the second orbital states and have thus higher energy, with spin wavefunction:

$$|T_+\rangle = |\uparrow\downarrow\rangle, \quad |T_0\rangle = \frac{|\uparrow\downarrow\rangle + |\downarrow\uparrow\rangle}{\sqrt{2}}, \quad |T_-\rangle = |\downarrow\downarrow\rangle.$$

Likewise, for the  $(1,1)$  charge configuration, the ground state is a singlet state and the first excited states are triplets. In this case, however, the wavefunctions' overlap is much smaller and the singlet and triplet states are almost degenerate. Thus, the low-energy spin dynamics of the two electron system can be described by the Heisenberg Hamiltonian:

$$H = J(\epsilon) \mathbf{S}_1 \cdot \mathbf{S}_2$$

where  $\mathbf{S}_1$  and  $\mathbf{S}_2$  are the spin operators of the two electrons, and  $J(\epsilon)$  is the energy difference between the singlet and the triplet state [30].

When applying a magnetic field (either parallel or perpendicular to the 2DEG) the

triplet states  $|T_+\rangle$  and  $|T_-\rangle$  separate from  $|T_0\rangle$  by the Zeeman energy  $E_z = g^* \mu_B B$ , where  $g^* \approx -0.44$  is the electron  $g$ -factor for bulk GaAs and  $\mu_B$  the Bohr magneton.

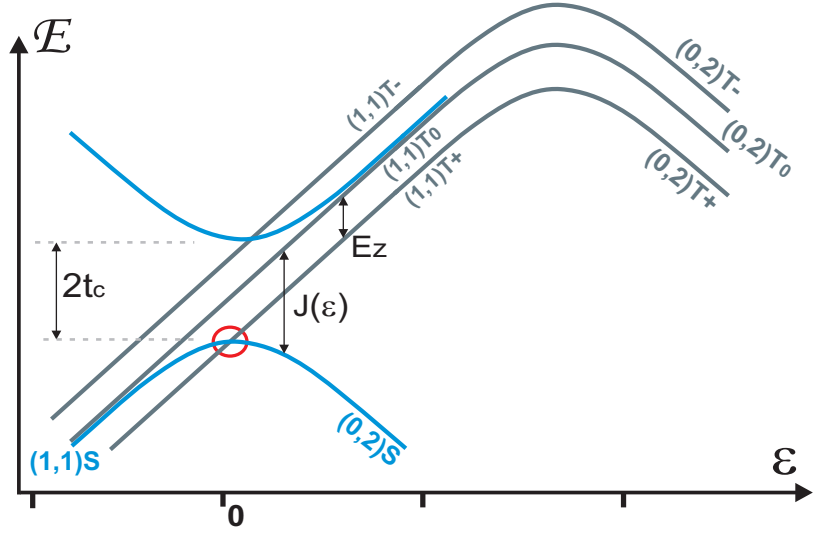


Figure 2.6: Energy levels at the  $(0,2)$ - $(1,1)$  charge transition including spin and an external magnetic field. Both the  $S(0,2)$ - $S(1,1)$  anticrossing and the  $T(0,2)$ - $T(1,1)$  anticrossing, which are possible at a different detuning  $\varepsilon$ , are indicated. Indicated are also the Zeeman energy  $E_z$ , the singlet-triplet energy difference  $J(\varepsilon)$  and the tunnelling  $t_c$ .

There is a second magnetic field effect which is not relevant for this work. A magnetic field applied perpendicular to the 2DEG affects the orbital part<sup>1</sup> of the electron wavefunction and, if the confining potential of the quantum dot is approximated to be parabolic, the eigenenergies are given by the Fock-Darwin spectrum [31]. When increasing the perpendicular magnetic field the energy of the singlet state increases, while the energy of the triplet state decreases, leading to a crossing point at a magnetic field  $B_{crossing}$ , where  $E_S = E_T$  [32]. The experiments presented in this thesis are performed with magnetic fields parallel to the 2DEG (except in Chap. 8, where the applied magnetic field was perpendicular but never exceeded 150 mT, which was experimentally verified to be smaller than  $B_{crossing}$ ).

Tunneling processes conserve the spin state of the two electrons. This means that when

---

<sup>1</sup>The term  $\mathbf{p} \cdot \mathbf{A} + \mathbf{A} \cdot \mathbf{p} \sim B_z \cdot L_z$  in the Hamiltonian.

a transition from the (0,2) to the (1,1) charge state is induced by changing the detuning  $\varepsilon$ , the (0,2) singlet state transitions into the (1,1) singlet state (and vice versa). However, if the system is in a triplet state in the (1,1) charge configuration, transitions to the (0,2) charge state are not possible, because  $T(0,2)$  is energetically not available at the chosen gate voltage configurations. This effect is known as the *Pauli spin blockade* [33, 34], i.e. the triplet spin state is blocked in the (1,1) charge configuration, while the singlet state is not.

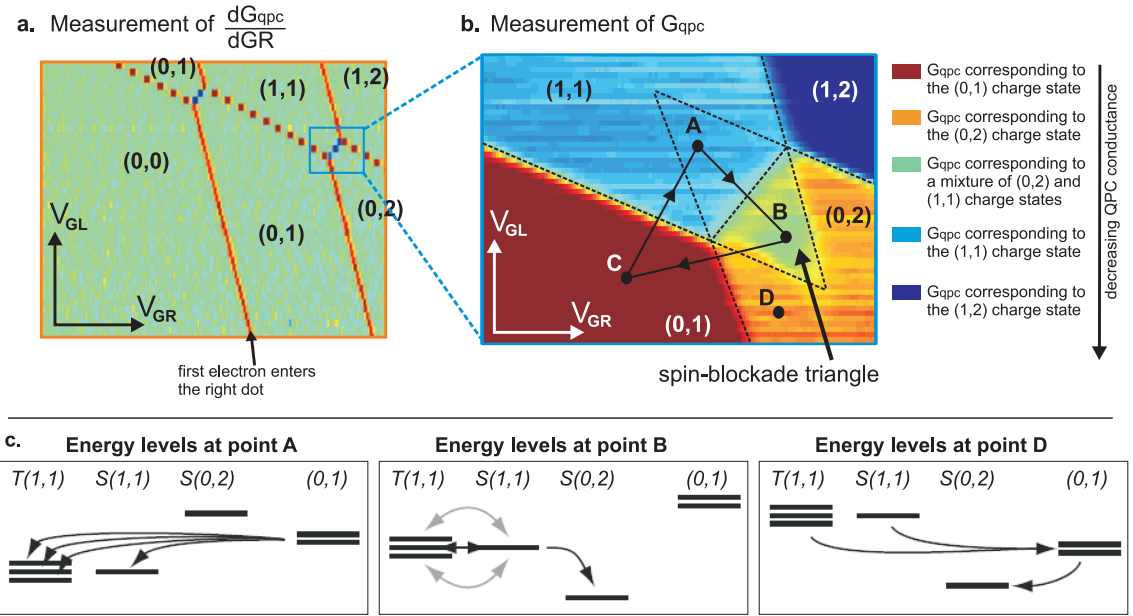


Figure 2.7: a) Measurement of the charge stability diagram. As the voltages on the two plunger gates ( $V_{GL}$  and  $V_{GR}$ ) are made more negative the dot is emptied. The (0,0) charge state is reached when no more jumps in  $\frac{dG_{qpc}}{dGR}$  are measured for large changes in gate voltages. b) Close-up view of the (0,2)-(1,1) charge transition and measurement of the QPC conductance  $G_{qpc}$ . Each charge configuration is characterized by a different value of QPC conductance, decreasing as more electrons are added to the dot. c) Schematic visualization of Pauli spin blockade. When moving from point C to point A electrons are loaded in a random spin state in the (1,1) charge configuration. When returning to point B, only transitions from  $S(1,1)$  to  $S(0,2)$  can occur. At point D, transitions from  $T(1,1)$  to  $S(0,2)$  can occur by exchanging electrons with the leads. Adapted from [22].

Fig. 2.7b shows a measured charge stability diagram (schematically introduced in Fig. 2.4), where each charge state is characterized by a different color. The green triangle in the (0,2) region indicates the region in gate space where the (1,1) charge configuration is still ener-

getically allowed. The spin-blockade triangle is measured in the following way: the gate voltages are first moved to point C (in Fig. 2.7b), where the ground state is the (0,1) charge state. By subsequently moving the gates to point A, a second electron is loaded into the dot in a singlet or one of the triplet spin states with similar probabilities. When returning to point B, the system can remain blocked in the (1,1) configuration. The charge configuration at point B is measured by averaging over many such pulse cycles, each cycle lasting about 10  $\mu$ s, with the measurement time being approximately 90% of the whole pulse cycle. A detailed explanation of the charge state measurement is given in the following section. Transitions from (0,2) to (1,1) can always occur, so there is no equivalent triangle in the (1,1) region. Below the (0,1)-(1,1) transition boundary (at point D for example) the (0,1) charge state's energy is intermediate between the energies of the (0,2) and (1,1) charge states. The transition from a (1,1) to a (0,2) charge configuration can thus occur by going through an intermediate state (the (0,1) charge state) and exchanging electrons with the leads overcoming spin blockade [22].

The singlet-triplet energy difference in (0,2) is typically on the order of a few hundred  $\mu$ eV, and the tunnel coupling one to ten  $\mu$ eV [32].

### **2.2.5 Determining the charge configuration with a charge sensing technique**

The dot occupancy is measured with a quantum point contact (QPC) which is placed very close to the dot and is thus capacitively connected to it. A QPC is a narrow one dimensional channel (lithographically defined by gates) carrying a discrete number of modes. Its conductance varies in a step-like manner when an additional conducting mode becomes available, for instance by changing the voltages on the gates [35].

The QPC's maximum sensitivity is at the conductance's steepest point (usually before the first conductance plateau). When, for example, an electron is added to the dot, the QPC conductance abruptly decreases. This is a powerful tool that allows us to detect the dot's occupancy even when the current through the dot becomes undetectable (i.e. when the tunneling rate is too small).

Each charge state is characterized by a distinct value of QPC conductance. The calibration is done in the following way: we first empty the dots by making the voltages on gate R (GR) and gate L (GL) so negative that no more jumps of the QPC conductance are detected, as shown in Fig. 2.7a. Then we add one electron at the time and locate the regions corresponding to the (0,2) and (1,1) charge states. At this point we determine the QPC conductance values for the (0,1), (1,1), (0,2) and (1,2) charge configurations as shown in Fig. 2.7b. As the number of electrons in the dots increases  $G_{qpc}$  decreases. In this particular case the QPC was coupled more strongly to the left dot, as  $G_{qpc}$  corresponding to the (1,1) charge configuration is smaller than  $G_{qpc}$  corresponding to the (0,2) charge configuration.

Throughout the thesis we need to determine the spin configuration of the two-electrons state at the end of a manipulation stage. Measuring the charge configuration is much easier than measuring the tiny magnetic moment of an electron ( $\mu_B = 9.27 \cdot 10^{-24}$  J/T). Different spin configurations thus need to be mapped onto charge configurations in order to be measured. As we saw in the previous section, singlets can be mapped onto the (0,2) charge state and triplet onto the (1,1) charge state, courtesy of the Pauli spin blockade. This *spin to charge* conversion technique [36, 37, 38] is used as measurement method in all experiments presented in this thesis.

## 2.3 Two-electron spin qubit

### 2.3.1 Motivation

Proposals for qubit encoding in two-electron spin states rather than one-electron spin states [12] were made a few years ago [39, 40, 41]. There are two main reasons why the interest in two-electron spin states arose:

- The use of microwave fields to address single spin qubits, and the associated problems such as heating, can be avoided. Manipulations using the exchange interaction between two electrons can be controlled all electrically.
- Fluctuations of the external magnetic field affect one-electron spin qubits because they change the Zeeman energy and thus the spin precession frequencies ( $hf = g^* \mu_B B$ ).

Two-electron spin states with vanishing angular momentum along the uniform magnetic field  $\mathbf{B}_{\text{ext}}$  are not affected by fluctuations of  $\mathbf{B}_{\text{ext}}$ .

In order to make all one-qubit operations possible, two axes of rotation around the Bloch sphere (see Fig. 2.8) need to be controlled. For the two-electrons spin qubits it has been proposed [39, 41] to control one axis of rotation by changing the energy difference between the two basis states  $J(\varepsilon)$  via electric fields (i.e. gate voltages). The second axis of rotation can be controlled by unequal local environments for the two spins through  $g$ -factor engineering [42] or permanent magnets [43]. In this thesis a third method was employed: dynamic nuclear polarization of different groups of nuclei interacting with the two electron spins.

As we have seen in the previous section, the available spin states in the (1,1) charge configuration are the singlet state  $|S\rangle$  and the three triplet states  $|T_0\rangle$ ,  $|T_+\rangle$  and  $|T_-\rangle$ . The  $|T_+\rangle$  and  $|T_-\rangle$  states are split off from  $|T_0\rangle$  by an external magnetic field. The two-electron

spin qubit basis states chosen for the experiments presented in this thesis are the singlet state  $|S\rangle$  and the triplet state  $|T_0\rangle$ . Fig. 2.8 shows the Bloch sphere with the basis states of the qubit,  $|S\rangle$  and  $|T_0\rangle$ , at the poles and the states  $\frac{|S\rangle+|T_0\rangle}{\sqrt{2}} = |\uparrow\downarrow\rangle$  and  $\frac{|S\rangle-|T_0\rangle}{\sqrt{2}} = |\downarrow\uparrow\rangle$  on the  $x$ -axis. The  $|S\rangle$  and  $|T_0\rangle$  states are separated by an energy  $J(\varepsilon)$ : rotations around the  $z$ -axis correspond to the rapid exchange of the two electrons.

An energy difference between the states  $|\uparrow\downarrow\rangle$  and  $|\downarrow\uparrow\rangle$  exists when each electron is subject to a different local magnetic field. If for example  $B_{local,L,z} > B_{local,R,z}$ , the state  $|\uparrow\downarrow\rangle$  has a lower total Zeeman energy than the state  $|\downarrow\uparrow\rangle$ . This local magnetic field difference for the left and the right dot is provided by a different local nuclear magnetic field acting on the electrons via hyperfine coupling.

### 2.3.2 Electron-nuclei hyperfine interaction

Before discussing qubit manipulations in more detail, we briefly introduce the origin of the interaction between electrons and nuclei. The spins of electrons localized inside quantum dots interact with about  $10^6$  nuclei [34]. GaAs has three different spin- $\frac{3}{2}$  nuclei,  $^{75}\text{As}$ ,  $^{69}\text{Ga}$  and  $^{71}\text{Ga}$ . For simplicity, let us first consider the interaction between one nuclear spin  $\mathbf{I}$  and one electron spin  $\mathbf{S}$  [44]:

$$H = \frac{\hbar^2 \gamma_n \mathbf{I} \cdot g_0 \mu_B \mathbf{S}}{r^3} + \frac{3\hbar^2 (g_0 \mu_B \mathbf{S} \cdot \mathbf{r})(\gamma_n \mathbf{I} \cdot \mathbf{r})}{r^5} + \frac{2\mu_0}{3} g_0 \mu_B \gamma_n \hbar |\Psi(0)|^2 \mathbf{I} \cdot \mathbf{S} \quad (2.4)$$

where  $\gamma_n$  is the nuclear gyromagnetic factor,  $\mu_0$  the permeability of free space,  $g_0$  the free electron  $g$ -factor,  $\mu_B$  the Bohr magneton,  $|\Psi(0)|^2$  the probability of finding the electron at the position of the nucleus (assumed to be at the origin) and  $\mathbf{r}$  is the vector between the nucleus' position and the electron's position. We consider electrons in the conduction band, which in the case of GaAs are in an s-orbital (i.e. spherically symmetric). This means that the electrons wavefunction is non-zero at the position of the nucleus. For this particular

case only the third term, the so called *Fermi contact term* survives while all other terms average to zero.

The Hamiltonian for an electron interacting with  $N$  nuclei is:

$$H_{hf} = \frac{2\mu_0}{3} g_0 \mu_B \gamma_n \hbar \sum_k^N |\Psi(\mathbf{r}_k)|^2 \mathbf{I}_k \cdot \mathbf{S}$$

where  $\mathbf{I}_k$  is the spin of the  $k$ -th nucleus,  $\mathbf{S}$  the electron spin. The wavefunction for a conduction electron in a crystal can be written as the product of a periodic Bloch function  $u(\mathbf{r})$  and an envelope function  $\Phi(\mathbf{r})$  [29], thus giving:

$$H_{hf} = \frac{2\mu_0}{3} g_0 \mu_B \gamma_n \hbar \sum_k^N |u(\mathbf{r}_k)|^2 |\Phi(r_k)|^2 \mathbf{I}_k \cdot \mathbf{S} = \sum_k^N A_k \mathbf{I}_k \cdot \mathbf{S}$$

where  $A_k = \nu_0 A |\Phi(\mathbf{r}_k)|^2$  is defined as the position dependent hyperfine coupling strength, with  $\nu_0$  the volume of the crystal unit cell,  $|\Phi(\mathbf{r}_k)|^2$  the probability density of finding the electron at position  $\mathbf{r}_k$  and  $A$  the average hyperfine coupling weighted by the natural abundance of the three isotopes ( $A = 90 \text{ } \mu\text{eV}$  for GaAs) [45]. We can rewrite this equation in the following way:

$$H_{hf} = \left( \sum_k^N A_k \mathbf{I}_k \right) \cdot \mathbf{S} = g^* \mu_B \mathbf{B}_N \cdot \mathbf{S}$$

where  $\mathbf{B}_N = \frac{1}{g^* \mu_B} (\sum_k^N A_k \mathbf{I}_k)$  acts like an effective magnetic field on the electron, and is called the Overhauser field. If all spins were aligned, the effective field strength would be about 5 T [46].

Since electron-spin dynamics occurs on a much faster time scale than nuclear spin dynamics, we consider the nuclei as static during electron motion. We will address the issue of slow nuclear spin dynamics in Sect. 2.4.

We conclude with the following remark: the contact hyperfine coupling conserves the total angular momentum  $\mathbf{S} + \mathbf{I}$ , because it commutes with the hyperfine Hamiltonian  $\mathbf{I} \cdot \mathbf{S}$ .

Accordingly, the contact term can be rewritten in terms of the raising and lowering operators

$$I^\pm = \frac{1}{\sqrt{2}}(I_x \pm I_y) \text{ and } S^\pm = \frac{1}{\sqrt{2}}(S_x \pm S_y) \text{ for electron and nuclear spins as}$$

$$\mathbf{I} \cdot \mathbf{S} = I^+S^- + I^-S^+ + 2I_zS_z$$

to make it evident that an electron spin flip from up to down must be accompanied by a nuclear spin flip in the opposite direction.

### 2.3.3 Qubit manipulations

We are now in the position to write the complete Hamiltonian for two electrons in the (1,1) charge configuration, considering the energy difference between the  $|S\rangle$  and the  $|T_0\rangle$  states, the interactions of the electrons with the external magnetic field  $B_{ext}$  and the local magnetic fields in the left and in the right dot  $\mathbf{B}_{nuc,L}$  and  $\mathbf{B}_{nuc,R}$  (following [47]):

$$H = g^* \mu_B [(\mathbf{B}_{ext} + \mathbf{B}_{nuc,L}) \cdot \mathbf{S}_L + (\mathbf{B}_{ext} + \mathbf{B}_{nuc,R}) \cdot \mathbf{S}_R] - J(\varepsilon) |S\rangle \langle S|$$

which can be simplified and rewritten as follows:

$$H = g^* \mu_B [\mathbf{B} \cdot (\mathbf{S}_L + \mathbf{S}_R) + \Delta \mathbf{B} \cdot (\mathbf{S}_L - \mathbf{S}_R)] - J(\varepsilon) |S\rangle \langle S| \quad (2.5)$$

where  $\mathbf{S}_{L,R}$  the spin operators for the left and right electrons,  $\mathbf{B} = \mathbf{B}_{ext} + \frac{\mathbf{B}_{nuc,L} + \mathbf{B}_{nuc,R}}{2}$  is the average magnetic field and  $\Delta \mathbf{B} = \frac{\mathbf{B}_{nuc,L} - \mathbf{B}_{nuc,R}}{2}$  is the difference in local magnetic field between the two dots. The homogeneous term simply adds to the external magnetic field and changes only the Zeeman splitting, while the inhomogeneous term couples singlet with triplet states. This is easier to visualize when rewriting eq. (2.5) in matrix form in the basis

$\{|T_-\rangle, |T_0\rangle, |T_+\rangle, |S\rangle\}$ :

$$H = g^* \mu_B \begin{pmatrix} B_z & 0 & 0 & \frac{\Delta B_x - i\Delta B_y}{\sqrt{2}} \\ 0 & 0 & 0 & -\Delta B_z \\ 0 & 0 & -B_z & \frac{\Delta B_x + i\Delta B_y}{\sqrt{2}} \\ \frac{\Delta B_x + i\Delta B_y}{\sqrt{2}} & -\Delta B_z & \frac{\Delta B_x + i\Delta B_y}{\sqrt{2}} & \frac{-J(\varepsilon)}{g^* \mu_B} \end{pmatrix} \quad (2.6)$$

which shows that the  $x$  and  $y$  components of  $\Delta\mathbf{B}$  mix the singlet with  $|T_+\rangle$  and  $|T_-\rangle$ , while the  $z$  component mixes the singlet with  $|T_0\rangle$  (the quantization axis for the electron spin is along  $\mathbf{B}_{ext} = B_{ext}\mathbf{e}_z$ ).

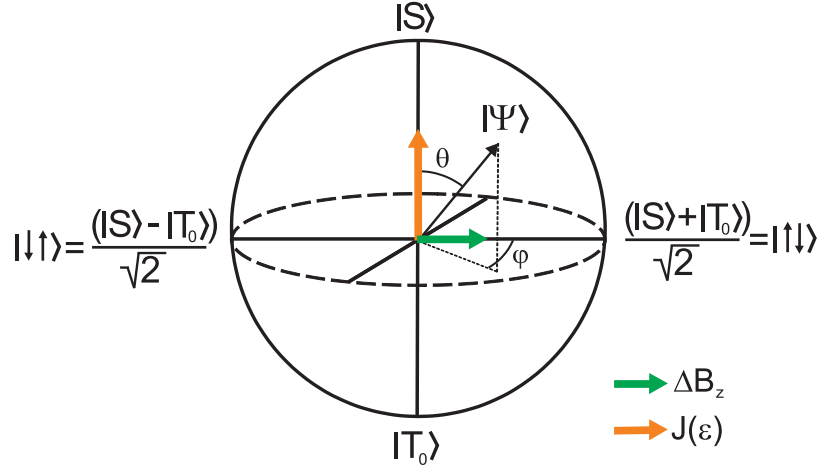


Figure 2.8: Bloch sphere representation of the qubit with basis states  $|S\rangle$  and  $|T_0\rangle$  shown at the north and south pole. Rotations around the  $z$ -axis are controlled by the energy difference between  $|S\rangle$  and  $|T_0\rangle$ ,  $J(\varepsilon)$ , while rotations around the  $x$ -axis are controlled with the difference in local magnetic field in  $z$  direction  $\Delta B_{nuc}^z$ .

Away from the charge transition and with  $|T_+\rangle$  and  $|T_-\rangle$  split off from  $|T_0\rangle$  due to the presence of an external magnetic field, the Hamiltonian in the  $\{|T_0(1,1)\rangle, |S(1,1)\rangle\}$  basis

$$H = -g^* \mu_B \begin{pmatrix} 0 & \Delta B_z \\ \Delta B_z & \frac{J(\varepsilon)}{g^* \mu_B} \end{pmatrix} = \frac{J(\varepsilon)}{2} (-\mathbb{1} + \sigma_z) - g^* \mu_B \Delta B_z \sigma_x$$

describes the dynamics in the singlet-triplet subspace. Rotations around the  $z$ -axis are controlled by varying the energy difference between  $|T_0(1,1)\rangle$  and  $|S(1,1)\rangle$ ,  $J(\varepsilon)$ , that can

be varied by changing  $\varepsilon$  (i.e. by applying a change to the voltages on the plunger gates).

Whereas up until now we considered only the (1,1) charge states, for values of  $\varepsilon$  close to the charge transition, the singlet state is a linear superposition of  $S(1,1)$  and  $S(0,2)$ . Following [48] we define:

$$|\tilde{S}\rangle = \cos \theta |S(1,1)\rangle + \sin \theta |S(0,2)\rangle$$

$$|\tilde{E}\rangle = -\sin \theta |S(1,1)\rangle + \cos \theta |S(0,2)\rangle$$

where  $|\tilde{S}\rangle$  is the ground state,  $|\tilde{E}\rangle$  the excited state and

$$\theta = \arctan \left( \frac{2t_c}{e\varepsilon - \sqrt{(e\varepsilon)^2 + 4t_c^2}} \right).$$

From the Hamiltonian in eq. (2.6) we see that the  $x$  and  $y$  components of the local magnetic field difference drive transitions between  $|\tilde{S}\rangle$  and  $|T_+\rangle$ , as shown for the  $\{|\tilde{S}\rangle, |T_+\rangle\}$  subsystem:

$$H = g^\star \mu_B \begin{pmatrix} B_z & \frac{dB_x - idB_y}{\sqrt{2}} \cos(\theta) \\ \frac{dB_x + idB_y}{\sqrt{2}} \cos(\theta) & \frac{J(\varepsilon)}{g\mu_B} \end{pmatrix} \quad (2.7)$$

### 2.3.4 Dynamic nuclear polarization

The Hamiltonian (2.7) involves transitions between  $|\tilde{S}\rangle$  and  $|T_+\rangle$  with a change of angular momentum in the  $z$ -direction. Since the contact hyperfine interaction conserves total spin angular momentum, the electron spin flip must be accompanied by a spin flip of the nuclei (see final remark in Sect. 2.3.2). This can be used to build up a nuclear polarization by continuously inducing nuclear spin flips in the same direction [49]. Dynamic nuclear polarization can be achieved with the double dot presented so far, where we make use of the avoided crossing between  $|\tilde{S}\rangle$  and  $|T_+\rangle$ , indicated with a red circle in Fig. 2.6b.

In one type of pumping cycle, the electrons are initialized in the S(0,2) state, at which point the state is brought close to the  $S-T_+$  degeneracy point. When subsequently adiabatically sweeping through the avoided crossing, a spin flip in the electron system with  $\Delta m_z = 1$  occurs, which induces a spin flip in the nuclei. The system is then reinitialized by exchanging electrons with the leads, a process that does not affect the polarization of the nuclei. When repeating this manipulation for a large number of times a nuclear polarization is built up. This dynamic nuclear polarization cycle both changes  $B_{nuc}^z$  and  $\Delta B_{nuc}^z$  as it will be shown in the experimental results presented in Chap. 5. In that experiment, a second type of pumping cycle is also presented.

### Direction of the induced magnetic field

We now analyze the sign of the induced polarization and the direction of the induced nuclear magnetic field acting on the electron [50]. Let us first consider the magnetic moment of the electrons, which is given by:

$$\boldsymbol{\mu}_e = \gamma_e \mathbf{S} = g_e \frac{e}{2m_e} \mathbf{S} = \frac{|g_e| \mu_B}{\hbar} \mathbf{S}$$

with  $\gamma_e$  the electron's gyromagnetic factor. The Hamiltonian for an electron in a magnetic field is given by:

$$H_{Z,e} = -\boldsymbol{\mu}_e \cdot \mathbf{B} = -\gamma_e \mathbf{S} \cdot \mathbf{B}$$

Similarly, for nuclei with spin  $\mathbf{I}$ , the magnetic moment is:

$$\boldsymbol{\mu}_n = \gamma_n \mathbf{I} = g_n \frac{e}{2m_p} \mathbf{I} = \frac{g_n \mu_n}{\hbar} \mathbf{I}$$

with  $\gamma_n$  the gyromagnetic ratio,  $g_n$  the  $g$ -factor of the nuclei and  $\mu_n = \frac{|e|\hbar}{2m_p}$ . The Hamiltonian for a nucleus in a magnetic field is:

$$H_{Z,n} = -\boldsymbol{\mu}_n \cdot \mathbf{B} = -\gamma_n \mathbf{I} \cdot \mathbf{B}$$

Because for electrons in GaAs both the effective  $g$ -factor and the charge are negative ( $g^* = -0.44$  in bulk), the magnetic moment is parallel to its spin. The same happens for the nuclei, where both the  $g$ -factor and the charge are positive. From this it follows that spin up (spin parallel to  $\mathbf{B}$ ) is the ground state for both cases. This means that when an electron flips from up to down a nuclear spin flips from down to up (and vice versa).

Thus, it remains to determine the direction of the induced magnetic field perceived by the electron. The hyperfine coupling constant  $A$  in the Hamiltonian  $H_{hf} = \sum_i A_i \mathbf{I}_i \cdot \mathbf{S}$  is positive (i.e. the coupling is antiferromagnetic) and the lowest energy configuration corresponds to antiparallel electron and nuclear spins. If we consider the Hamiltonian for the electrons, including both the Zeeman and the hyperfine term we can rewrite it as:

$$H = H_Z + H_{hf} = -\gamma_e \mathbf{S} \cdot \mathbf{B} + \sum_i A_i \mathbf{I}_i \cdot \mathbf{S} = -\gamma_e \mathbf{S} \cdot \left( \mathbf{B} - \sum_i \frac{A_i}{\gamma_e} \mathbf{I}_i \right)$$

where  $A_i/\gamma_e > 0$ . This means that the effective nuclear magnetic field points opposite the nuclear polarization: when spin ups are pumped into the nuclear system, the total magnetic field  $\mathbf{B}_{ext} + \mathbf{B}_{nuc}$  acting on the electrons decreases. In the case of the polarization cycle introduced in the previous section, the total nuclear magnetic moment decreases while the nuclear magnetic field acting on the electron increases.

### 2.3.5 Spin flip due to spin-orbit coupling

Magnetic coupling is the only way to interact with the electron's spin. In the previous section, we saw that electrons confined in quantum dots interact via hyperfine coupling with their environment. There is a second way electrons interact with the environment: spin-orbit coupling.

According to special relativity, a particle moving with momentum  $\mathbf{p}$  in an electric field  $\mathbf{E}$ , experiences an effective magnetic field  $\mathbf{B} = \mathbf{E} \times \mathbf{p}$ . This is the case for an electron

moving in the periodic potential of the crystal lattice and has the same origin as spin-orbit coupling in an atom.

GaAs has a zincblende structure, which has the property of breaking inversion symmetry [48]. For conduction band electrons in GaAs one can write an effective spin-orbit Hamiltonian which is known as the Dresselhaus term, shown here for the 2 dimensional case of a heterostructure with strong confinement along the  $z$ -axis in the [001] crystal axis (following [51]):

$$H_D^{2D} = \beta[-p_x\sigma_x + p_y\sigma_y]$$

where  $p_x$  and  $p_y$  are the momentum operators in the  $x$  and  $y$  direction and  $\sigma_x$  and  $\sigma_y$  the spin operators in the  $x$  and  $y$  direction. The effective internal magnetic field in the Dresselhaus term is aligned with the momentum when  $\mathbf{p}$  points along the crystal axis [010], and anti-aligned with the momentum when  $\mathbf{p}$  points along the crystal axis [100].

A second contribution is known as the Rashba term, associated with the asymmetric confining potential, the triangular well at the interface between GaAs and AlGaAs. The asymmetry generates the needed electric field, and the Rashba spin-orbit contribution is of the form:

$$H_R = \alpha[-p_y\sigma_x + p_x\sigma_y]$$

with the effective internal magnetic field always orthogonal to the momentum.

The characteristic length scale associated with spin-orbit coupling is the spin-orbit length  $l_{SO}$  defined as the distance the electron moves (ballistically) before its spin is rotated by  $\pi$ : the shorter  $l_{SO}$ , the stronger the spin orbit coupling. Both the Dresselhaus and the Rashba terms are linear in momentum, which implies that  $l_{SO}$  is independent of the electron velocity (if the electron moves faster, its spin also rotates faster); it also implies that if the electron retraces its path, the spin precession is exactly undone.  $l_{SO}$  has been exper-

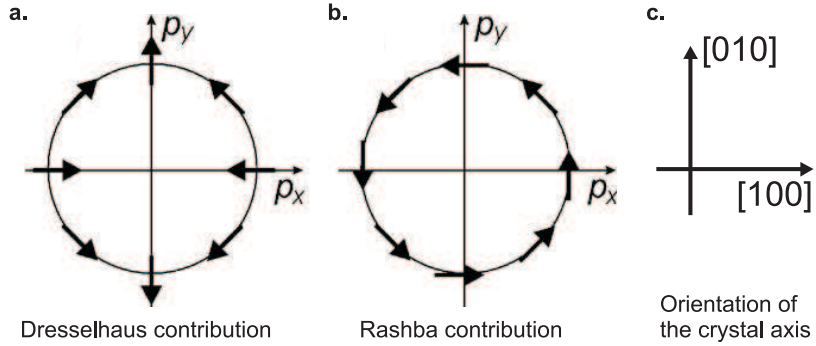


Figure 2.9: Spin-orbit interaction. a) Schematic diagram of the orientation of the apparent magnetic field (arrow direction) that acts on the electron spin as a result of Dresselhaus spin-orbit interaction. b) Schematic diagram of the orientation of the apparent magnetic field (arrow direction) that acts on the electron spin as a result of Rashba spin-orbit interaction. c) Diagram showing the orientation of the crystal axes. Adapted from [51].

mentally determined to be on the order of 1-10  $\mu\text{m}$  [52] in GaAs/AlGaAs heterostructure 2DEGs similar to the ones employed for experiments presented in this thesis.

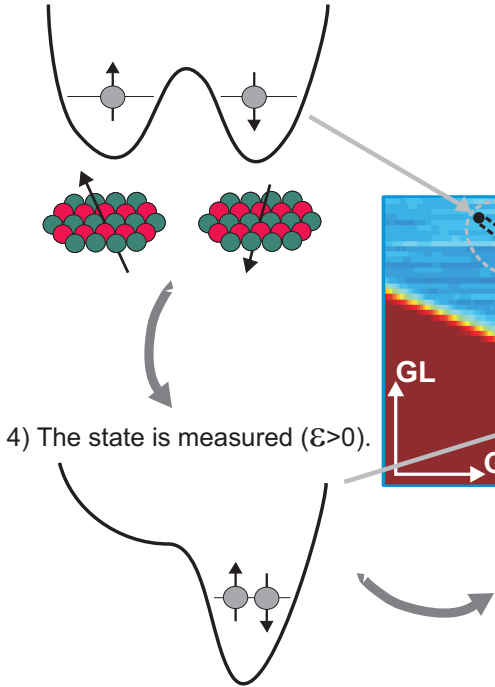
The typical dimension of our quantum dots are on the order of 100 nm  $\ll l_{SO}$ ; spin-orbit coupling is thus considered to only weakly affect the electron spin state. We will see though that to explain the results presented in Chap. 8 spin-orbit interaction cannot be ignored.

### 2.3.6 Preparation, manipulation and read-out: a summary

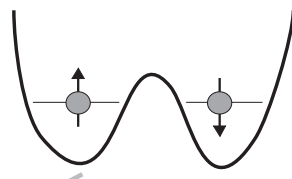
To summarize the concepts introduced until now, we briefly illustrate how they are employed for the preparation, manipulation and the read-out of the qubit. The qubit can be reliably prepared in the (0,2) charge configuration, where the only available spin state is a singlet. The values on the gate voltages are then changed, in order to separate the two electrons, adiabatically with respect to tunneling  $t_c$ , to avoid Landau-Zener tunneling [53]. The detuning can be changed in two different ways with respect to hyperfine coupling: when  $\varepsilon$  is changed such that  $\hbar \frac{dJ}{d\varepsilon} \frac{d\varepsilon}{dt} \gg (g^* \mu_B \Delta B_{nuc}^z)^2$  the initialized state remains a singlet; in the opposite limit the initialized state becomes an  $|\uparrow\downarrow\rangle$  state (the ground state for

$$g^* \mu_B \Delta B_{nuc}^z \gg J(\varepsilon)) [47].$$

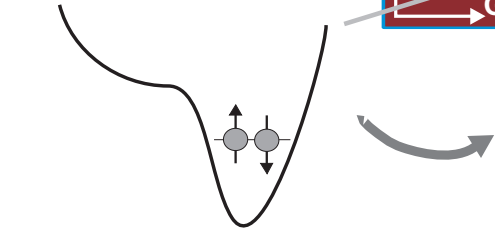
3) The state is manipulated ( $\varepsilon < 0$ ).



2) The electrons are separated ( $\varepsilon$  from positive to negative).



4) The state is measured ( $\varepsilon > 0$ ).



1) The state is prepared in a singlet state ( $\varepsilon > 0$ ).

5) Electrons are exchanged with the leads.

Figure 2.10: At the beginning of each pulse cycle, the state is loaded into a singlet state in the (0,2) charge configuration. The two electrons are then separated in two different dots. In the (1,1) charge configuration, the state is manipulated and subsequently read out by moving the gates back to the measurement point. After the measurement time the state is reinitialized and the cycle starts again.

At this point the qubit can be manipulated by setting the detuning  $\varepsilon$  to values where  $g^* \mu_B \Delta B_{nuc}^z \ll J(\varepsilon)$  (inducing rotations around the  $z$ -axis of the Bloch sphere) or values where  $g^* \mu_B \Delta B_{nuc}^z \gg J(\varepsilon)$  (inducing rotations around the  $x$ -axis of the Bloch sphere). After manipulation, the read-out takes place by bringing the gate voltages back to the (0,2) charge configuration and identifying the spin states after the manipulation by detecting whether the electrons are blocked in the (1,1) charge configuration (indicating a triplet state) or can transit into the (0,2) charge configuration (indicating a singlet state).

The signal measured with the QPC is a time-averaged measurement of the dot occupation throughout the entire pulse cycle. In order to obtain primarily information about

the charge state at the measurement point in (0,2), the measurement time  $t_M$  spent at this point has to be on the order of 90 % of the total pulse time. This is only required for low-frequency measurements, where an averaging over many pulse cycles is necessary. For the RF read-out schemes used in Chap. 7 this becomes unimportant.

The system is then reinitialized by moving into a region in gate space where electrons can be exchanged through the leads (such as point D indicated on Fig. 2.7b).

## 2.4 Decoherence

According to theoretical predictions (see for instance [14, 54]), sources of decoherence for the two-electron system are fluctuations in the nuclear magnetic field due to the hyperfine interactions at low magnetic field and the nuclear dipole-dipole interaction at high magnetic field. We will first give a brief explanation of these two types of decoherence processes and in the second part of the section we will discuss the ensemble coherence time  $T_2^*$  and the coherence time  $T_2$ .

### 2.4.1 Local magnetic field changes due to hyperfine interaction

At magnetic fields  $B_{ext} \ll B_{nuc}$  each nucleus precesses around the magnetic field generated by the electrons, the Knight field  $A_k \mathbf{S}$ . Due to the precession of the nuclei, the nuclear magnetic field changes over time. At magnetic fields  $B_{ext} \gg B_{nuc}$ , both electrons and nuclei precess around the external magnetic field. As previously seen in Sect. 2.3.2, the hyperfine Hamiltonian

$$H_{hf} = \mathbf{S} \cdot \sum_k^N A_k \mathbf{I}_k = \sum_k^N \frac{A_k}{2} (I_k^+ S^- + I_k^- S^+ + 2 I_k^z S^z).$$

describes electron-nuclear flip-flops. As the external field is increased, direct electron-nuclei flip-flops are no longer allowed due to Zeeman energy mismatch ( $E_{Z,e} \approx 25 \mu\text{eV/T}$  and

$E_{Z,n} \approx 30$  neV/T) as long as one is not at the  $S-T_+$  resonance. The efficiency of these flip-flop processes decreases as  $1/B_{tot,z}^2$  [55].

On the other hand, virtual processes have an efficiency that decreases only as  $1/B_{tot,z}$ . In this case a flip-flop between nucleus  $i$  and the electron is followed by a second flip-flop between the electron and nucleus  $j$  with an energy cost of  $A_i - A_j$ . Since the coupling constants  $A_k$  of the two nuclei are different, the effective local magnetic field experienced by the electron changes as the two nuclei are flipped. Each of these processes creates a different nuclear configuration, leading to decoherence [56].

#### 2.4.2 Local magnetic field changes due to dipole-dipole interaction

In addition to hyperfine interactions, dipole-dipole interactions between nuclei are responsible for nuclear spin dynamics. The Hamiltonian describing the dipole-dipole interaction between nuclei is, following [51]:

$$H_{dd} = \sum_{i < j} \frac{\mu_0 g_i \gamma_N^2 g_j \hbar}{4\pi} \left( \frac{\mathbf{I}_i \cdot \mathbf{I}_j}{|r_{ij}|^3} - \frac{3(\mathbf{I}_i \cdot \mathbf{r}_{ij})(\mathbf{I}_j \cdot \mathbf{r}_{ij})}{|r_{ij}|^5} \right)$$

with  $\mu_0$  the permeability of free space,  $g_i$  the  $g$ -factor of the  $i$ -th nucleus,  $\mu_N$  the nuclear magneton and  $\mathbf{r}_{i,j}$  the vector connecting nucleus  $i$  and nucleus  $j$ .

At high magnetic fields we need to only take into consideration the secular (i.e. energy conserving) term, and the Hamiltonian reduces to [57]:

$$H_{dd}^{sec} = D[\mathbf{I}_i \cdot \mathbf{I}_j - 3I_i^z I_j^z] = \frac{D}{2}[I_i^+ I_j^- + I_i^- I_j^+ - 4I_i^z I_j^z]$$

with the interaction term for GaAs  $D = \frac{\hbar}{100\mu s}$  [58]. We only consider nuclei  $i$  and  $j$  at different positions but of the same species (nuclei of different species have a different gyromagnetic factor, which, at finite magnetic field, would lead to an energy mismatch).  $B_{nuc}^{x,y}$  evolve on a time scales of 100  $\mu s$ .  $B_{nuc}^z$  can evolve on similar time scales, but in the

presence of an electron in the dot (i.e. a Knight field gradient) its evolution is typically slower. Note that in the presence of a Knight field, if  $|A_i - A_j| > D$ , flip-flops are forbidden by energy conservation.

### 2.4.3 Determining the ensemble coherence time $T_2^*$

As we saw in the previous section, the nuclear magnetic field fluctuates in time due to electron-nuclei hyperfine interaction and dipole-dipole interaction between nuclei.

An electron confined in a GaAs quantum dot interacts with approximately  $N = 10^6$  nuclei. Since  $k_B T \gg E_{z,nuc}$  the Boltzmann factors are all approximately equal and the average nuclear field is zero with a Gaussian distribution in all three directions given by [46, 59]:

$$B_{rms} = \sqrt{\frac{\langle |B_{nuc}|^2 \rangle}{3}} = \frac{h_1}{\sqrt{N}} \approx \frac{A}{g^* \mu_B \sqrt{N}}$$

with  $h_1$  the characteristic strength parameter. We note that for an electron confined in a quantum dot, the statistical fluctuations affecting the electron are stronger than for an electron in the 2DEG, since  $N$  is smaller.

The nuclear field distribution determines the shape of the coherence decay [51]. For a Gaussian distribution of  $B_{nuc}^z$ , the coherence decay is Gaussian as well and of the form  $e^{-\frac{1}{2}(t/T_2^*)^2}$  [46], where the ensemble coherence time  $T_2^*$  is:

$$T_2^* = \frac{\hbar}{g^* \mu_B \sqrt{\langle |B_{nuc}^z|^2 \rangle}}$$

In order to measure the ensemble coherence time, we average over many runs of a free induction decay type measurement (graphically illustrated in Fig. 2.11): the electrons are prepared in the  $(0, 2)S$  state, they are then separated fast to a value of  $\varepsilon$  where  $g^* \mu_B \Delta B_{nuc}^z \gg J(\varepsilon)$ . Under these conditions, the initial state in  $(1, 1)$  is a singlet, that evolves around  $\Delta B_{nuc}^z$  (i.e the  $x$ -axis of the Bloch sphere, see Fig. 2.8). After an evolution

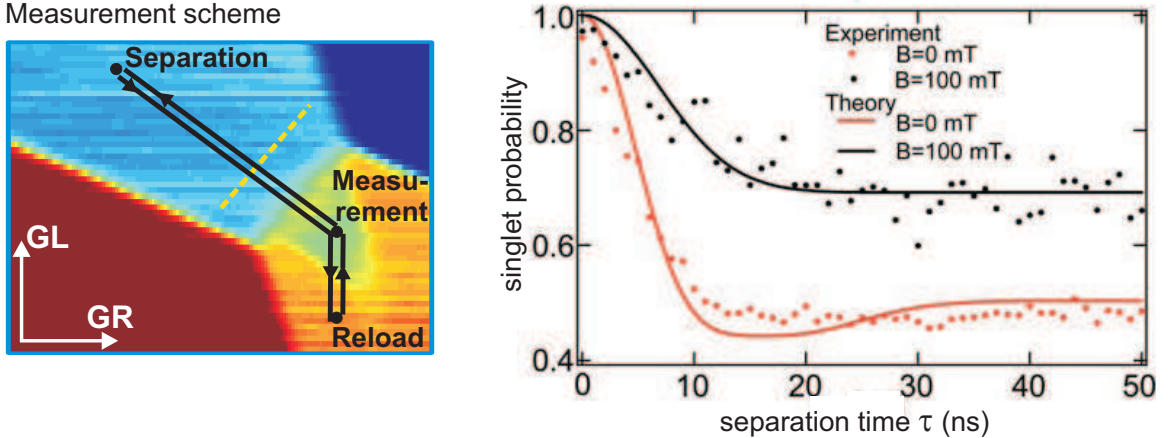


Figure 2.11: Measurement scheme used to determine  $T_2^*$ . The used pulse sequence is illustrated on a charge stability diagram (left hand side). The graph on the right hand side illustrates the probability of the state to be a singlet as a function of separation time  $\tau$  at two different values of magnetic field. Adapted from [13].

time  $\tau$  (on the order of 1-50 ns),  $\varepsilon$  is moved back fast to the (0,2) charge configuration for a measurement time on the order of 10  $\mu$ s. The measurement stage is followed by a reload of two electrons into a S(0,2) state and the whole pulse cycle is repeated. The probability of finding the state in a singlet after an evolution time  $\tau$  oscillates between 1 and 0. The same pulse sequence is run many times and each time the electrons are subjected to a different local magnetic field, i.e. the precession frequency  $f = \frac{g^* \mu_B \Delta B_{nuc}}{\hbar}$  is each time different. What is measured is the average signal over a large set of pulse sequences. The outcome shows the Gaussian decay of the probability to find the state in a singlet after an evolution time  $\tau$  (see Fig. 2.11). By fitting the experimental curve with a Gaussian decay the time  $T_2^*$  can be extracted. For quantum dots in GaAs  $T_2^*$  is on the order of 10 ns [13].

#### 2.4.4 Determining the coherence time $T_2$

The coherence time  $T_2$  is a very important figure, since the maximum number of gate operations is given by the ratio between  $T_2$  and the typical time necessary for one gate

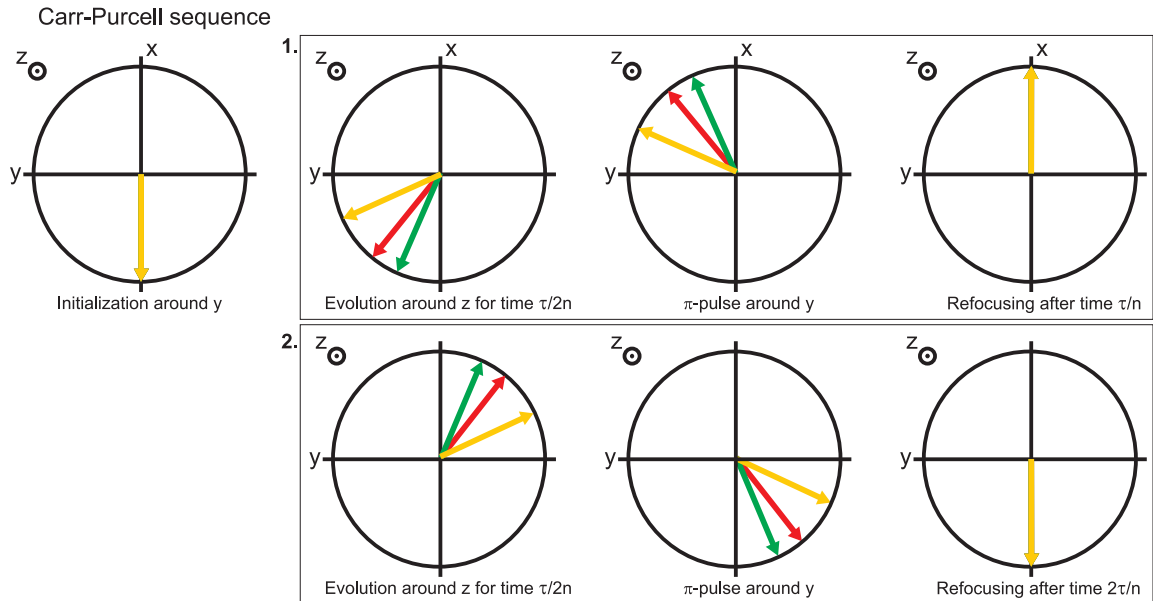
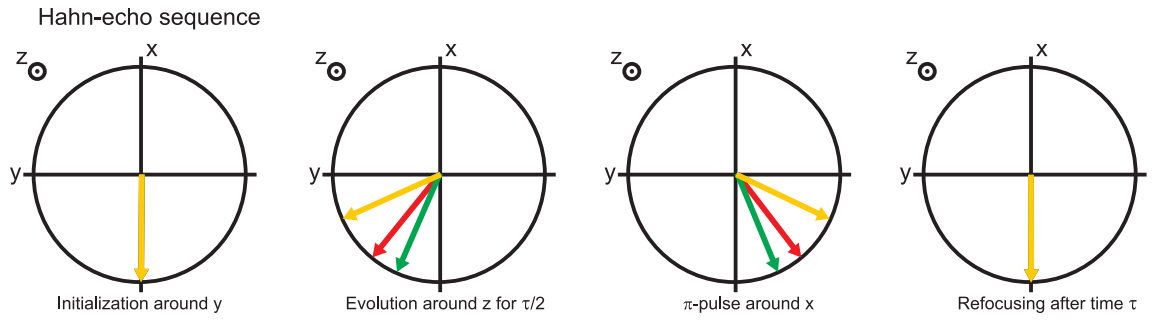
operation.

$T_2$  is the decay time that would be measured in a free induction decay type measurement for an ensemble of spins all subject to the exact same local magnetic field and thus typically longer than the ensemble decoherence time [59]. If the fluctuations that lead to an ensemble decoherence time  $T_2^*$  are slower than the time it takes to perform each single measurement, a trick can be used to extract the coherence time: use a so called Hahn-echo pulse [60] to determine  $T_{2,echo}$ . The main idea is to let the state evolve for a time  $\tau/2$  then apply a  $\pi$ -pulse in order to reverse the interaction, and then let the state evolve again for a time  $\tau/2$ . If the conditions before and after the  $\pi$ -pulse are equal, the initial state is fully recovered.

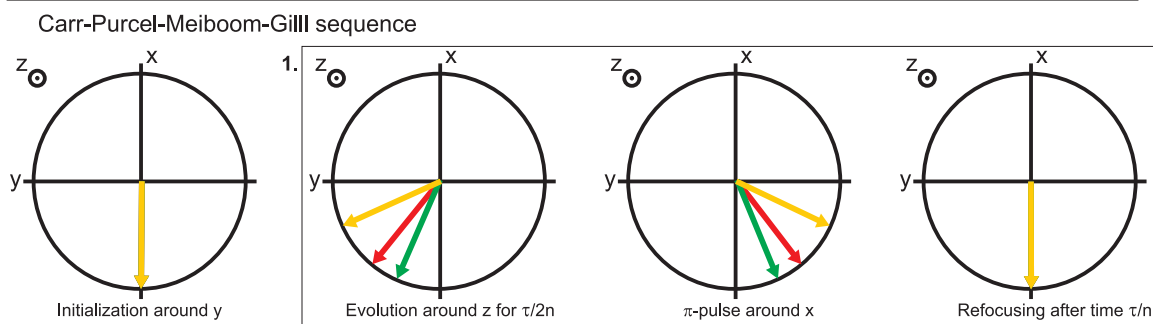
As mentioned above, what limits the coherence time are fluctuations of the nuclear magnetic field due to hyperfine interaction at low external magnetic fields and nuclear dipole-dipole interaction at high magnetic fields. The Hahn-echo decoherence time  $T_{2,echo}$  equals  $T_2$  only when the decoherence due to the dynamics of the electron spin and the nuclear bath can be treated within a Markovian approximation (i.e. not history dependent). Only in this particular case is the decay of the form  $e^{-\tau/T_{2,echo}}$ . In contrast in our system, because of the slowness of the bath and the effects of back-action of the electron on the bath, the decoherence time  $T_{2,echo}$  is different from  $T_2$  [14].

The Hahn-echo pulse however can not remove fluctuations with a typical time scale shorter than  $\tau$ . Carr and Purcell (CP) [61] introduced a sequence of  $n$  refocusing pulses, each one of length  $\tau/n$ , that can remove fluctuations much slower than  $\tau/n$ . This pulse sequence is thus less sensitive to higher frequency fluctuations than the simple Hahn-echo pulse.

The Carr-Purcell pulse sequence is affected by a systematic  $\pi$ -pulse error. Fig. 2.12 shows the scheme of a CP-sequence: the state is initialized into the  $xy$ -plane with a rotation



3. repeating the same cycle as shown in box1 for a total of  $n/2$  times



2. repeating the same cycle as shown in box1 for a total of  $n$  times

Figure 2.12: Illustration of the general schemes for the Hahn-echo, the Carr-Purcell and the Carr-Purcell-Meiboom-Gill pulse sequences.

around the  $y$ -axis. After an evolution time  $\tau/2$ , an imperfect  $\pi$ -pulse around the  $y$ -axis will rotate the state by  $\pi + \delta$ . After a second evolution time  $\tau/2$ , all states are refocused along

the  $-x$ -axis. Each subsequent  $\pi + \delta$ -pulse around the  $y$ -axis will effectively increase the error by  $\delta$ . The Carr-Purcell-Meiboom-Gill (CPMG) [62] is a slightly modified pulse sequence implemented to overcome the  $\pi$ -pulse error. In this case the first  $\pi/2$  initialization pulse and the  $\pi$ -pulses are not applied along the same axis as is the case for the CP pulse sequence. Rather, the state is initialized around the  $y$ -axis, but  $\pi$ -pulses are applied around the  $x$ -axis. Note that in this case, if we consider imperfect  $\pi$ -pulse (i.e.  $\pi + \delta$ ) the error of the second  $\pi$ -pulse always undoes the error on the first one.

Fig. 2.12 illustrates the Hahn-echo, the CP and the CPMG pulses as used in NMR [19]. In the particular case of our Hahn-echo experiment, the system is loaded into a  $S(0,2)$  state, and  $\varepsilon$  is moved to the  $(1,1)$  configuration fast compared to  $\Delta B_{nuc}^z$  in order to prepare  $S(1,1)$  as the initial state of the manipulation. The state then rotates around the  $x$ -axis of the Bloch sphere (presented in Fig. 2.8) for a time  $\tau/2$ . At this point  $\varepsilon$  is moved fast to a value  $J(\varepsilon) \gg g^* \mu_B \Delta B_{nuc}^z$  to induce a rotation around the  $z$ -axis. The rotation time has to be calibrated in advance, in order to perform a rotation of exactly  $\pi$ . After the  $\pi$ -rotation  $J(\varepsilon)$  is switched off fast, the state evolves again around the  $x$ -axis and the initial state  $S(1,1)$  is recovered after a total evolution time  $\tau$ , provided the electron is subject to the same environment before and after the  $\pi$ -pulse. For the CPMG pulses the same procedure is used. The Hahn-echo and the CPMG pulse sequence are employed for measurements presented in Chap. 7.

# Chapter 3

## Device fabrication

The samples used for all experiments presented in this thesis were fabricated in the clean room facility of the Braun Submicron Center at the Weizmann Institute of Science in Israel. The substrate used for the fabrication of lateral quantum dots is a GaAs/AlGaAs heterostructure grown with molecular beam epitaxy (MBE) technique (details of the structure were given in Chap. 2). In this chapter the fabrication procedure we used for sample preparation is described.

### 3.1 Defining the conducting region

A confined conducting region (the mesa) is defined via standard photolithography. Photoresist S1805 is spun on the wafer and baked to remove the solvent. A pattern on a glass mask (brought in close contact with the wafer) is transferred to the resist by illuminating the mask with UV light. Because S1805 is a positive resist the regions where the photoresist has been illuminated are removed faster by the developer than those covered by the mask. Fig. 3.1a shows the pattern on the mask that defines the mesa region. Once the mesa region to be is protected by photoresist, we dip the wafer into a standard GaAs etch

(see Appendix A for details) and remove material past the donor layer, such that only the central island (see Fig. 3.1a) is conducting due to the presence of a 2DEG, while all the remaining parts become insulating.

### 3.2 Ohmic contacts

The 2DEG, which lies about 100 nm below the wafer surface, has to be contacted in order to perform transport measurements. These ohmic contacts should fulfill the following requirements:

- They should present a linear I-V characteristic, i.e. they are an additional resistance in the bias circuit and should have the least possible influence in the device under consideration.
- They should be stable over time and under temperature changes.

For the fabrication of ohmic contacts, we use image reversal AZ5214E resist. After two steps of illumination (for details see Appendix A) and a development step we define regions free of resist. Image reversal is a negative tone resist and is usually used in conjunction with metal deposition because it ensures a profile undercut. The critical parameters for a satisfactory pattern transfer are the exposure time, the reversal bake temperature and the development time [63].

To contact GaAs/AlGaAs 2DEGs a gold-germanium eutectic alloy (88% gold, 12% germanium in weight), accompanied by an overlay of another metal such as nickel was found to fulfill the above mentioned requirements [64]. In our case the following metallization was used: 5 nm Ni, 200 nm Au, 100 nm Ge and 75 nm Ni. The total amount may be changed as long as the ratios are kept constant. After deposition, the resist is washed off in hot

acetone removing the metal deposited on the resist itself (commonly called lift-off process). Through an annealing process (50 sec at 460 °C in forming gas, Ar/H<sub>2</sub>, H<sub>2</sub> to prevent oxidation) the metal diffuses into the heterostructure. The nickel serves two purposes: it acts as a wetting layer, preventing AuGe from balling up when heating and it seems to help diffusion of germanium into the material. Gallium diffuses into the gold and germanium atoms can take the place of gallium atoms acting as donors [65].

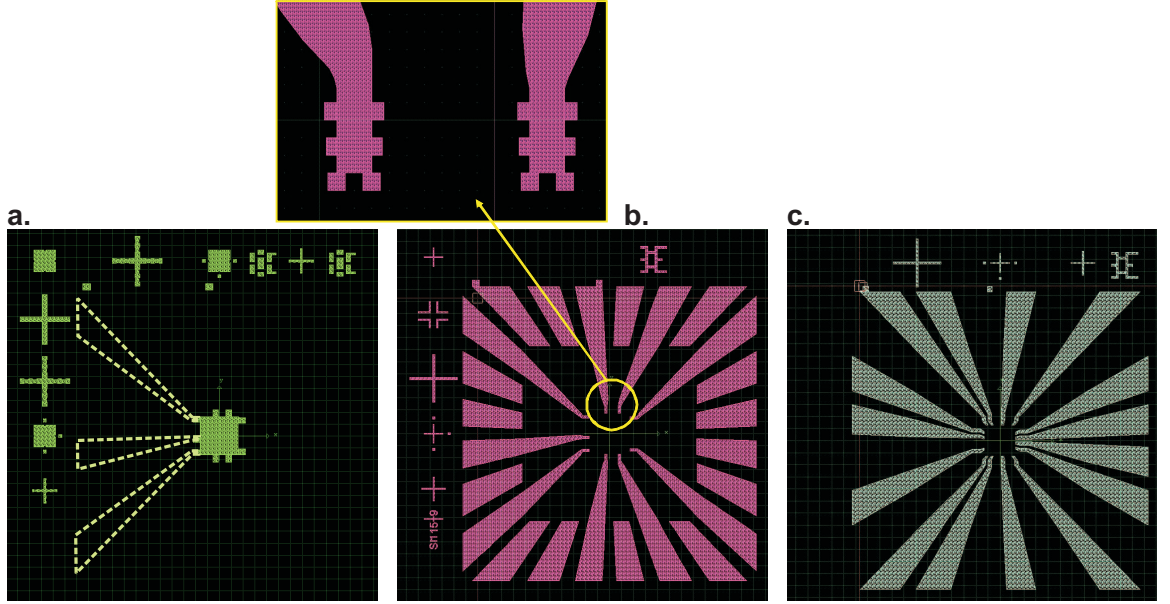


Figure 3.1: CAD drawings of the photolithography mask. a) The center square defines the conducting mesa, the surrounding region is made insulating by etching AlGaAs past the donor layer. The three dashed legs describe a second possible design, where the mesa region extends till the bonding pads. This particular geometry is less advisable, due to the larger resistance. On the sides various alignment marks are visible. b) Ohmic contact layout. The long legs reach the mesa square, where little rectangles with saw-tooth like edges overlap with the mesa region. It is important to deposit metal on the bonding pad region of all 24 contacts, such that the lowest metal layer of each bonding pad is annealed and thus more robust against peeling. c) Geometry of the optical gates that are used to contact the small e-beam gates to the bonding pads.

Although not fully understood, we noticed experimentally that the directionality of the edges of the ohmic contacts matters for the quality of the contacts (the same problem was encountered by other groups as well [66]). Following I. Neder's suggestion, the contacts are

designed with edges as shown in Fig. 3.1b. It is also important to have the ohmic contacts close to the mesa square and not just as bonding pads. Long “mesa legs” (as shown with dashed contours in Fig. 3.1a for three contacts) increase the number of squares, and thus increase the resistance unnecessarily.

When testing the device at room temperature a typical two terminal resistance is on the order of  $10\text{ k}\Omega$  (two ohmic contacts and mesa region in between). The resistance decreases to values below  $1\text{ k}\Omega$  when cooled to 4 K. This change in resistance as a function of temperature is mainly due to a resistance change of the 2DEG since phonon scattering decreases as a function of temperature, and not to a resistance change of the contacts.

### 3.3 E-beam and optical gates

Metal gates evaporated on the surface of the substrate allow one to locally deplete the 2DEG, in order to define small islands (the quantum dots). For our experiments the energy levels inside the quantum dots need to be quantized. This means that the typical dimensions of the structures have to be on the order of the Fermi wavelength of the electrons ( $\approx 50\text{ nm}$ ), requiring a fabrication step by means of electron beam lithography. Two layers of organic polymers PMMA<sup>1</sup> 200 K and PMMA 495 K (poly(methylmethacrylate)) are spun on the surface of the wafer and the desired patterns are defined with a focused electron beam. In the exposed regions the polymer chains are broken and washed off by the development solution of MIBK:IPA 1:3 (methyl isobutyl ketone:isopropyl alcohol). Employing a two-layer coating generates an undercut because the PMMA with lower molecular weight is more sensitive than the PMMA with larger molecular weight.

---

<sup>1</sup>PMMA is commonly used for plastic windows and one of the commercial names is Plexiglas.

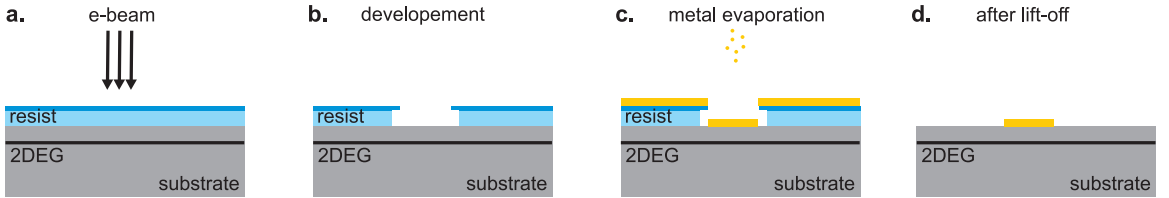


Figure 3.2: a) Two layers of PMMA, the most sensitive at the bottom, are spun on the surface of the wafer. Under e-beam exposure, the polymer chains are broken and are easily removed in the developer. b) After development. Being the bottom PMMA more sensitive, the resist assumes an undercut profile that facilitates lift-off after metal evaporation, because the resist side walls are not covered and acetone can penetrate and remove the resist. c) Metal is thermally or e-beam evaporated on the wafer surface and on the resist. d) After immersing the wafer in acetone for a few minutes, the resist is dissolved, whereas the metal deposited on the wafer surface remains.

We deposit 30 nm of PdAu, which has good adhesion properties to GaAs surfaces. An alternative is to use 15 nm of PdAu as an adhesion layer followed by another 15 nm of Au. Gold is typically chosen because of its chemical stability (e.g. it does not oxidize, a reaction that greatly reduces electrical conductance). After metal deposition, we lift-off with hot acetone (see Appendix A). Subsequent tests at Harvard have shown that for the deposition of such thin metal layers one single layer of PMMA 950 K still gives reliable lift-off. Difficult lift-off is usually the result of metal deposition on the side walls, preventing acetone from reaching the underlying resist.

Large optical gates (defined by optical lithography methods) are fabricated as a last step to connect the small e-beam gates to the bonding pads (for procedure details see Appendix A).

### 3.4 Few-electron quantum dot design

The challenge when designing few-electron quantum dots is to be able to create a structure where the electron number can be reduced to zero while the tunnel barriers are still trans-

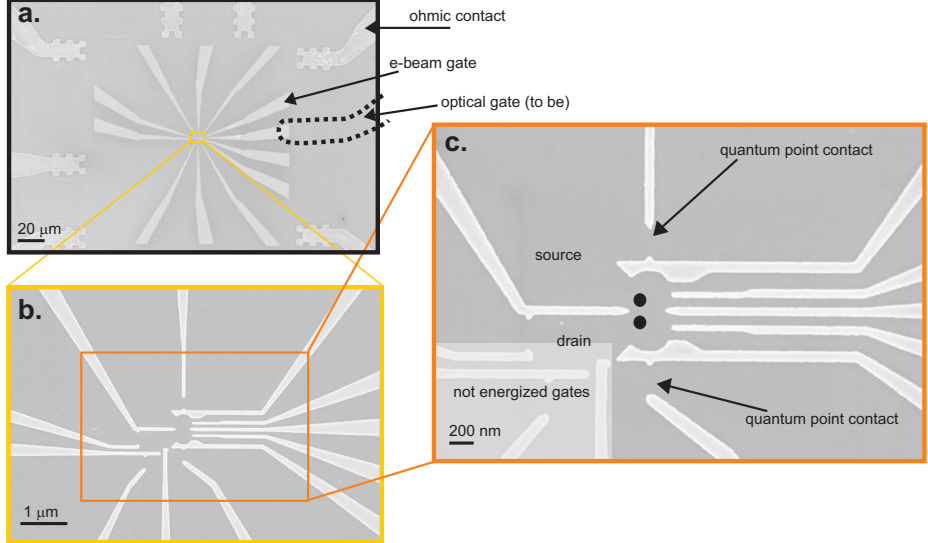


Figure 3.3: Three SEM micrographs of the device. a) Overview of the mesa region, where the ohmic contacts and the PdAu e-beam gates are visible. b) Zoom in on the central region. c) The quantum dots (schematically indicated by black circles) and the quantum point contacts are defined with PdAu gates 20-50 nm wide.

parent enough (i.e. the tunneling rate is not vanishingly small). Ciorga *et al.* [24] were the first to achieve this goal for single quantum dots.

In previous designs, source and drain were placed at opposite ends of the dot (schematically shown in Fig. 3.4a). In Ciorga's design (Fig. 3.4b), the two openings are close to each other so that the electron's wavefunction does not need to extend over the length of the entire quantum dot to overlap with both leads.

The double dot design we adopted had been previously used by the group of Prof. L. Kouwenhoven at Delft University and the group of Prof. C. Marcus at Harvard University. The big gates in the design of Fig. 3.4c are employed to define the dot's potential. The central gates control the tunnel barriers between the dots and the leads; the small plunger gates help in fine tuning the position of the dots with respect to the tunnel barriers (i.e. modifying the coupling). To have more independent control of the tunnel barriers to the leads one could envisage a splitting of the big gates into two parts: a big one used to define the

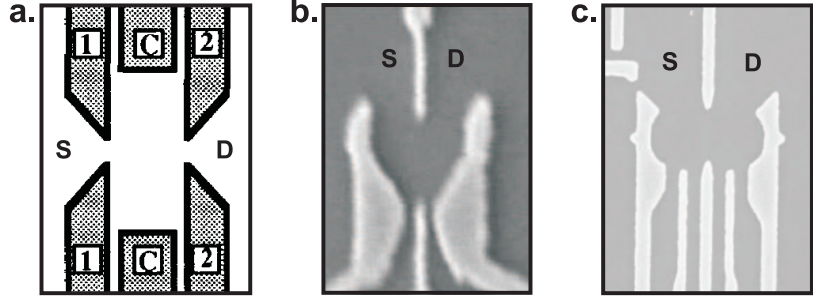


Figure 3.4: Quantum dots designs. a) Schematic of one of the early quantum dots, where source (S) and drain (D) are positioned on two opposite sides of the dot. Adapted from [23]. b) Quantum dots design allowing to reach the few electron regime, with source and drain contacts close to each other. Adapted from [24]. c) Double dot design similar to the geometry presented in b).

potential and a smaller one that allows to adjust the tunnel barrier transparency. Steps in this direction have been taken by C. Barthel in the group of Prof. C. Marcus [67].

### 3.5 Sample stability

A few iterations were needed in order to find a substrate that would both be easy to contact with standard AuGeNi ohmic contacts and be stable. In an unstable material, the measurement is disturbed by charge switches other than electrons leaving or entering the quantum dot studied. The switching events are probably related to traps in the donor layer being charged or discharged: these events change the electrostatic environment and shift the QD energy levels and modify the QPC conductance. In a stable material, over a time scale of days, not more than one or two switching events are seen.

One procedure that seems to help stability is to apply positive bias on the gates during cool down. In this way electrons are “frozen” in place underneath the gates and less negative voltages need to be employed to define the quantum dot. What also seems to help, is a relatively high aluminum content in the  $\text{Al}_x\text{Ga}_{1-x}\text{As}$  layer (in our case  $x = 0.36$ ). This

ensures a large bandgap, which renders the Schottky barrier between the gates and the substrate less transparent (i.e. preventing electrons to leak from the Schottky gates) [68].

## Chapter 4

# Experimental set-up and procedures

The technological challenge in performing spin qubit manipulations rests in two opposite requirements. On one hand, fluctuations of the quantum dot charge state should be negligible, requiring the thermal energy to be much smaller than the charging energy  $E_c \approx 1$  meV (see Sect. 2.2.2). For this reason, the measurements are carried out in a dilution refrigerator with typical base temperature of 10-100 mK. On the other hand, as the decoherence times that characterize our system are in the nanosecond to microsecond range, coaxial cables are indispensable to bring up to 1 GHz signals to the gates, adding thermal load to the dilution refrigerator.

We performed significant modifications on the Frossati dilution refrigerator already in use in our laboratory. We later designed and installed a similar set-up together with a high frequency read-out part in collaboration with David Reilly on a newly purchased Oxford dilution refrigerator. In this chapter the two measurement set-ups are presented.

## 4.1 Set-up in the Frossati dilution refrigerator with high frequency gate lines

The first system is a MiniKelvin 126-400  $^3\text{He}$ - $^4\text{He}$  dilution refrigerator from Leiden Cryogenics, commonly known as “Frossati fridge”, with a base temperature of 10 mK and cooling power of 400  $\mu\text{W}$  at 120 mK. It was modified at the Weizmann Institute and later shipped to Harvard.

### 4.1.1 DC wiring

In the Frossati fridge, lossy coaxes with resistance of about  $150 \Omega$  run from room temperature to the mixing chamber. Thermal anchoring is provided by embedding the wires into copper cylinders filled with Stycast tightly screwed to the different plates (as shown for the 1 K plate on Fig. 4.1b). From the mixing chamber to the sample holder manganin wires are employed.

Lines connecting to DC gates on the sample are filtered at three different stages:

- At room temperature we employed commercial  $\pi$ -filters (Mini Circuit BLP-1.9), that cut-off frequencies above 1.9 MHz.
- At the mixing chamber stage we employed sintered silver filters from Leiden Cryogenics. These filters are built in the following way: approximately half a meter of copper wire is wrapped around a small cylinder held between two SMX connectors. The wire is embedded in silver paint and sintered silver [69]. This provides capacitive coupling to ground and effectively filters frequencies above 1 GHz. These filters serve the same purpose as copper powder filters used by other groups [57].
- On the cold finger we employed RC-filters built with a capacitance to ground of 5 nF

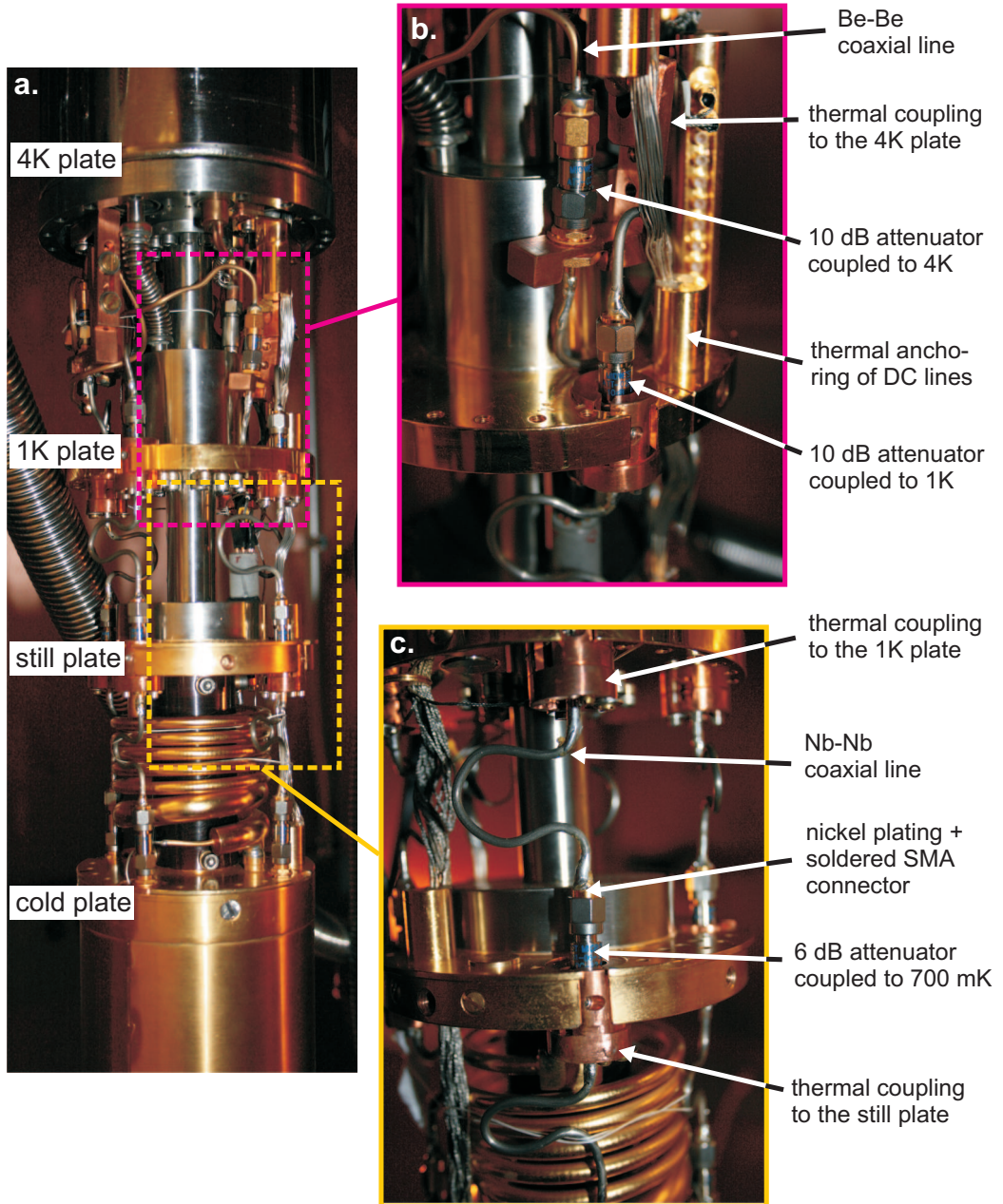


Figure 4.1: a) Overview of the dilution refrigerator insert with the installed high frequency lines. The different cooling stages (4 K plate, 1 K plate, still plate and cold plate) are indicated. b) Close-up of the thermal anchoring of the DC lines and the thermal anchoring of the beryllium copper coaxial lines to the 4 K plate. c) Close up of the niobium coaxial lines and the thermal anchoring to the 1 K plate. The cables are shaped into a half-loop to relieve stress from thermal contraction on the solder joints.

mounted on a printed circuit board (PC-board) in series with the wire resistance ( $\approx 150 \Omega$ ), giving a cut-off frequency of  $f = \frac{1}{2\pi RC} = 200 \text{ kHz}$ .

- On the cold finger the manganin wires are covered with silver paint, which acts as low pass filters.

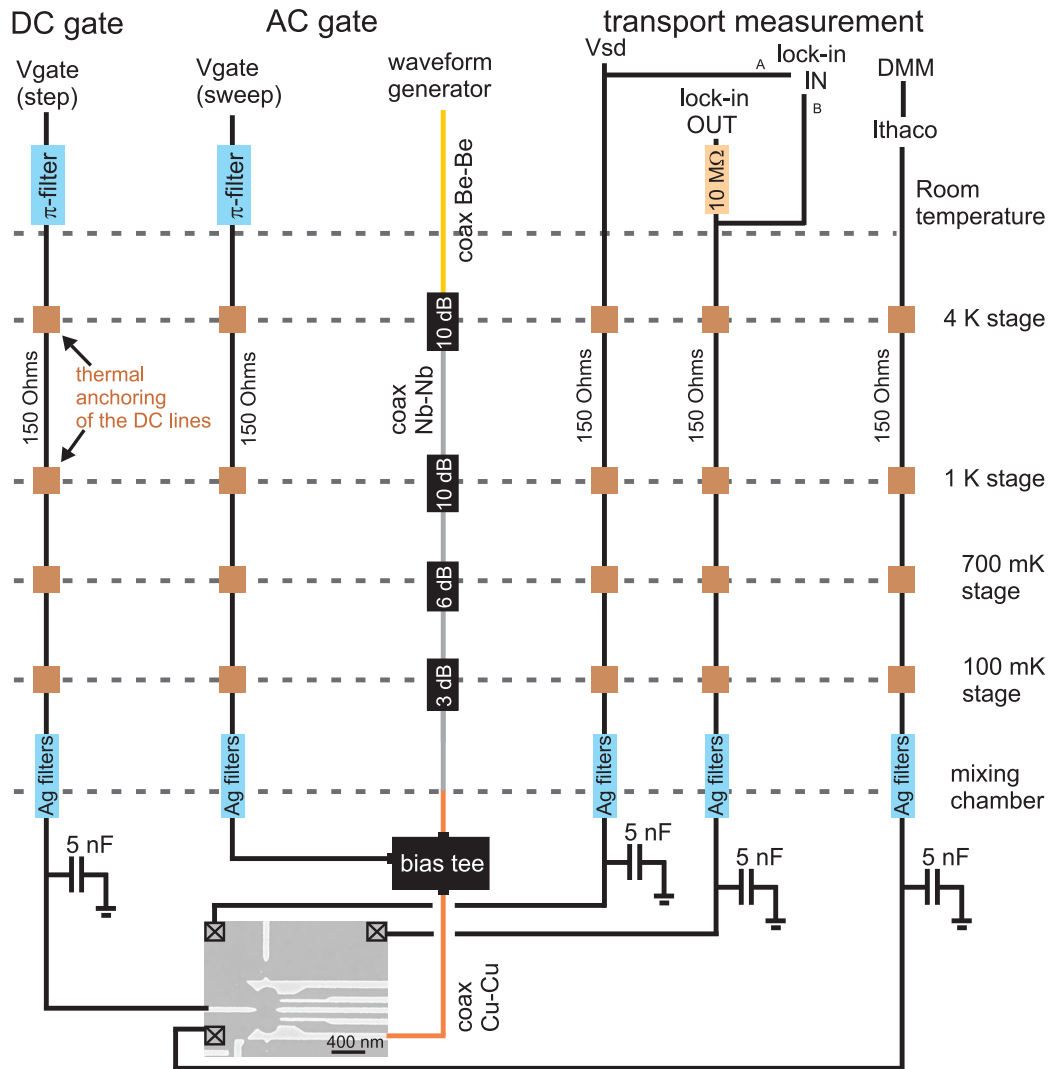
The lines connecting current and voltage probes to ohmic contacts on the sample are filtered in the same way, with the exception of the  $\pi$ -filters at room temperature, that are usually not used in this case, because the additional capacitance to ground affects the phase and reduces the amplitude of the lock-in excitation signal.

Low frequency transport measurements are of two kinds: current biased lock-in measurements of the QPC conductance ( $I_{QPC} = 1 \text{ nA}$ ) and DC voltage biased measurements of the double quantum dot for tuning (for details see Fig. 4.2 and Appendix B). DC voltages at the gates were initially applied with voltage sources from Yokogawa and later with a 16-channel DAC (Decadac) developed and assembled by Jim MacArthur from the Harvard electronic shop. All voltages were downconverted to a range between 0 to  $-1 \text{ V}$  with a 1:10 voltage divider.

#### 4.1.2 High frequency gate lines

A crucial point to consider for coax lines is the frequency response of the conductor material. The attenuation due to conductor losses is proportional to the surface resistance  $R_s = \frac{1}{\sigma\delta_s} = \sqrt{\frac{\omega\mu_0}{2\sigma}}$ , the resistance of the conductor whose effective thickness is the skin depth  $\delta_s = \sqrt{\frac{2}{\omega\mu_0\sigma}}$ , where  $\mu_0$  is the vacuum permittivity and  $\sigma$  the electrical conductivity [70]. For minimal attenuation, one would choose a coax with the highest possible electrical conductivity. The cable attenuation at a frequency  $f$  is linearly proportional to its length  $l$  and inversely proportional to the diameter of its inner conductor  $d$ :  $\frac{l}{d}\sqrt{\frac{f}{\sigma}}$  [71].

A second important issue is the thermal anchoring of both the inner and outer conductor,



- $\pi$ -filter: Mini Circuit BLP-1.9 (DC-1.9 MHZ)
- Ag filters: sintered silver filters, Leiden Cryogenics
- XX dB: XX dB attenuator Midwest Microwave ATT-276F-XX-SMA-02
- coax Be-Be: coaxial cable UT-85 B-B, Microstock
- coax Nb-Nb: coaxial cable UT-219/50-Nb-Nb, Nippon Cryogenic Ldt.
- coax Cu-Cu: UT 34C semirigid coaxial cable, Microstock
- Waveform generator: Tektronix Arbitrary Waveform Generator AWG520
- Vgate (step): DecaDac from Harvard electronic shop designed by Jim MacArthur
- Vgate (sweep): Yokogawa 7651 programmable voltage source or DecaDac
- Lock-in: Stanford research system SR830 DSP lock-in preamplifier
- Ithaco: 1211 current preamplifier, DL Instruments
- DMM: Digital Multimeter Agilent 34401A

Figure 4.2: Wiring scheme of the Frossati dilution refrigerator. Electrical circuit used for simultaneous current biased lock-in measurement of the QPC conductance as well as DC transport measurement through the dot (employed for its tuning). The left hand side of the scheme shows the electric circuit necessary to apply both DC and AC (MHz to GHz) voltages to the gates.

in order to cool the electrons to the base temperature of the dilution refrigerator on their way down to the sample. To provide thermal anchoring of the outer conductor at different temperature stages (4 K, 1 K, still and coldplate) bulkheads are tightly screwed to copper plates connected to the different cooling stages (see Fig. 4.1b and c).

For the inner conductor, two 10 dB, a 6 dB and a 3 dB attenuator are mounted to the 4 K, the 1 K, the still and the cold plate, respectively. Attenuators are very similar to voltage dividers, where a finite resistance to ground allows for thermal coupling of the inner conductor [70]. As a rule of thumb the attenuation factor should be approximately equal to the temperature ratio between the stage on which they are mounted and the previous one [71]. It should also be noticed that the 4 K stage, the 1 K stage and the still provide a larger cooling power than the mixing chamber. Attenuators with large attenuation factors and power dissipation should thus be thermally anchored at those stages.

Between the different temperature stages, different kinds of coaxial lines were used:

- From the top of the fridge (room temperature) until the 4 K plate: 0.085" semi rigid beryllium copper-beryllium copper (inner and outer conductor) coaxial cables were employed. We chose beryllium copper to maximize the bandwidth even though its thermal conductivity is 10 time as high as that of stainless steel for example. Calculations showed that this would not contribute to the thermal load of the 4 K stage.
- From the 4 K plate until the mixing chamber: 0.085" semirigid superconducting niobium-niobium coaxial cables were used. Niobium coaxial cables where chosen because as a superconductor they are very good electrical conductors but poor thermal conductors (the critical temperature is  $T_c=9$  K). Niobium remains superconducting also when applying an external magnetic field smaller than the critical field for nio-

bium,  $B_c=2.5$  T. Although it is only for temperatures below 100 mK that niobium's thermal conductivity is lower than stainless steel's [71, 72], niobium coaxes have lower attenuation. For instance the cut-off for 40 cm of 0.085" SS-SS coaxial line is about 4 GHz [73].

- From the mixing chamber until the sample holder 0.034" semi rigid copper-copper coaxial lines were employed in order guarantee good thermal connection to the mixing chamber.

From a technical point of view niobium is not easy to solder to. The soldering of the SMA connectors to the coax lines required nickel coating of the inner and outer conductor. The nickel coating was done with a metalization pen (PL-1006, Hunter products). For the second measurement system (presented in the following section) we exclusively used crimp connectors.

The high frequency lines connect the two large plunger gates on the double dot structure (as shown for one of them in Fig. 4.2) to an arbitrary waveform generator (Tektronix AWG520) that can be programmed with a desired sequence of pulses for fast electron manipulation.

#### 4.1.3 The cold finger

The cold finger holds the sample such that it is thermally connected to the mixing chamber (i.e. as close as possible to the mixing chamber temperature) and in the center of the magnet bore. This cold finger is made out of a single copper piece (alloy 101, oxygen free electronic grade) and tightly screwed to the mixing chamber.

Just below the mixing chamber, commercial bias tees (Anritsu K251) which add high frequency signals on top of a DC bias, are mounted and thermally connected to the cold-

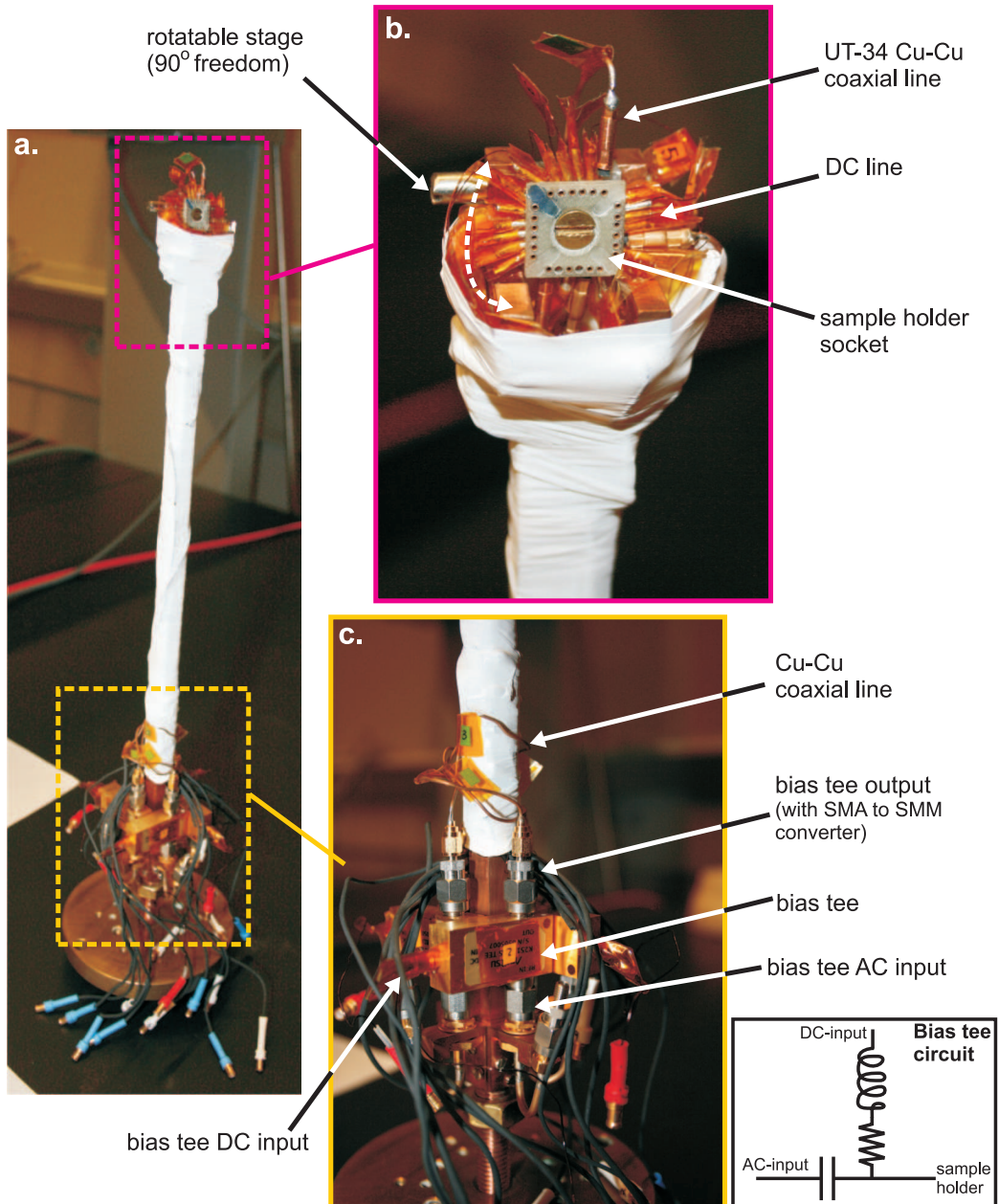


Figure 4.3: a) Cold finger, basically 1 cm square copper rod. b) Close up of the sample holder, the coaxial lines and the DC lines connected to pins. The screw on the left side can be removed to rotate the stage. c) Close up of the upper part of the cold finger with the bias tees. The equivalent circuit of the bias tees is shown in the inset.

finger. After the bias tees the coaxial lines reach directly the sample holder, where the inner conductors are soldered to the side-wall of a pin connector. A weakness of this design is that the outer conductor is not grounded to a well defined RF ground at the sample holder,

which can lead to pulse distortions.

The DC lines between the mixing chamber to the sample holder are manganin wires and are glued to the copper-skeleton with silver paint. At the sample holder side, they are soldered to the same type of pins as the high frequency lines. These are inserted into a square shaped G10-plate which serves as socket (as shown in Fig. 4.4). The legs of the chip carrier are later inserted into the pins.

The head of the cold-finger can be rotated to position the sample at different angles with respect to the applied magnetic field: the sample stage angle must be set to the desired value before cool-down. The pins are removable, allowing one to change the position of the coaxial lines on the sample holder. This design is not very convenient, despite its flexibility. When rotating the head of the cold finger the coaxial lines regularly disconnected from the pins, and re-soldering was necessary. It is advisable to have the coaxial lines connected in a more permanent and stable way and to adjust the bonding scheme as needed.

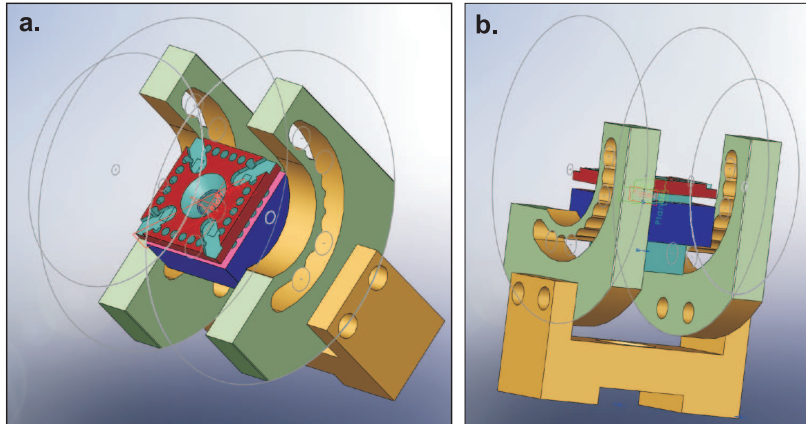


Figure 4.4: a) Front view of the sample holder. b) Back view of the sample holder that can be set to 10 different inclinations between 0 and 90°.

Once the coaxial lines and the cold finger were mounted, the electron temperature was measured with both a quantum dot and a metallic single electron transistor (SET) fabricated by B. Verdene. From fits of the Coulomb blockade peak width, the electron temperature

was determined to be about 100 mK. This temperature is slightly higher than the electron temperature obtained using a standard cold finger without coaxial lines ( $T_e = 60$  mK) in the same dilution refrigerator.

The sample holder was a commercial gold plated 24 pin connector without magnetic materials, no longer in production.

## 4.2 Set-up in the Oxford dilution refrigerator with high frequency gate lines and RF read-out

The second system is a Kelvinox MX50  $^3\text{He}$ - $^4\text{He}$  dilution refrigerator from Oxford Instruments with a base temperature of 25 mK and cooling power of 50  $\mu\text{W}$  at 100 mK.

### 4.2.1 DC wiring

From room temperature to the mixing chamber a loom of constantan (a copper and nickel alloy) is employed. Thermal anchoring is achieved by wrapping the loom around copper posts at different cooling stages. A copper loom is employed from the mixing chamber to the sample.

Lines connecting to DC gates are filtered at various stages:

- At room temperature we employed commercial  $\pi$ -filters (Mini Circuit BLP-1.9), that cut-off frequencies above 1.9 MHz.
- At the top of the cold finger we employed capacitive filters inside a commercial D-sub connector (Cristek FMD-1D-0N5CH) that filters noise above 10 MHz.
- On the sample holder we employed 100 pF to ground mounted on the PC-board (chip holder) in series with the wire resistance giving a cut-off frequency of about 10 MHz.

It has later been substituted with a  $10\text{ nF}$  capacitance together with a  $2\text{ k}\Omega$  resistor on the DC line, giving a cut-off frequency of about  $8\text{ kHz}$ .

The lines connecting current and voltage probes to ohmic contacts on the sample are filtered the same way, with exception of the  $\pi$ -filters at room temperature, that are not used in this case.

#### 4.2.2 High frequency gate lines

The high frequency lines to the pulsed gates are attenuated at three stages: at the  $1\text{ K}$  plate, at the cold plate and at the mixing chamber with  $20\text{ dB}$ ,  $10\text{ dB}$  and  $3\text{ dB}$ , respectively. The slightly different choice and location of the attenuators compared to the previous set-up is due exclusively to the different configuration and space availability inside the dilution refrigerator.

The coaxial lines used from room temperature to the mixing chamber are made of stainless steel (UT-85 SS-SS). Being a poor thermal conductor, stainless steel is employed to reduce the thermal load on the dilution unit. As previously mentioned, the cut-off frequency of these stainless steel coaxial lines is on the order of a few GHz, sufficient to perform the experiments: noise at higher frequencies is cut-off. If a larger bandwidth is needed, one would use niobium coaxial lines. From the mixing chamber to the sample holder, copper coaxial lines (UT-34 C) are used.

The commercial bias tees used in the previous set-up, and employed before us by other groups [13, 73] cause resonances in the lines that lead to pulse distortions. In this second set-up we employed home-made bias tees differing from the commercial ones by the absence of inductors on the DC line (as schematically shown in Fig. 4.8). Their performance was equally good, with no pulse distortions and a more accurate voltage compensation.

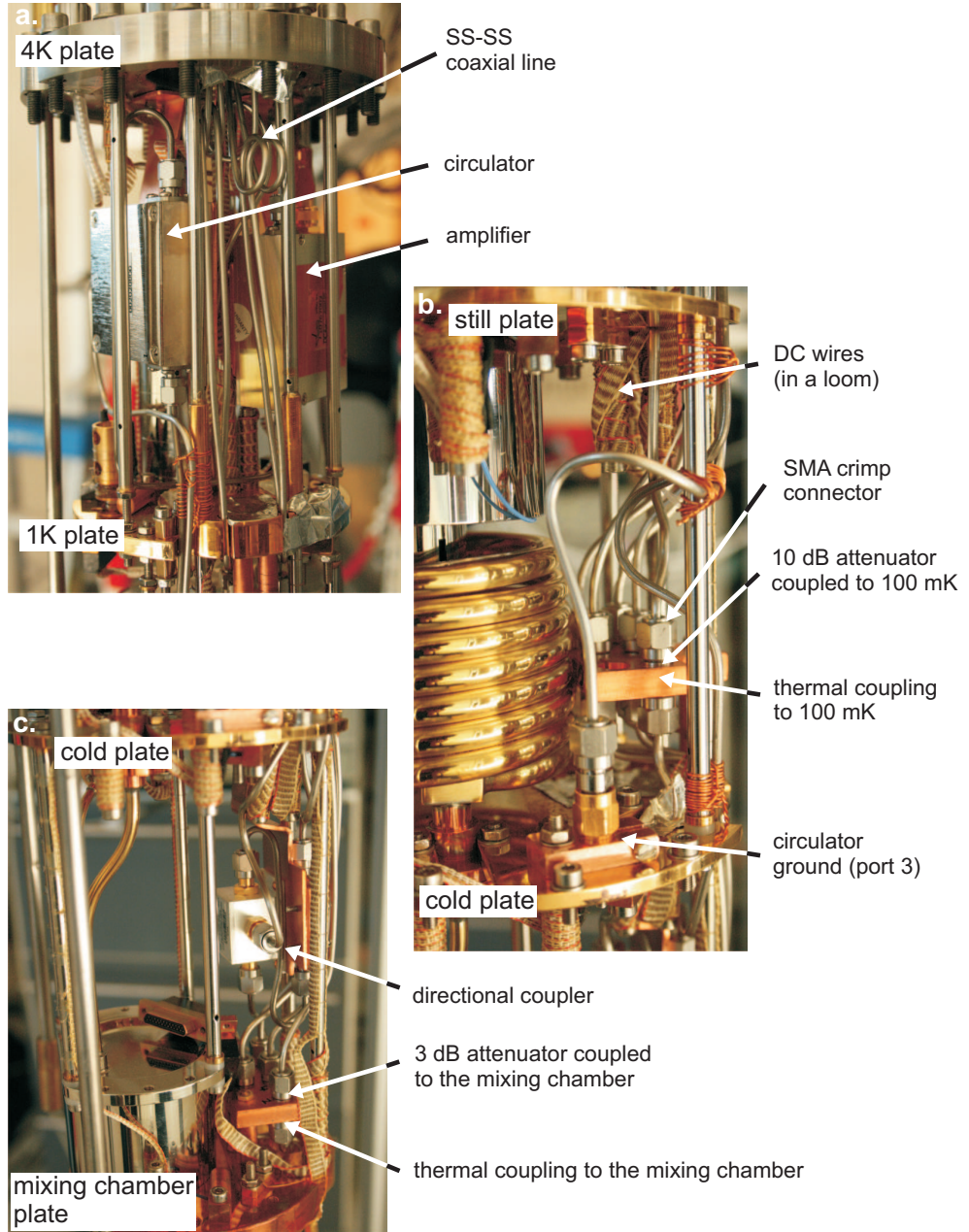
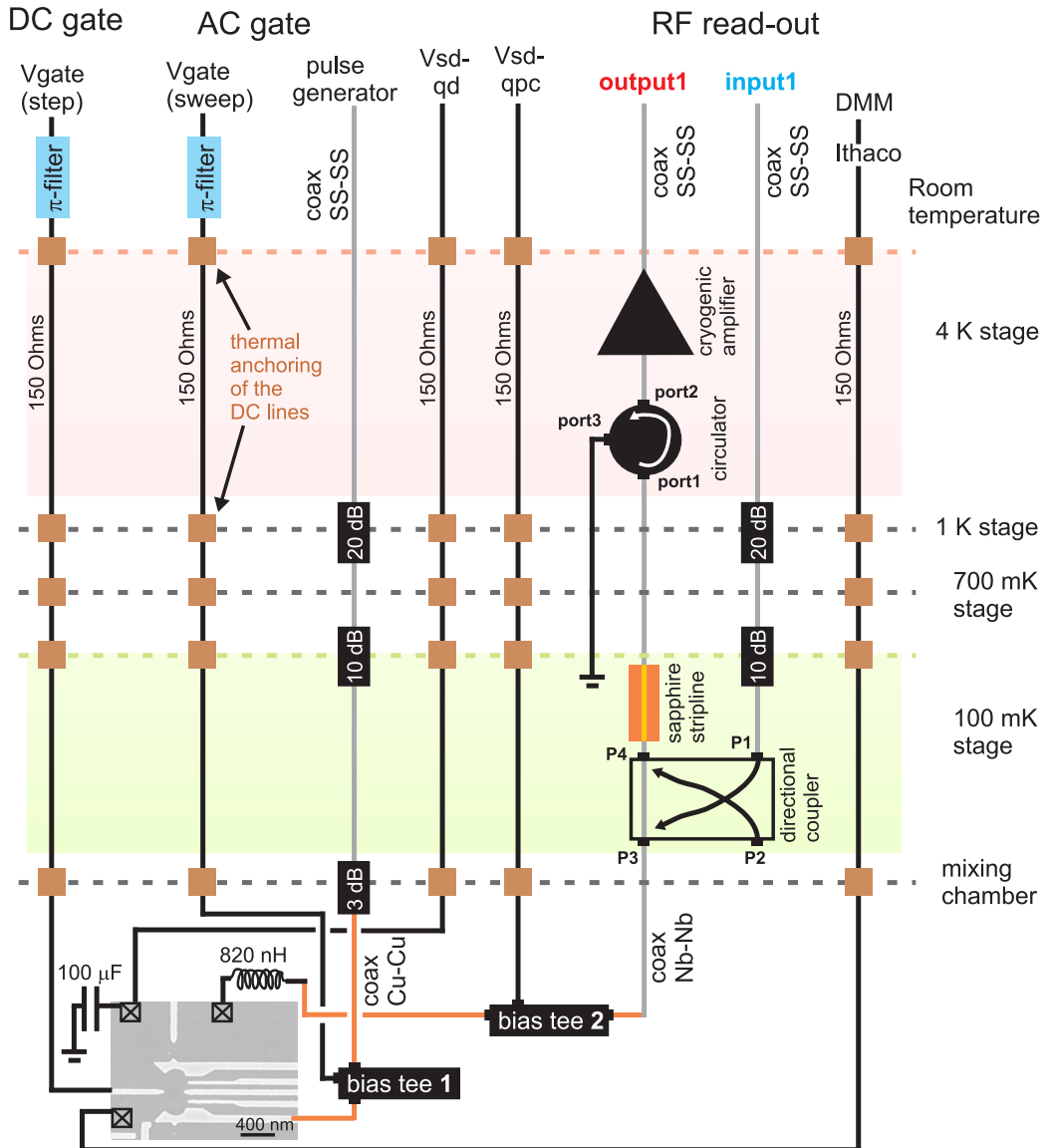


Figure 4.5: Pictures of the wiring of the MX50-dilution refrigerator. a) Upper part (4 K to 1 K stages) of the dilution refrigerator insert with the stainless steel coaxial lines coming down from the top of the dilution refrigerator. On these lines used for RF read-out, a circulator and an amplifier are mounted and thermally anchored to the 4 K stage. b) The third port of the circulator is anchored to ground at the cold plate (100 mK). Attenuators provide cooling of the gate lines' inner conductor: they are clamped by copper block for thermalization. The loom with DC wires is wrapped around copper posts at different stages. c) The directional coupler is thermally anchored to the cold plate. The last stage of attenuators on the gate lines is thermally anchored to the mixing chamber.



- Coax SS-SS: provided with the MX-50 Oxford dilution refrigerator
- Directional coupler: Mini Circuit ZEDC-15-2B
- Circulator: cryogenic circulator without magnetic shielding, 220-240 Hz, Quinstar QCY-002020U00
- Amplifier: cryogenic amplifier, center frequency 230 MHZ, bandwidth 50 MHZ Quinstar QCA-U-230-30HZ1, amplification 45 dB (with power supply PS-3D, ps-connector: [www.mmm-microtech.com](http://www.mmm-microtech.com) EP-7S-1)

Figure 4.6: Wiring scheme of the MX50-dilution refrigerator used for RF read-out measurements. The details of input1 and output1 are explained in Fig. 4.7. The circuits used for bias tee 1 and bias tee 2 are explained in detail in Fig. 4.8. On the left hand side of the scheme the electric circuit necessary to apply both DC-voltages on the gates and change the gate voltages on a MHz-GHz time scale is shown.

In this second measurement system we exclusively used crimp connectors, that are easier to handle and whose quality is not affected by repeated thermal cycling (Tyco electronics, SMA connectors: 1050611-1, crimp tool: 1055835-1).

#### 4.2.3 RF read-out

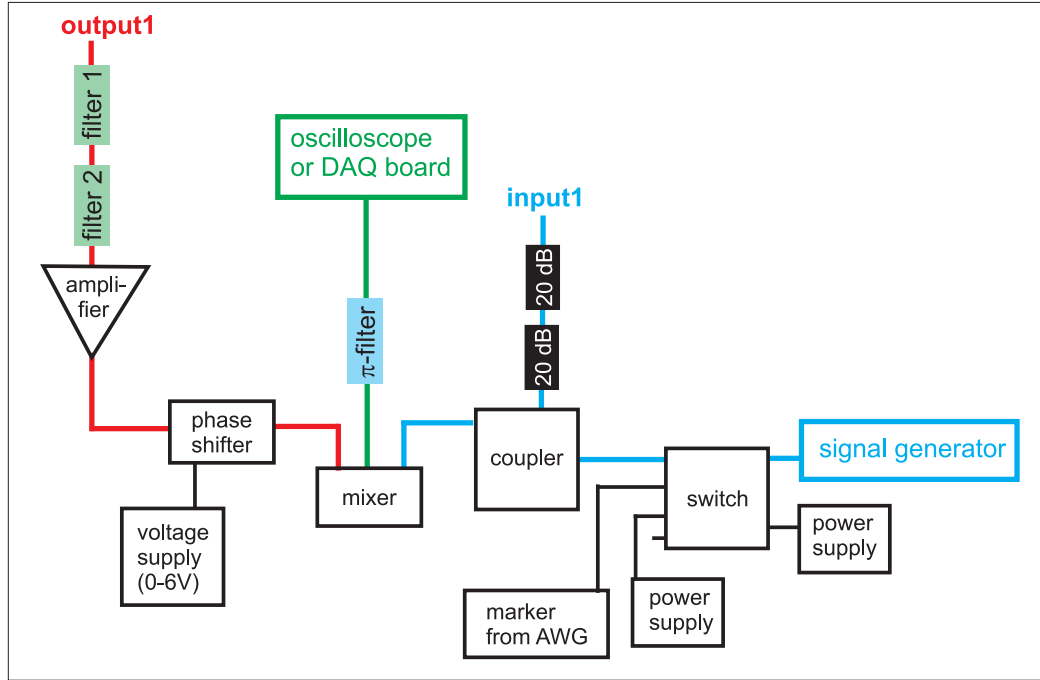
The typical DC-lines used in dilution refrigerators are several meters long and have thus non-negligible stray capacitance. This capacitance, combined with the sample resistance results in an RC-time constant that limits the measurement bandwidth to a few hundred kHz [74].

At the end of the 1990's a new technique has been successfully employed for SET's (single electrons transistors): the extraordinary properties of charge sensitivity and response time of the SET could be exploited by embedding the SET in an impedance matching circuit [75]. Reilly *et al.* [76] and Cassidy *et al.* [77] recently demonstrated that the same technique can be employed for QPCs. Our RF read-out set-up is based on David Reilly's design [76] with the addition of a circulator [75, 78].

#### Input signal

Figs. 4.6, 4.7 and 4.8 show the complete set-up used for measurements with RF read-out. A signal generator sends a signal (the carrier, with power 5-8 dBm) to input1 through a switch, a coupler and two 20 dB attenuators. The switch, triggered by a marker from the arbitrary waveform generator, allows us to switch the amplitude of the carrier on and off, for example, to turn off the signal on the QPC during qubit manipulations (see Ch. 7). The coupler splits the carrier signal into two, one towards input1, the other towards a mixer (the use of which will be explained in the following). According to the specifications, the

ideal operating point of the mixer requires a carrier with 13 dBm power, but even a lower choice of power did not affect the proper functioning of the mixer.



- filter 1: band pass filter SHP-50+ (41-800 MHz)
- filter 2: low pass filter SLP-450+ (DC-400 MHz)
- phase shifter: Pulsar SO-06-411
- mixer: Mini-Circuits ZP-3MH (0.15-400 MHz)
- switch: Mini-Circuits ZASWA-2-50DR+ (DC-5 GHz)
- coupler: Mini-Circuits ZEDC-15-2B
- amplifier: Miteq Inc., AU-1565-11795C (0.01-400 MHz), 55 dB amplification
- coupler: Mini-Circuits ZEDC-15-2B (1-1000 MHz)
- signal generator: HP ESG 1000A (1GHz)
- oscilloscope: Tektronix TDS5104B Digital phosphor oscilloscope (1 GHz, 5GS/s)
- DAQ board: ATS660 Alazar Technologies Inc. (130 MS/s, 2 channels, 8 MS per channel, 16 bit)

Figure 4.7: The signal generator outputs a carrier signal that is blocked by the switch on demand (see Chap. 7). The signal is then fed to a coupler, that divides the signal into two. One part is attenuated by 40 dB and fed into input1, the other part is sent to a mixer. The output signal is amplified by 55 dB. The phase of the signal is adjusted with a phase shifter, such that it is in phase with the input signal. The signal is then demodulated before being measured by the oscilloscope.

The stainless steel high frequency line runs from input1 to the cold plate with a 20 dB attenuator for the thermalization of the inner conductor at the 1 K plate and a 10 dB attenuator at the cold plate. At the cold plate the carrier is fed into a directional coupler. The directional coupler is a 4-port passive element consisting of two microstrips connecting

directly port P1 to port P2 and P3 to P4 [70]. The two microstrips are weakly coupled by electromagnetic radiation and a small amount of signal from P1 is coupled into P3 but ideally not into P4 (and vice versa from P2 into P4 but not P3). We use the coupler in the following way: the input signal is fed into P1, and P2 is  $50\ \Omega$  terminated. This signal is partially coupled to P3 that goes to the sample. The reflected signal from the sample is directly coupled to P4 and only a small amount is lost into P1. We use such an asymmetric coupler with small coupling and a large signal from the waveform generator because the dissipation at port P2 is not a concern, but preserving the signal from the sample is.

After the directional coupler the circuit continues with a copper coaxial line ending on a  $50\ \Omega$  stripline on a specially designed PC-board (shown on Fig. 4.8). At the end of the stripline (very close to the sample) a bias tee adds DC and AC signals. The signal reaching the sample has been attenuated by about 100 dB.

### **Tank circuit properties**

Given the high resistance of the QPC, it is necessary to transform its impedance to match the  $50\ \Omega$  of the transmission line. Failing to do so causes the RF probing signal to be completely reflected independently of the QPC resistance, as if it was an open circuit. This can be done using an LCR circuit (also called *tank circuit*) that transforms the impedance at a particular frequency. The inductance  $L$  is provided by a chip inductor of 820 nH (Coilcraft 1206CS-821XL) mounted on the PC-board close to the sample (shown in Fig. 4.8). The capacitance  $C$  is mostly parasitic capacitance (i.e. stray capacitance from the inductor and from the bond pads to ground) estimated to be on the order of 0.5 pF.  $R$  is the sample resistance and in our case  $50\text{ k}\Omega$  at matching.

The measured quantity is the reflected power, the ratio between the injected and the

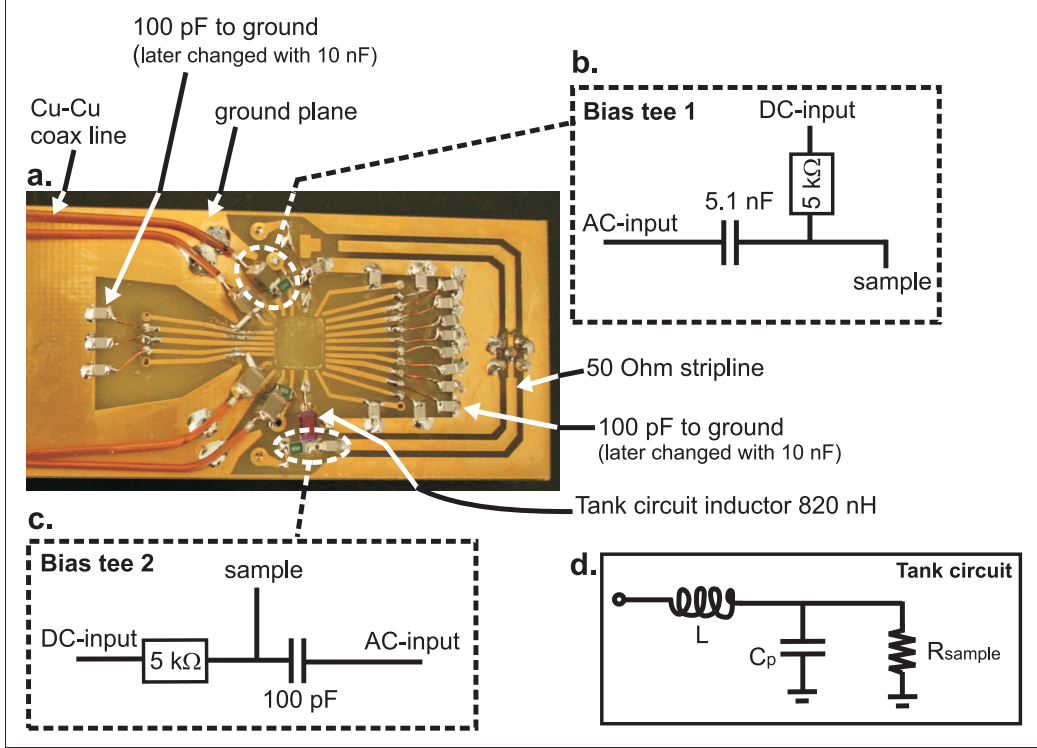


Figure 4.8: a) Close up on the PC-board designed as sample holder. Visible are the copper coaxial lines for gate pulsing as well as the  $50 \Omega$  stripline in which the coaxial line for RF read-out terminates. b) Bias tee circuit used on the RF read-out circuit, with a resistor on the DC input and a capacitor on the AC input. c) Bias tee used on the high frequency gate lines. d) Scheme of the tank circuit, needed for impedance matching of the quantum point contact.

reflected *average* power:

$$|\Gamma(\omega)|^2 = \frac{\frac{|V_0^-|^2}{2Z_0}}{\frac{|V_0^+|^2}{2Z_0}} = \left| \frac{Z_{LCR} - Z_0}{Z_{LCR} + Z_0} \right|^2$$

where  $Z_0 = 50 \Omega$  is the characteristic coaxial line impedance,  $V_0^+$  ( $V_0^-$ ) the voltage amplitude of the incoming (outgoing) signal. The total impedance of the circuit is given by [73]:

$$Z_{LCR}(\omega) = j\omega L + \frac{1}{\frac{1}{R} + j\omega C} = \frac{R}{1 + (\omega RC)^2} + j\omega L \left[ 1 + \frac{R^2 C / L}{1 - (\omega RC)^2} \right]$$

At resonance all power is delivered to the load, so that current and voltage are in phase and  $\text{Im}\{Z_{LCR}\} = 0$ . The resonance occurs at

$$\omega_0 = \sqrt{\frac{1}{LC} - \frac{1}{R^2C^2}} \approx \frac{1}{\sqrt{LC}}$$

the approximation holding for  $R \gg Z_{LC} = \sqrt{\frac{L}{C}}$  (i.e.  $\omega_0 RC \gg 1$ ). This is the case for our typical parameters  $R \approx 50 \text{ k}\Omega \gg \sqrt{\frac{L}{C}} \approx \sqrt{\frac{1 \mu\text{H}}{1 \text{ pF}}} = 1 \text{ k}\Omega$ .

The impedance at resonance is thus given by :

$$Z_{LCR}(\omega_0) = \frac{R}{1 + (\omega_0 RC)^2} = \frac{L}{RC}.$$

An important figure of merit of the circuit is the bandwidth, which characterizes the quality factor of the resonant circuit. The quality factor, defined as the energy stored divided by the energy dissipated per cycle, is given by  $Q_{load}$ , defined as (following [79]):

$$\frac{1}{Q_{load}} = \frac{1}{Q_{ext}} + \frac{1}{Q_{no-load}} = \frac{Z_0}{Z_{LC}} + \frac{Z_{LC}}{R}$$

where  $Q_{ext} = \frac{R}{Z_{LC}}$  and  $Q_{no-load} = \frac{Z_{LC}}{Z_0}$ .

In order to understand the functional dependence of  $\Gamma(\omega)$ , we do a Taylor expansion around the resonance frequency  $\omega_0$  and the matching resistance  $R_0 = \frac{Z_{LC}^2}{Z_0}$ :

$$Z_{LCR}(\omega) \approx Z_0 \left( 1 - \frac{R - R_0}{R_0} \right) + 2jZ_{LC} \frac{\omega - \omega_0}{\omega_0}$$

Using this approximation, the voltage reflection coefficient becomes:

$$\Gamma(\omega) \approx \frac{Z_0 \frac{R_0 - R}{R_0} + 2jZ_{LC} \frac{\omega - \omega_0}{\omega_0}}{2Z_0 + 2jZ_{LC} \frac{\omega - \omega_0}{\omega_0}} \quad (4.1)$$

At matching condition  $R = R_0$ , the reflected power becomes:

$$|\Gamma(\omega_0)|^2 \approx \left| \frac{j \frac{\omega - \omega_0}{\omega_0}}{j \frac{\omega - \omega_0}{\omega_0} + \frac{1}{Q_{no-load}}} \right|^2$$

This has a Lorentzian shape and equals 1 far away from  $\omega_0$  (all signal is reflected) and 0 at resonance (all signal is delivered to the load), see Fig. 4.9a. Its full width at half maximum

is

$$\Delta f_{FWHM} = \frac{\omega_0}{2\pi Q_{load}}. \quad (4.2)$$

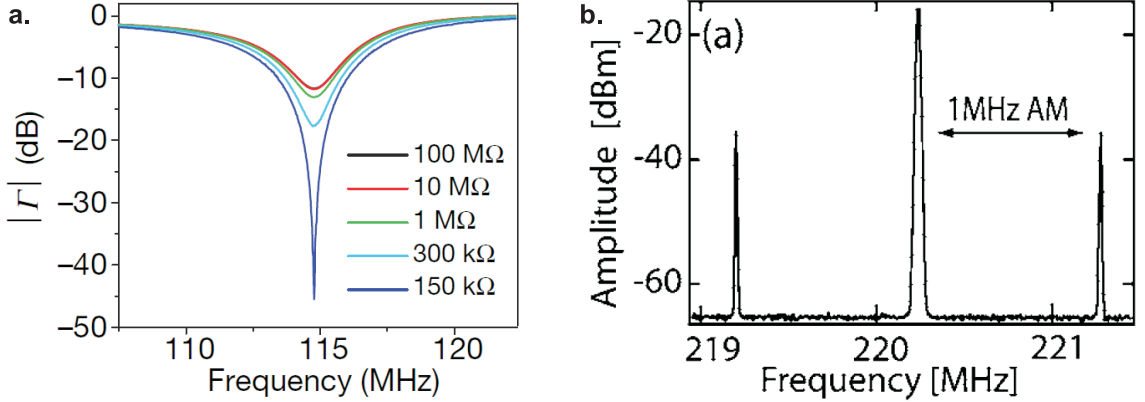


Figure 4.9: a) Measurement of the voltage reflection coefficient  $|\Gamma|$  as a function of frequency for different values of resistance. The matching resistance is in this particular case  $150 \text{ k}\Omega$ . Adapted from [80]. b) A gate modulation of 1 MHz on the QPC gate is used to test the response. The measurement shows the response of the RF-QPC before demodulation. The carrier frequency is set to 220.2 MHz (central peak). Adapted from [76].

When taking an actual measurement the carrier frequency is set to resonance  $\frac{\omega_0}{2\pi}$ .

Changes in the quantum dot charge state are reflected in the QPC resistance: Fig. 4.9a shows a measurement of the voltage reflection coefficient for different resistance values. In this specific example,  $R_0$  was  $150 \text{ k}\Omega$ .

### Choice of components and measurement of the resonance frequency

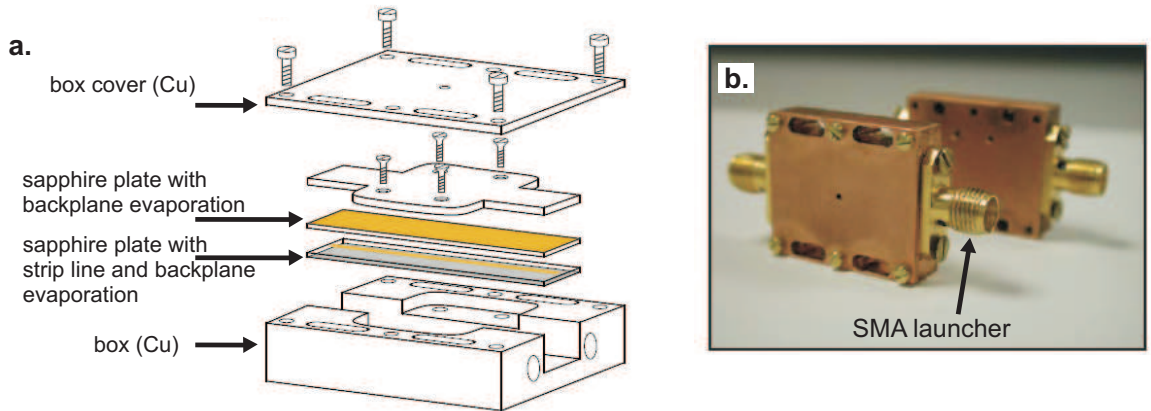
Experimentally the resistance of the sample at the operation point is known: the QPC is tuned to the steepest point on the first conduction step (with our choice, about  $50 \text{ k}\Omega$ ). The parasitic capacitances can be estimated and the chip inductor is chosen such that the resonance frequency lies within the bandwidth of the circulator and amplifier (further explained in the next section).

A newly assembled PC-board with the tank circuit is usually first tested at room tem-

perature or 4 K without sample by measuring the reflected power  $|\Gamma(\omega)|^2$  as a function of frequency. The resonance frequency without the sample is typically higher than the resonance frequency with the sample (in our case by approximately 60 MHz). After bonding the sample, the whole circuit is cooled to 4 K in order to measure  $|\Gamma(\omega)|^2$  and determine whether the resonance frequency lies in the correct frequency window.

### Output signal

At the directional coupler the reflected signal is mainly transmitted towards output1. Between the mixing chamber and the 4 K stage the coaxial line is superconducting (niobium outer and inner conductor). Thermal anchoring of the inner conductor can not be provided by attenuators, since this would attenuate the signal we want to measure. We thus thermalise the inner conductor via a  $50 \Omega$  sapphire stripline [71].



- Copper box: design by Leo DiCarlo, production by the Harvard machine shop
- Sapphire plate: A-plane orientation +/- 5°, commercial polish on both sides, C-axis along length, 25.4 mm x 6.35 mm x 0.508 mm (from Boston Piezo-Optics, Inc.)
- Launcher: Midwest Microwave SMA-5261-15-DRP-02

Figure 4.10: a) Drawing of the sapphire stripline box, with the two plates of sapphire and the stripline in the middle. The stripline is designed to have a  $50 \Omega$  impedance. b) Picture of the closed copper box, which is mounted inside the dilution refrigerator and thermally anchored to the cold plate. Adapted from [71].

A chromium/gold (10 nm/200 nm) stripline,  $200 \mu\text{m}$  wide [70], designed to have  $50 \Omega$

impedance, is thermally evaporated on a sapphire plate. The stripline is then covered with another sapphire plate (see Fig. 4.10). The inner conductor of the coaxial lines is connected on both sides to the stripline via SMA launchers (shown in Fig. 4.10). Sapphire ( $\text{Al}_2\text{O}_3$ ) is chosen as the dielectric because it is an insulator with very good thermal conductance ( $2 \cdot 10^{-5} \frac{\text{W}}{\text{cm}\cdot\text{K}}$  at 100 mK) [72]. The thermal connection is optimized by evaporating chromium/gold (10 nm/200 nm) on the backplane of each of the sapphire plates and by tightly clamping them between copper plates. More details about the planning of the copper box can be found in [71].

The circulator and the amplifier are mounted at the 4 K stage. The circulator is a non-reciprocal 3-port network (ideally lossless and matched at all ports) [70]. This means that the signal arriving at port 1 is only transmitted to port 2 and the signal arriving at port 2 is only transmitted to port 3 (port 1, 2 and 3 are indicate in Fig. 4.6). There are two reasons to interpose a circulator. First, if placed before the amplifier, it prevents reflection of signal from the slightly mismatched input of the amplifier creating resonances. Second, the circulator prevents amplifier noise from propagating back towards the sample.

At room temperature, the signal is amplified with a second amplifier. The signal is then sent through a phase shifter and a mixer before being detected by an oscilloscope. The phase shifter is necessary to easily adjust the phase of the outcoming signal such that it is in phase with the reference signal (i.e. the input signal). The mixer is used for demodulation of the reflected signal with the input signal. The demodulated signal is then measured with an oscilloscope or a DAQ board. Fig. 4.9 shows a measurement of the QPC response before demodulation when a periodic modulation of 1 MHz is applied to the QPC gate.

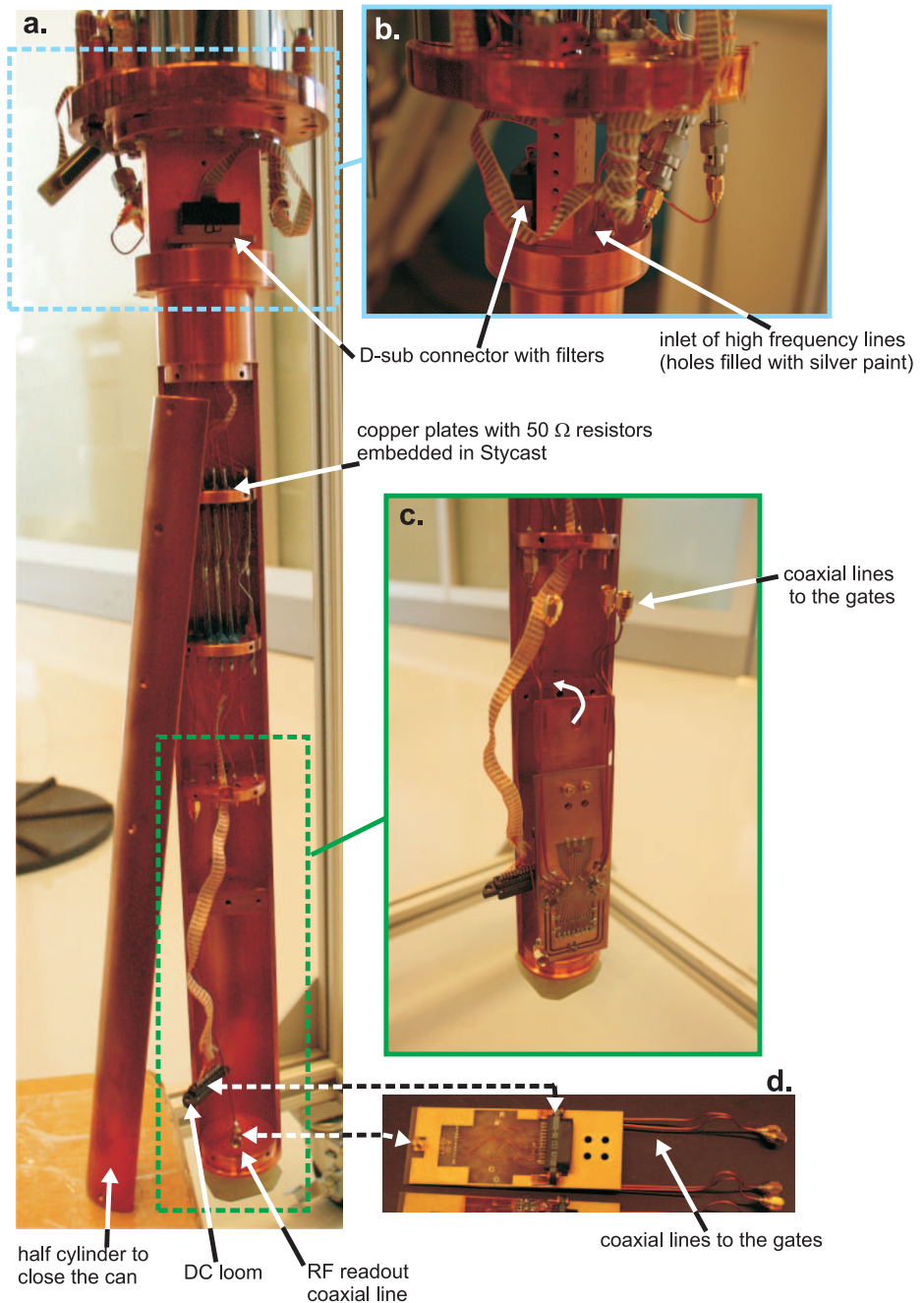


Figure 4.11: MX-50 cold finger. a) The cold finger: the copper cylinder can be opened to access and change the sample holder and the sample. b) Upper part of the cold finger showing the DC-lines connected to a D-sub connector with filters, and the inlet of the high frequency lines into the can. c) Lower part of the cold finger with the indication of how the PC-board is mounted. d) PC-board back side with the connection to the RF read-out coaxial line, to the DC lines and to the gate coaxial lines.

#### 4.2.4 The cold finger

For the design of the second cold finger, we also planned a shield that would prevent radiation warmer than  $T_{\text{mixing chamber}}$  from reaching the sample [33]. As shown in Fig. 4.11, the cold finger is a copper cylinder that can be opened from the side. The DC lines entering form the top part through a D-sub connector that includes capacitive filters, are connected to two  $50 \Omega$  resistors embedded with Stycast in two copper disks. This solution is in principle similar to the one chosen for the previous set-up. In the first case, the distributed RC filter is formed by the manganin ( $\sim 10 \Omega$ ) wire and the silver paint (the ground being the cold finger). In the second case, the resistance is given by two  $50 \Omega$  resistors in series with the copper wires. On the PC-board (the chip holder) a  $100 \text{ pF}$  capacitance to ground is mounted in series with the DC lines before they reach the bonding pads.

The AC lines are fixed in the top part of the cold finger with silver paint and go then straight to the PC-board, where the inner conductors are soldered to bonding pads and the outer conductor to the RF ground.

Once the whole system was assembled, we determined the electron temperature by fitting the width of Coulomb blockade peaks measured in a quantum dot and obtained a temperature of about  $100 \text{ mK}$ .

### 4.3 Data acquisition programs

The acquisition of the data presented in Chap. 8 was done with a program developed by Shahal Ilani and written in Labview. The framework was in use by all members of the group at the Weizmann Institute. For this specific project, a few routines had to be added to control the Tektronix AWG520 arbitrary waveform generator.

The acquisition of data presented in Chap. 5, 6 and 7 was done with a MATLAB-based measurement program, developed by Hendrik Bluhm to which Vivek Venkatachalam added a graphic interface. This program was introduced to widen the variety of scans and the data acquisition speed. Being command line based, MATLAB allows fast prototyping that can be convenient when the development of the program is still in an exploratory phase.

## Chapter 5

# Universal quantum control of two-electron spin quantum bits using dynamic nuclear polarization

Sandra Foletti<sup>1†</sup>, Hendrik Bluhm<sup>1†</sup>, Diana Mahalu<sup>2</sup>, Vladimir Umansky<sup>2</sup> and Amir Yacoby<sup>1</sup>

1. Department of Physics, Harvard University, Cambridge, MA 02138, USA  
2. Braun Center for Submicron Research, Department of Condensed Matter Physics,  
Weizmann Institute of Science, Rehovot 76100, Israel

† These authors contributed equally to this work.

One fundamental requirement for quantum computation is to perform universal manipulations of quantum bits at rates much faster than the qubit's rate of decoherence. Recently, fast gate operations have been demonstrated in logical spin qubits composed of two electron spins where the rapid exchange of the two electrons permits electrically controllable rotations around one axis of the qubit. However, universal control of the qubit requires arbitrary

rotations around at least two axes. Here we show that by subjecting each electron spin to a magnetic field of different magnitude we achieve full quantum control of the two-electron logical spin qubit with nanosecond operation times. Using a single device, a magnetic field gradient of several hundred milliTesla is generated and sustained using dynamic nuclear polarization of the underlying Ga and As nuclei. Universal control of the two-electron qubit is then demonstrated using quantum state tomography. The presented technique provides the basis for single and potentially multiple qubit operations with gate times that approach the threshold required for quantum error correction<sup>1</sup>.

## 5.1 Introduction

The potential realization of quantum computers has attracted a lot of attention because of their promise to perform certain calculations practically intractable for classical computers. While a classical bit attains only two values (0 and 1), the phase space of a quantum bit (a two-level system) is in one-to-one correspondence with the points on the surface of a three dimensional sphere, the Bloch sphere [16] (introduced in Chap. 2), where the basis states are represented at the north and south pole (Fig. 5.1a). A generic manipulation of the qubit needed to implement universal gate operations requires the ability to perform rotations around two axes in the Bloch sphere [39, 82, 83, 51] (for example the  $z$  and  $x$ -axis). In the present work, the two-level quantum bit (smallest logical unit of the quantum computer) is encoded in the spin state of two electrons confined in a double-well potential. This semiconductor-based system has potential for good scalability, manipulations are all-electrical and they are potentially fast enough to enable  $10^4$  universal gate operations within

---

<sup>1</sup>This chapter is adapted from Ref. [81].

the coherence time. This is an essential requirement for quantum error correction [84].

For the two-electron spin qubits, rotations around the  $z$ -axis, corresponding to the coherent exchange of two electrons, have recently been demonstrated by Petta *et al.* [13]. Rotations around the second axis require the presence of a non-uniform magnetic field across the double-well potential, making the two spins precess at different rates. Here we take advantage of the interaction of the electrons with the nuclear magnetic field of the Ga and As sublattices of the host material in order to generate the required magnetic field gradient. While fluctuations of this hyperfine field are known to be a major source of decoherence [59, 85, 86, 34, 87], the results presented in this chapter demonstrate the possibility of building up a gradient in the hyperfine field that significantly exceeds the fluctuations and can be sustained for times longer than 30 min. This is done by employing pumping schemes that transfer spin and thus magnetic moment from the electronic system to the nuclei. Internally created gradients of nuclear field, in excess of 200 mT, together with the coherent exchange of the two electrons allow us to rapidly manipulate the two-electron spin qubit. The coherent manipulation is demonstrated by reconstructing the evolution of the state within the Bloch sphere through quantum state tomography.

## 5.2 Description of the system

The double-well potential that confines the electrons is formed by applying a negative voltage to metal gates deposited on top of a two dimensional electron gas embedded in a GaAs/AlGaAs heterostructure. The negative voltages deplete the electrons underneath the metal gates creating two isolated puddles of electrons (a double quantum dot, Fig. 5.1b). The number of electrons in the dots can be controlled by tuning the voltages on the gates. We restrict the total occupation of the double quantum dot to two electrons, and describe

their spatial separation by the parameter  $\varepsilon$ : for  $\varepsilon \gg 0$  both electrons are in the right quantum dot, the (0,2) configuration; for  $\varepsilon \ll 0$  one electron occupies each dot, the (1,1) configuration. The parameter  $\varepsilon$  and hence the dots' charge state can be continuously swept through intermediate configurations by varying the voltages on the metal gates.

In the (0,2) charge configuration, the only energetically accessible spin configuration is the singlet state  $S(0,2) = (\uparrow\downarrow - \downarrow\uparrow)/\sqrt{2}$  (the arrows indicate the direction of the electron spins). As we separate the electrons, the wavefunctions overlap decreases and four spin configurations become energetically degenerate: the singlet  $S(1,1)$  and three triplets  $T_0 = (\uparrow\downarrow + \downarrow\uparrow)/\sqrt{2}$ ,  $T_- = \downarrow\downarrow$  and  $T_+ = \uparrow\uparrow$  (Fig. 5.1d). We select the states  $S(1,1)$  and  $T_0$ , both having zero  $z$  component of the spin angular momentum, as the basis states of our logical qubit [40, 41] and lift the degeneracy with the states  $T_-$  and  $T_+$  by applying an external magnetic field  $B_{ext}$ . The Zeeman energy  $E_z = g^* \mu_B B$  ( $g^* = -0.44$  is the  $g$ -factor for electrons in GaAs,  $\mu_B$  Bohr's magneton) shifts the  $T_+$  state to lower energies, creating a crossing point with the singlet (marked by a red circle in Fig. 5.1d) at a value of  $\varepsilon$  that depends on  $\mathbf{B}_{tot} = \mathbf{B}_{ext} + \mathbf{B}_{nuc}$ , where  $\mathbf{B}_{nuc} \equiv (\mathbf{B}_{nuc,L} + \mathbf{B}_{nuc,R})/2$  is the average hyperfine field and  $\mathbf{B}_{nuc,L}$  and  $\mathbf{B}_{nuc,R}$  the nuclear fields felt by the electrons in the left and right dot, respectively (Fig. 5.1c). Within this logical subspace, rotations around the  $z$ -axis are controlled by the energy splitting between  $S(1,1)$  and  $T_0$ , denoted by  $J(\varepsilon)$ . This evolution amounts to a coherent exchange of the two electrons. Rotations around the  $x$ -axis are controlled by the  $z$ -component of a magnetic field gradient across the two electrons,  $\Delta\mathbf{B}_{nuc} = \mathbf{B}_{nuc,L} - \mathbf{B}_{nuc,R}$ . If we thus let a state evolve around a combined axis  $J\mathbf{z} + g\mu_B \Delta B_{nuc}^z \mathbf{x}$ , the precession frequency will be given by  $f = \sqrt{J^2 + (g\mu_B \Delta B_{nuc}^z)^2}/h$  (where  $h \approx 4 \cdot 10^{-15} \text{ eV} \cdot \text{s}$  is Plank's constant).

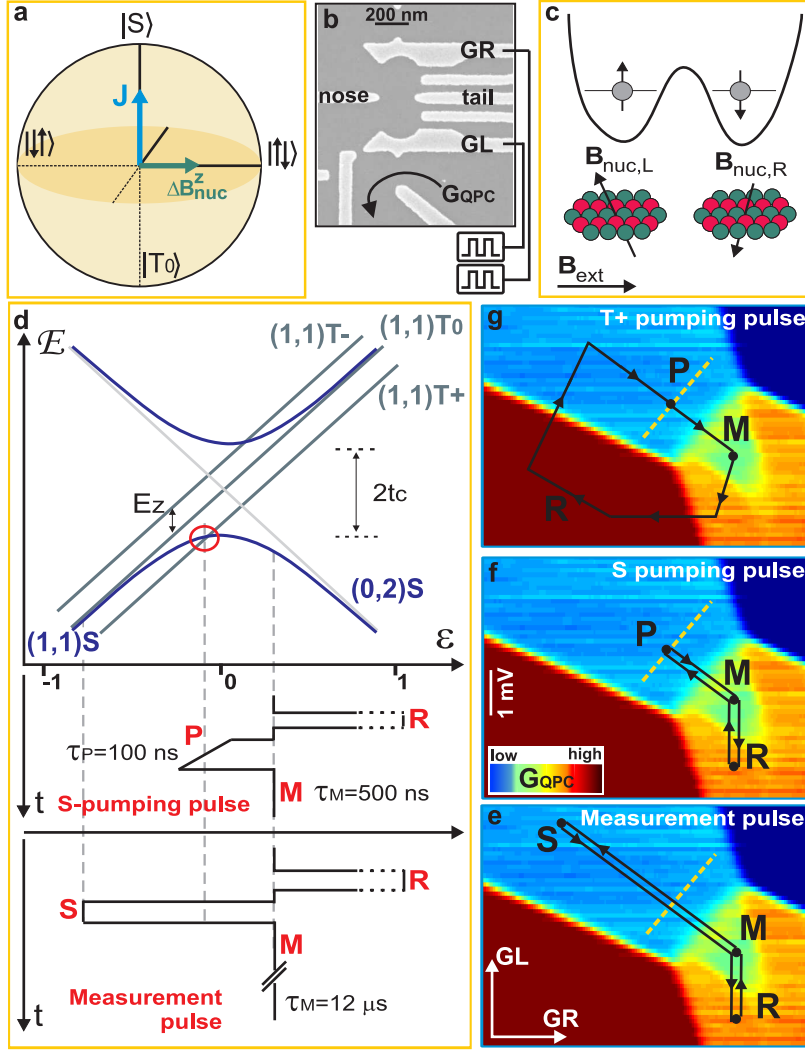


Figure 5.1: a) Geometrical representation (Bloch sphere) of the two level system ( $S$  and  $T_0$ ) and the two rotation axes ( $J$  and  $\Delta B_{nuc}^z$ ) allowing the implementation of universal single qubit gates. b) SEM micrograph of a device similar to the one measured. Gates GL and GR control the charge configuration of the two dots, the central gates (Nose and Tail) control the tunneling rate between the two dots. The average charge configuration is detected by measuring the conductance ( $G_{QPC}$ ) through a capacitively coupled quantum point contact. c)  $\mathbf{B}_{nuc,L}$  and  $\mathbf{B}_{nuc,R}$  are the local magnetic fields experienced by the electrons in the left and right dot through hyperfine coupling with the Ga and As nuclei. d) Schematic representation of the energy levels at the  $(0,2)$ – $(1,1)$  charge transition for finite external magnetic field. The detuning  $\varepsilon$  from the degeneracy point is controlled by the voltages on GL and GR. Two pulse cycle are presented: 1) Nuclear pumping: the system is moved to point P where  $S$  and  $T_+$  are degenerate and can mix. 2) Measurement pulse: the system is moved to large negative detuning where the states  $S$  and  $T_0$  can mix. e) The measurement pulse scheme, f) the  $S$ -pumping pulse scheme, g) the  $T_+$ -pumping pulse scheme, all shown as a function of GL and GR.

## 5.3 Pumping schemes

While controlled  $z$ -rotations have been previously shown [13], controlled rotations around the  $x$ -axis of the two-electron logical qubit have not been demonstrated to date. Clearly, the challenge is to provide a stable magnetic field gradient across the two dots which exceeds the intrinsic nuclear fluctuations due to the hyperfine interaction. Here we present two polarization schemes by which the gradient can be increased to values significantly exceeding its fluctuations. Both pumping schemes make use of the degeneracy point between  $S(1,1)$  and  $T_+$ . Transitions between the two states that are driven by the transverse component of  $\Delta\mathbf{B}_{\text{nuc}}$  [46] are accompanied by a spin flip of the nuclei in order to conserve the total angular momentum.

### 5.3.1 $S$ -pumping scheme

Our first pumping scheme follows a standard recipe [49, 88] of initializing the system in the  $S(0,2)$  state followed by a 0.5 mV ramp across the  $S-T_+$  transition in 50 ns (100 ns) with 4 MHz (1.1 MHz) repetition rate. Changes in gate voltage can be converted to energy shifts with a conversion factor  $\approx 0.1$  eV/V extracted from transport measurements through the double dot at finite bias. This process ideally transfers one unit of angular momentum into the nuclear sub system.

### 5.3.2 $T_+$ -pumping scheme

In addition to the  $S$ -pumping scheme, we have developed an alternative pumping scheme whereby we initialize the system in a  $T_+(1,1)$  state followed by a similar slow passage through the  $S-T_+$  degeneracy point. This new  $T_+$ -pumping scheme allows us to polarize the nuclear subsystem in a direction opposite to the  $S$ -pumping scheme. The  $T_+$ -pumping scheme

works only when the Zeeman energy exceeds the electron temperature in the reservoirs: the system is swept slowly into (0,1) and subsequently reloaded into the (1,1) charge state (Fig. 5.1g). First the right and then the left electron align with the external magnetic field due to large Zeeman energy ( $\approx 12.5 \mu eV$  at 500 mT), which preferentially loads a  $T_+$  state.

## 5.4 Measurement scheme

While the above nuclear pumping schemes should produce nuclear polarization, it is not obvious at all that this nuclear polarization should be different across the two dots [88]. Since the mixing between the  $S(1,1)$  and  $T_0(1,1)$  is only sensitive to the field gradient, we use a pulse cycle that monitors the coherent evolution around the  $x$ -axis in order to measure this gradient. The system is first reset into a  $S(0,2)$  state at point **M**.  $\varepsilon$  is then abruptly set to point **S** in (1,1) by changing the voltages on both GR and GL by 7 mV for an evolution time  $\tau_S$  (see Fig. 5.1e). Here  $\Delta B_{nuc}^z \gg J(\varepsilon)/g\mu_B$  drives coherent oscillations between  $S(1,1)$  and  $T_0$  and the probability of being in a singlet state oscillates as a function of evolution time  $\tau_S$  as  $p(S) = \cos^2(g^*\mu_B\Delta B_{nuc}^z \cdot \tau_S/2\hbar)$ . After a time  $\tau_s$  the system is brought back to the measurement point **M** for the rest of the total pulse time of 12  $\mu s$ . Only transitions from  $S(1,1)$  to  $S(0,2)$  are allowed, while  $T_0$  remains blocked in the (1,1) charge configuration. This spin-blockade effect allows to map the spin configuration of the state onto a charge configuration [33], which is measured by a charge sensor.

Here we use a quantum point contact (QPC) positioned next to the double quantum dot (Fig. 5.1b) in order to detect changes in the double dot charge configuration. The QPC signal, averaged over many gradient-probing cycles, is proportional to the probability of being in a singlet state. The QPC was operated at a 2 nA rms AC bias current and a conductance of approximately 0.4  $G_0$ , where  $G_0 = 2e^2/h$  is the conductance quantum. The

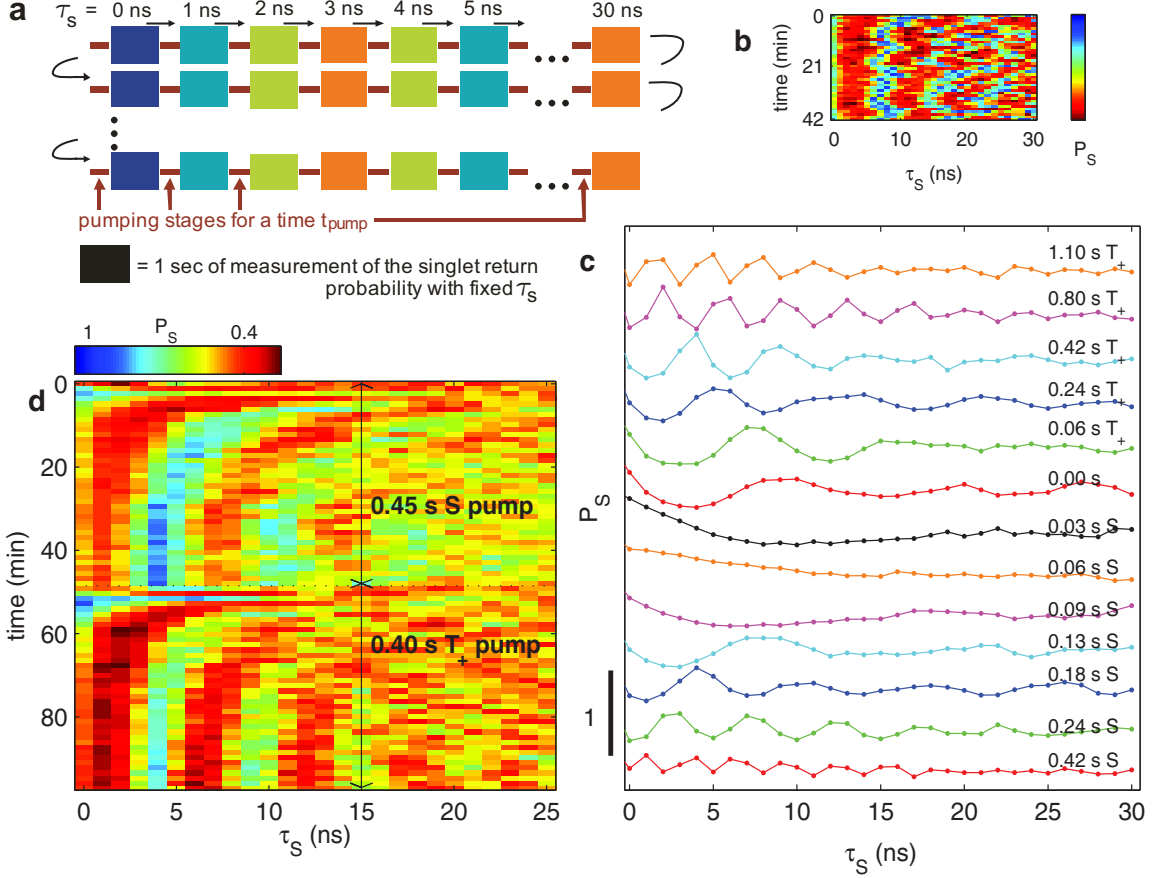


Figure 5.2: a) Schematics explaining the measurement of the singlet return probability as a function of  $\tau_S$ . Each measurement point (rectangle) is an average over 1 sec and preceded by a pump cycle that runs for a time  $t_{pump}$ . Each line is a repetition of the same measurement procedure. b) Measurement of the singlet return probability as a function of  $\tau_S$  for  $t_{pump} = 60$  ms. c) Singlet return probability as a function of separation time  $\tau_S$  for different  $t_{pump}$ . Each data set line is an average over 30  $\tau_S$  sweeps.  $P_s$  is normalized by the size of the DC charge transition (see Supplementary Material). Traces are displaced for clarity. d) Crossover between  $S$  and  $T_+$ -pumping. The plot shows an average of nine subsequent repetitions of the same measurement. The disappearance of the oscillations upon changing the pump pulse followed by a recovery (around 0 and 50 min) suggests that  $S$  and  $T_+$ -pumping produce  $\Delta B_{nuc}^z$  of opposite sign.  $B_{ext} = 1.5$  T for these data sets.

signal change across the (1,1)-(0,2) charge transition was typically 2 to 4  $\mu$ V (corresponding to a conductance change of 2-4 %). We note that since the ground state is a singlet ( $S$ ), the signal corresponding to a singlet ( $p(S) = 1$ ) is well known, whereas that corresponding to a triplet ( $p(S) = 0$ ) is affected by the inelastic triplet decay rate during the measurement stage [33]. This decay rate varies with dot tuning,  $B_{ext}$  and apparently polarization, and is

different for  $T_0$  and  $T_+$ . Because of these uncertainties in the signal conversion, we normalize the QPC signal by the size of the DC charge transition and denote the result by  $P_S$ .

## 5.5 Steady state nuclear magnetic field gradients

### 5.5.1 Gradient build-up with and $S$ and $T_+$ pumping

A steady state nuclear field can be achieved by continuously alternating between a pump cycle that runs for a time  $t_{pump}$ , and a gradient probing cycle that runs for 1 sec, as schematically visualized in Fig. 5.2a. In each measurement stage a gradient probing pulse with a different separation time  $\tau_S$  is used. For each sweep,  $\tau_S$  is varied between 0 and 30 ns in steps of 1 ns. The outcome of a measurement repeating  $\tau_S$ -sweeps 40 times and using  $t_{pump} = 60$  ms is shown in Fig. 5.2b. An oscillatory signal with a frequency fluctuating around a steady mean is clearly visible. In the present measurement the gradient is kept in a steady state for 40 minutes, but this time could have been extended indefinitely. Each curve in Fig. 5.2c shows an average over 30  $\tau_S$  sweeps. The different values of  $t_{pump}$  control the steady state value of the gradient in each data set. We observe that the oscillations vanish (corresponding to a  $\Delta B_{nuc}^z$  fluctuating around 0) at moderate  $S$ -pumping rather than  $t_{pump} = 0$ . This appears to reflect a small polarization effect from the measurement pulses that can be compensated with  $S$ -pumping.

Under certain tuning conditions (i.e. specific coupling strengths to the reservoir and between the dots) and certain ranges of magnetic field values, we observe oscillations ( $S-T_0$  mixing) even without pumping. They appear to be induced by the measurement cycle. Applying  $T_+$ -pumping monotonically increases their frequency, whereas the  $S$ -pumping cycle first reduces it until the oscillations disappear. For  $S$ -pumping with even larger  $t_{pump}$ ,

oscillations with increasing frequency reappear. This “spontaneous”  $\Delta B_{nuc}^z$  vanishes gradually below  $B_{ext} \approx 0.2$  T and typically reaches its maximal value around 0.5 T. At larger fields, it usually decreases but remains substantial up to 1.5 T. Furthermore, it tends to increase when using pulses with overshoots or near the tip of the readout triangle. Various observations suggest that the origin of this polarization is an inelastic decay of triplets at the measurement point, but understanding the details of the unintentional polarization will require further experiments that go beyond the scope of the present work. Since we have demonstrated that intentional pumping can increase or compensate and overcome the measurement induced  $\Delta B_{nuc}^z$ , it is clear that its presence does not impede the use of dynamic nuclear polarization to achieve quantum control for double quantum dot spin qubits. It is not clear to what extent the polarization effects of the measurement and pump pulses are related; however the fact that  $S$ -pumping can cancel or overcome the effect of the measurement pulses suggests that the two mechanisms are simply additive.

To compare the  $S$  and  $T_+$ -pumping schemes, we have taken a measurement where we have switched between  $S$ -pumping and  $T_+$ -pumping every  $40 \tau_s$  sweeps (see Fig. 5.2c). The data show that upon changing the pump cycle, the oscillations disappear and then recover after a few minutes in a way that suggests a sign change of the induced gradient.

### 5.5.2 Loss of contrast

The data shown in Fig. 5.2 was taken with the measurement point **M** chosen near the tip of the readout triangle, the region in gate space where spin-blockade can be used for spin to charge conversion. We find that when point **M** is further away from the tip, the amplitude of the observed oscillations decreases with increasing pump time (i.e. oscillation frequency) as shown in Fig. 5.3. For sufficiently large  $\Delta B_{nuc}^z$ , the oscillations can become

entirely invisible.

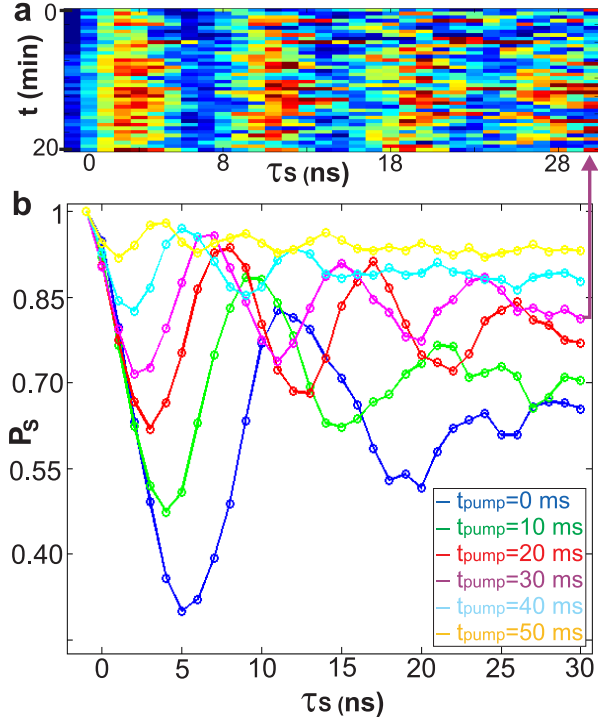


Figure 5.3: a) Singlet return probability as a function of separation time  $\tau_S$  ( $0 \leq \tau_S \leq 30$  ns) for  $t_{pump}=60$  ms. b) Singlet return probability as a function of  $\tau_S$  for different pumping times. The contrast of the signal decreases with increasing pumping time.

A possible explanation to that could be as follows: if at the measurement point  $J < \Delta B_{nuc}^z$ ,  $\Delta B_{nuc}^z$  can drive mixing between  $T_0(1,1)$  and  $S(1,1)$ . In addition to that, the inelastic relaxation rate between  $S(1,1)$  and  $S(0,2)$  can be position dependent. For values of  $\varepsilon$  where this relaxation rate is larger than  $1/t_M$  ( $t_M$  the total measurement time), the triplet  $T_0$  can decay within this measurement time and spin blockade is lifted. On the other hand if  $J \gg \Delta B_{nuc}^z$ , mixing does not occur and  $T_0$  remains blocked in the (1,1) charge configuration.

By adding an overshoot along the  $\varepsilon$  axis (typically by 1.4 mV for 50 ns) when returning from point **S** to point **M**, the contrast can be kept finite even at large  $\Delta B_{nuc}^z$ . This technique was employed to take the data shown in Fig. 5.5b. Changes in the pulse distortions due to

the setup's finite bandwidth for separation times  $\tau_S$  on the order of 100 ns or longer also appear to recover the readout contrast.

Presumably, the pulse shape changes in such a way that regions where a large  $\Delta B_{nuc}^z$  significantly enhances relaxation are avoided during the readout stage of the pulse. Improvements in the high frequency setup should allow us to understand and/or eliminate these effects. While the above explanations for the contrast loss and recovery are qualitatively consistent with all our data, more work is required to establish their correctness beyond reasonable doubt. However, we are confident that this puzzle does not affect the interpretation of our data in terms of ability to control and utilize  $\Delta B_{nuc}^z$  for universal qubit rotations.

## 5.6 Measurement of the average local magnetic field

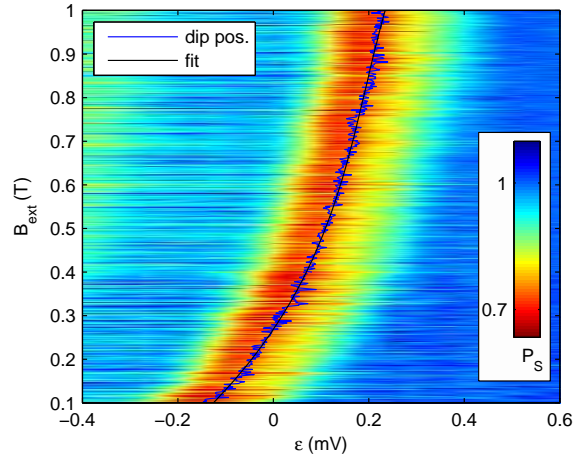


Figure 5.4: Line scans across the  $S-T_+$  transition vs.  $B_{ext}$  used to calibrate the shift of the transition in response to pumping. The  $\varepsilon$  axis is given in units of gate voltage and contains an arbitrary offset. The blue line shows the fitted center of the dip in  $P_S$  for each scan line and the black line is a polynomial fit to those positions as a function of  $B_{ext}$ .

While the magnitude of the gradient is determined via coherent  $x$ -rotations, we can

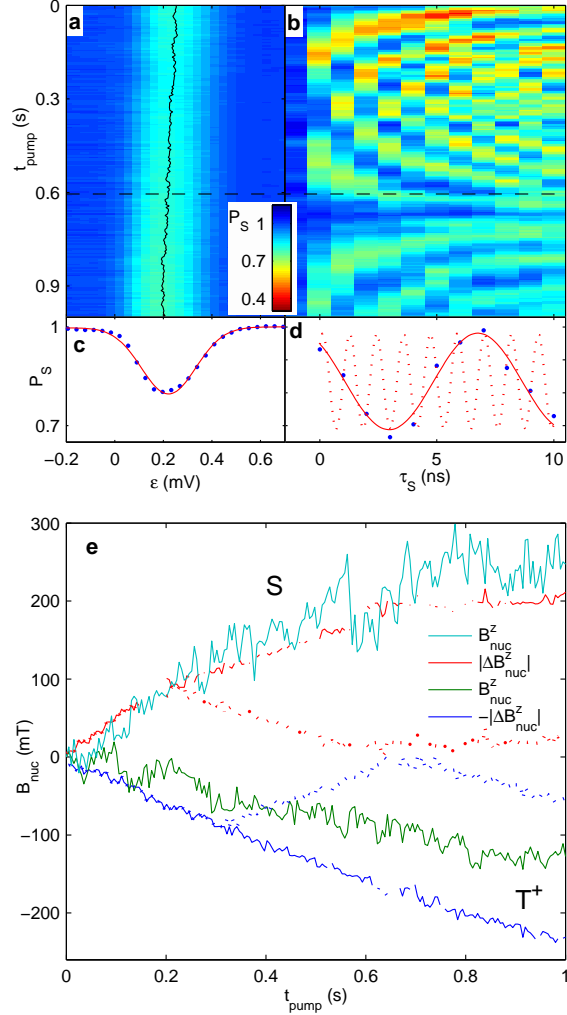


Figure 5.5: a) Line scans of the position of the  $S-T_+$  transition as a function of pump time: the  $T_+$ -pumping cycle, applied for a duration  $t_{\text{pump}}$ , precedes each 2 s long measurement interval. b) Singlet return probability versus  $\tau_S$  under the same pumping conditions as in a). The repeated increase and decrease of the apparent oscillation frequency is a consequence of aliasing of a monotonically increasing frequency due to the 1 ns sampling interval. c) Single line scan from the data in panel a) at  $t_{\text{pump}} = 0.6$  s. d) The corresponding  $\tau_S$  sweep from panel b). The continuous red line is a sinusoidal fit, the dashed line reconstructs the actual, non-aliased time dependence of the singlet probability. e)  $B_{\text{nuc}}$  and  $\Delta B_{\text{nuc}}^z$  extracted from fits as shown in c) and d) as a function of  $t_{\text{pump}}$  for both  $T_+$  and  $S$ -pumping. The shift of the  $S-T_+$  transition was converted to  $B_{\text{nuc}}^z$  using its measured dependence on  $B_{\text{ext}}$  (see Fig. 5.4) [49],  $\Delta B_{\text{nuc}}^z$  was obtained from the fitted oscillation frequency corrected for aliasing. The dotted lines show the same data before this correction. The fluctuations in the  $B_{\text{nuc}}^z$  curves reflect measurement noise.  $B_{\text{ext}} = 500$  mT for these data sets.

also measure the average value of the nuclear field by monitoring the position of the  $S$ - $T_+$  transition [49]. This should clarify whether spins are flipped only in one or both dots. Figs. 5.5a,b show interleaved measurements of the position of the  $S$ - $T_+$  transition [88] and the oscillatory  $S$ - $T_0$  mixing as a function of  $t_{pump}$  using the  $T_+$ -pumping cycle. A shift of the  $S$ - $T_+$  transition to more negative  $\varepsilon$  corresponds to the build-up of an average field  $B_{nuc}^z$  oriented opposite to the external magnetic field, consistent with spin flips from down to up in the nuclear system [45].

To probe the position of the  $S$ - $T_+$  transition, we have used a pulse as reported in Refs. [88, 13]. It is similar to the  $S$ -pumping cycle, with the ramping through the  $S$ - $T_+$  transition replaced by a jump to and a wait time at the degeneracy point (typically 100 ns). In addition, it is extended with a measurement stage at point **M**, resulting in a total pulse period of 12  $\mu$ s. Sweeping the DC value of GL and GR while running this pulse results in line scans as shown in Fig. 5.5c. When the  $S$  and  $T_+$  states are degenerate, transitions from the prepared  $S$  to the  $T_+$  state are allowed and cause a dip in  $P_S$ . For the data in Fig. 5.5, this measurement has been interleaved with the gradient-probing pulse at a fixed point, each running for 2 s with pumping in between. Thus, any polarization effect of either pulse will affect both measurements equally because the nuclear relaxation time is much longer than 2 s. To calibrate the shift in the  $S$ - $T_+$  transition, we have taken line scans along  $\varepsilon$  as a function of external field  $B_{ext}$  (see Fig. 5.4) and analyzed them in the same way as the measurement in Fig. 5.5a. We have fitted the field dependence of the position of the dip in  $P_S$  with a polynomial. This allows to convert the shift in the  $S$ - $T_+$  transition in response to polarization to a change in field, which can be identified with  $B_{nuc}^z$  if  $\Delta B_{nuc}^z \ll B_{ext}$ .

Fig. 5.5e shows that at  $B_{ext} = 500$  mT,  $\Delta B_{nuc}^z$  reaches 230 mT while  $B_{nuc}^z$  is about 130 mT. The ratio of nearly a factor 2 indicates that the nuclei are polarized predominantly

in one of the two dots. Data obtained using the  $S$ -pumping cycle (Fig. 5.5e) show a  $\Delta B_{nuc}^z$  that tends to be slightly smaller than the average field. The value of  $B_{nuc}^z$  can be subject to various systematic analysis errors, but it is clearly not much larger than  $\Delta B_{nuc}^z$  as previously mentioned.

The analysis may be subject to various systematic errors. An imperfect alignment of the sample with the external magnetic field may lead to orbital effects contributing to the calibration of the position of the  $S-T_+$  transition via its dependence on  $B_{ext}$ . This calibration may also be affected by a small measurement-induced polarization, either in the calibration data or at the beginning of each measurement. Finally, the  $S-T_+$  transition might also shift in response to  $\Delta B_{nuc}^z$  rather than just  $B_{ext} + B_{nuc}^z$ , although we estimate this effect to be negligible at least for values of  $\Delta B_{nuc}^z < J(\varepsilon)$ .

### 5.6.1 Tuning

Reilly *et al.* [89] reported a saturation of the mean hyperfine field  $B_{nuc}^z$  under  $S$ -pumping at  $B_{ext} + B_{nuc}^z \approx 20$  mT, whereas we find that a shift of the  $S-T_+$  transition corresponding to more than 100 mT can be induced at fields as large as 0.7 T.

This discrepancy is at least partly due to the different tuning (i.e. different coupling strength to the reservoir and between the dots) used in the two experiments. Especially the tunnel coupling between the two dots seems to have a considerable influence. As a guide for establishing suitable tuning conditions, we typically measure the current through the double dot as a function of GL and GR for a bias voltage of 0.4 mV across the dot in the non-Pauli blocking direction. Data that is representative for the tuning typically used in the present work is shown in Fig. 5.6a. In Ref. [88], the transport current was typically an order of magnitude smaller [90], similar to our data shown in Fig. 5.6b. A fading signal of

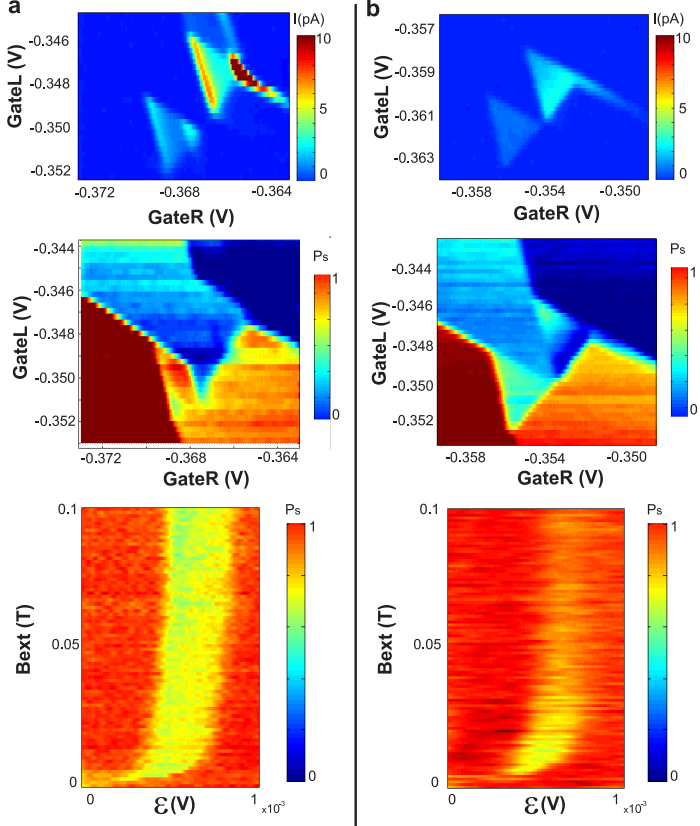


Figure 5.6: a) Current through the dot (upper panel), QPC signal (middle panel) and position of the  $S-T_+$  transition as a function of magnetic field (lower panel).  $\varepsilon$  is given in units of gate voltage with an arbitrary offset). b) The same kind of data for tuning conditions more similar to those used in Ref. [88].

the  $S-T_+$  mixing when increasing the external magnetic field indicates that the transition rate as well as the pumping efficiency are decreasing. For dot tuning shown in Fig. 5.6a, the contrast stays constant at least up to 1.5 T.

## 5.7 State tomography

Combining our slowly tunable  $x$ -rotation gate with the electrically controllable exchange gate allows single qubit rotations around an axis that can be rapidly tilted to any desired angle between 0 and nearly  $\pi/2$  away from the  $x$ -axes (angle  $\theta$  in Fig. 5.7d). Concaten-

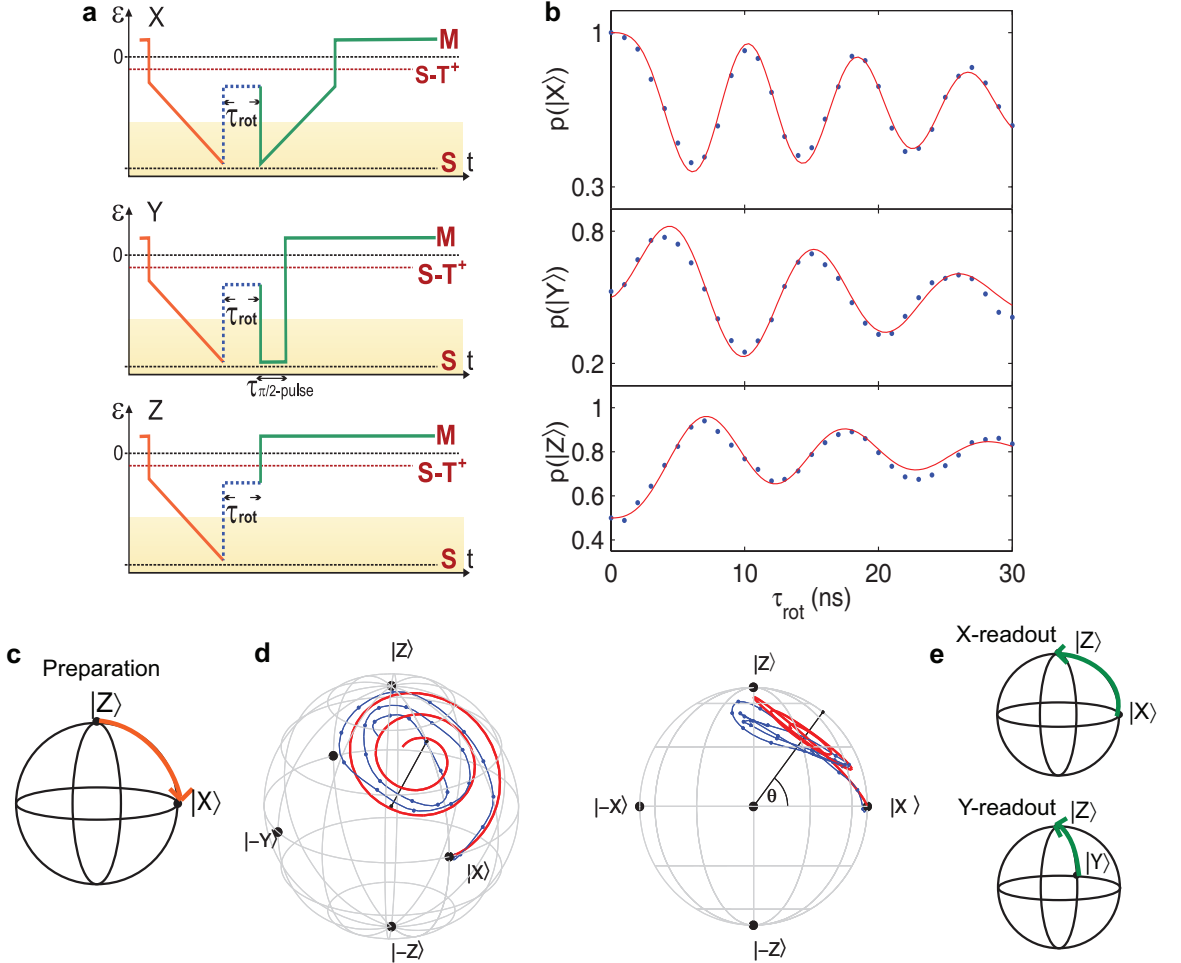


Figure 5.7: a) Pulse schemes to measure the singlet probability  $p(|S\rangle) \equiv p(|Z\rangle)$ , the  $|\uparrow\downarrow\rangle$  probability  $p(|\uparrow\downarrow\rangle) \equiv p(|X\rangle)$  and the  $|S\rangle + i|T_0\rangle$  probability  $p(|S\rangle + i|T_0\rangle) \equiv p(|Y\rangle)$  after rotation around a tilted, tunable axis. b) Measurements taken with the X, Y and Z pulses (dots) and fits (line) to a numerical solution of the Schrödinger equation of the  $S-T_0$  Hamiltonian incorporating the finite pulse rise time and inhomogeneous broadening due to fluctuations in  $\Delta B_{\text{nuc}}^z$ . c) An  $|\uparrow\downarrow\rangle = |X\rangle$  state is prepared by adiabatically turning off  $J$ . d) Representation of the measured and fitted trajectories in the Bloch sphere. In order to eliminate phase shifts due to the slightly different frequencies (see text), the time scales for the X-data has been rescaled using spline interpolation so that the expected phase relations are maintained. The blue line is a spline interpolation of the data points in panel b). e) Visualization of the X and Y-readout schemes on the Bloch sphere.

nating rotations around different axis allows to implement universal quantum control. We demonstrate and characterize the rotation around an arbitrary axes using state tomography, consisting of three independent measurements of the probability of being in a  $|S\rangle \equiv |Z\rangle$ , in

an  $|S\rangle + |T_0\rangle \equiv |\uparrow\downarrow\rangle \equiv |X\rangle$  and in a  $|S\rangle + i|T_0\rangle \equiv |Y\rangle$  state [16], with pulses shown in Fig. 5.7a.

This allows us to fully reconstruct the time evolution of the state vector. For each of the measurements, we first prepare an  $|\uparrow\downarrow\rangle$  state by loading a  $S(0,2)$  and adiabatically switching off  $J(\varepsilon)$  in (1,1).

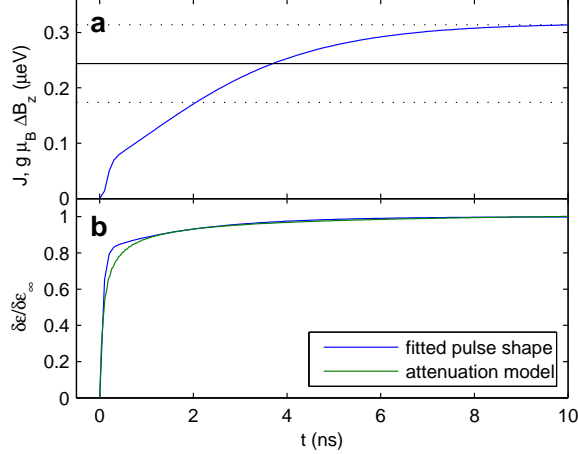


Figure 5.8: a) Time dependence of  $J$  according to the fit model described in the text (blue line). The black line shows  $\bar{\Delta}B_{nuc}^z$ , the mean of  $\Delta B_{nuc}^z$ , and the dashed lines indicate the rms fluctuation amplitude,  $\delta\Delta B_{nuc}^z$ . b) Pulse shape corresponding to  $J(t)$  from a) (blue line). The sharp kink is an artifact of the pulse parametrization. The green line shows the pulse expected from a step function transmitted through a lossy coax cable, with a time constant obtained by comparing the same model to the measured pulse shape on a similar experimental setup.

The desired rotation is performed by quickly setting  $J$  to a finite value for a time  $\tau_{rot}$ . Rapidly returning to  $S(0,2)$  allows to measure  $p(|Z\rangle) \equiv |\langle Z|\psi\rangle|^2$ , whereas slowly increasing  $J$  brings  $|\uparrow\downarrow\rangle$  onto  $|S\rangle$  and  $|\downarrow\uparrow\rangle$  onto  $|T_0\rangle$ , thus allowing the readout of  $p(|X\rangle) \equiv |\langle X|\psi\rangle|^2$ . To obtain  $p(|Y\rangle) \equiv |\langle Y|\psi\rangle|^2$ ,  $J$  is turned off for a time corresponding to a  $\pi/2$  rotation around the  $x$ -axis before rapidly returning to  $\mathbf{M}$ . Results of this procedure for a particular choice of  $J$  and  $\Delta B_{nuc}^z$  are shown in Fig. 5.7c as a function of  $\tau_{rot}$ . For ideal pulses, one would expect  $p(|X\rangle)$  to oscillate sinusoidally between 1 and  $(1+\cos(2\theta))/2$ ,  $p(|Z\rangle)$  between 1/2 and  $(1+\sin(2\theta))/2$ , whereas  $p(|Y\rangle)$  should vary symmetrically around 1/2. Deviations from this

behavior can be attributed to a finite pulse rise time and high pass filtering of the pulses. The first causes an approximately adiabatic drift of the rotation axis which prevents  $p(|Z\rangle)$  to return to the starting point, whereas the second leads to slightly different  $\varepsilon$ -offsets and thus different  $J(\varepsilon)$  for different pulses, causing a  $\approx 25\%$  frequency change. Fits to a model (Fig. 5.7b, see next section) incorporating these effects and inhomogeneous broadening due to fluctuations in  $\Delta B_{nuc}^z$  give a good match with the data. In Fig. 5.7d, the data and fits are displayed in the Bloch sphere representation. We estimate that the errors due to measurement noise, pulse imperfections other than those included in the model, incomplete ensemble averaging over nuclear fluctuations and uncertainties in the QPC conductance calibration are on the order of 0.15 for all three probability measurements. They could be substantially reduced by improving the characteristics of our high frequency setup, such that pulse compensation schemes would be simpler and pulse dependent variations of  $J$  could be eliminated.

### 5.7.1 Model for the analysis of the tomography data

While the contrast in the measurement triangle should be a direct measure of the singlet return probability, we found empirically that it varies with polarization, position of the measurement point  $\mathbf{M}$ , and pulse shape. In the tomography measurement (Fig. 5.7) we account for the imperfect pulse shape errors by monitoring the QPC signal from a reference pulse without any excursion to (1,1) and the  $\tau_{rot} = 0$  pulses to convert the measured signal to probabilities. Both the reference pulse and the  $\tau_{rot} = 0$  X-pulse should produce a singlet-like signal. However, because of direct coupling of the pulses to the QPC, the two pulses result in a slightly different QPC conductance. This correction is approximately proportional to the time spent in (1,1) and thus mostly due to the long ramps for preparation and X-readout.

For the Y and Z-pulses, which contain only one ramp each, we have used the average of the signals from the reference pulse (no ramp) and the  $\tau_{rot} = 0$  X-pulse (two ramps) to determine  $p(|S\rangle) = p(|Z\rangle) = 1$  and  $p(|S\rangle + i|T_0\rangle) = p(|Y\rangle) = 1$ , while  $p(|Z\rangle) = 1/2$  and  $p(|Y\rangle) = 1/2$  are determined from the average of the  $\tau_{rot} = 0$  Y and Z-pulse signals. For the X-pulse, only the  $p(|\uparrow\downarrow\rangle) = p(|X\rangle) = 1$  signal can be determined reliably. We have thus adjusted the remaining scaling factor manually such that the amplitude of the Y-signal obtained from the fits as described below matches the data.

To fit the tomography data, we have numerically solved the Schrödinger equation for the Hamiltonian  $H = J(t)/2\sigma_z + g\mu_B\Delta B_{nuc}^z/2\sigma_x$ , with a time dependence of  $J$  reflecting the finite rise time of the pulses. We have parametrized  $J(\varepsilon)$  by a phenomenological exponential dependence  $J(\varepsilon) \propto e^{\varepsilon/\epsilon}$  that approximates our measurements of the frequency of exchange oscillations [13, 91] as a function of  $\varepsilon$ . The time dependence of  $\varepsilon$  was modeled as  $\varepsilon(t) - \varepsilon(t=0) \propto 1 - \alpha e^{-t/\tau_1} + (1 - \alpha)e^{-t/\tau_2}$ . The time dependence of  $\varepsilon$  and  $J$  obtained from the fits is shown in Fig. 5.8. The model was chosen such that it can produce a pulse shape with an initial fast rise followed by a slow decay. This behavior is expected because of the frequency dependent attenuation of the coaxial cables (see Fig. 5.8b) and other bandwidth limitations and can also be observed in exchange pulses with  $\Delta B_{nuc}^z \ll J$ . For comparison, the specified 10 to 90 % rise time of our pulse generator is 1.5 ns.

When switching on  $J$  at the end of the preparation ramp, the fast part of the pulse is in a region where  $J(\epsilon) \ll \Delta B_{nuc}^z$ , so that  $J$  increases significantly only in the slow phase of the pulse, leading to a slow rise of  $J(t)$ . When switching off  $J$  or returning to (0,2),  $J$  varies strongly in the fast part of the pulse, so that an infinitely sharp rise is a good approximation. We have thus only considered the effect of a finite rise time when switching on  $J$ . To account for fluctuations in  $\Delta B_{nuc}^z$ , we have taken a weighted average of simulation

results for a range of  $\Delta B_{nuc}^z$  with Gaussian weights.

The data from the X and Z-pulses (Fig. 4b) were fitted simultaneously with the following fit parameters:  $\alpha = 0.19$ ,  $\tau_1 = 2.0$  ns,  $\tau_2 = 0.064$  ns,  $\epsilon = 0.44$  mV (normalized as change in gate voltages, i.e.  $\sqrt{\Delta V_{GL}^2 + \Delta V_{GR}^2}$ ),  $J_X = 0.32$   $\mu\text{eV}$ ,  $J_Z = 0.45$   $\mu\text{eV}$ ,  $\overline{\Delta B_{nuc}^z} = 10.5$  mT,  $\delta\Delta B_{nuc}^z = 4.3$  mT.  $\overline{\Delta B_{nuc}^z}$  and  $\delta\Delta B_{nuc}^z$  denote the mean and standard deviation of the  $\Delta B_{nuc}^z$  distribution and  $J_X$  and  $J_Z$  the asymptotic value of  $J$  for the X and Z-pulse. Ideally, one could set  $J_X = J_Z$ , however in our data, different offsets to the pulses due to the DC blocking effect of our bias tee's lead to an approximately 25% difference. All other parameters were the same for both the X and the Z-fit. The model curve shown for Y was computed with the same parameter values and  $J_Y = J_Z$ . This is reasonable because the overall pulse shape of the Y-pulse is more similar to the one of the Z-pulse than the one of the X-pulse (see Fig. 5.7a). In the Bloch sphere representation of the model in Fig. 5.7d, the  $J_Z$  value was used for all three coordinates.

## 5.8 Conclusions

The mechanism responsible for the large gradient due to pumping is currently unknown. One possible cause is an asymmetry in the size of the two dots due to local disorder. Both the probability to flip a nuclear spin in one of the dots and the change in hyperfine field due to that flip are inversely proportional to the number of nuclei N over which the electron wave function extends [92]. The overall  $1/N^2$  dependance results in the smaller dot being polarized more rapidly. Different relaxation rates in the two dots and more complex aspects of the nuclear dynamics may also play a role [93]. The relation between our results and those in Ref. [17], where a strong suppression of  $\Delta B_{nuc}^z$  was reported, is currently under investigation. The apparent contradiction with the observation of Reilly *et al.* [89] that

*S*-pumping becomes ineffective at fields exceeding a few tens of mT might be due to a different coupling between the dots and to the electron reservoirs as shown in the previous section.

We demonstrated the ability to perform universal single qubit operations in sub nanosecond time scales [94], two orders of magnitude faster than previously shown for single spin qubits [95, 96, 43]. These short operation times together with the demonstrated coherence times of a few microseconds [13] and predicted coherence times of up to 100  $\mu$ s [97, 98, 99] suggest that the requirements for quantum error correction of two-electron spin qubits are within reach. Furthermore, our ability to record the magnetic field gradient opens the way towards feedback control of the nuclear environment that would prolong  $T_2^*$  and thereby reduce the number of error correcting pulses needed.

## Chapter 6

# Enhancing the coherence of Spin Qubits by Narrowing the Nuclear Spin Bath Using a Quantum Feedback Loop

Hendrik Bluhm<sup>1†</sup>, Sandra Foletti<sup>1†</sup>, Diana Mahalu<sup>2</sup>, Vladimir Umansky<sup>2</sup> and Amir Yacoby<sup>1</sup>

1. Department of Physics, Harvard University, Cambridge, MA 02138, USA  
2. Braun Center for Submicron Research, Department of Condensed Matter Physics,  
Weizmann Institute of Science, Rehovot 76100, Israel

† These authors contributed equally to this work.

In many realizations of electron spin qubits the dominant source of decoherence is the fluctuating nuclear spin bath of the host material. The slowness of this bath lends itself to a promising mitigation strategy where the nuclear spin bath is prepared in a narrowed

state with suppressed fluctuations. Here, this approach is realized for a two-electron spin qubit in a GaAs double quantum dot and a nearly ten-fold increase in the inhomogeneous dephasing time  $T_2^*$  is demonstrated. Using the qubit to both measure and polarize its nuclear environment creates a quantum feedback loop that directly conditions the nuclear polarization rate on a quantum limited measurement of the hyperfine field seen by the same qubit. This procedure also maintains an average polarization enabling fast universal qubit control. These results indicate that suppressing nuclear fluctuations could allow gate fidelities of 99.99%, on the order of the quantum error correction threshold<sup>1</sup>.

## 6.1 Introduction

Spins in semiconductor are attractive qubits because of their long coherence times [101, 102, 10], their electrical control and readout [13], and their potential for scalability [41]. Few electron quantum dot devices have been used successfully in recent years to demonstrate universal control of electron spin qubits as well as single shot readout [103, 83, 67, 81]. However, interaction of the qubit spin(s) with nearby nuclear spins is a significant source of decoherence in several systems [13, 10, 95, 104, 102]. It is therefore very attractive to prepare the spin environment of the electron in a way that mitigates this decoherence. One approach would be to polarize the nuclei [105], but a nearly complete polarization is required for improved coherence [106], which is difficult to realize. Alternatively, one can narrow the distribution of the fluctuating effective field from the spin bath, for example through repeated projective measurements [107] or feedback. In addition to the reduced decoherence, such a narrowed state is of great interest for studying the long-time quantum

---

<sup>1</sup>This chapter is adapted from Ref. [100].

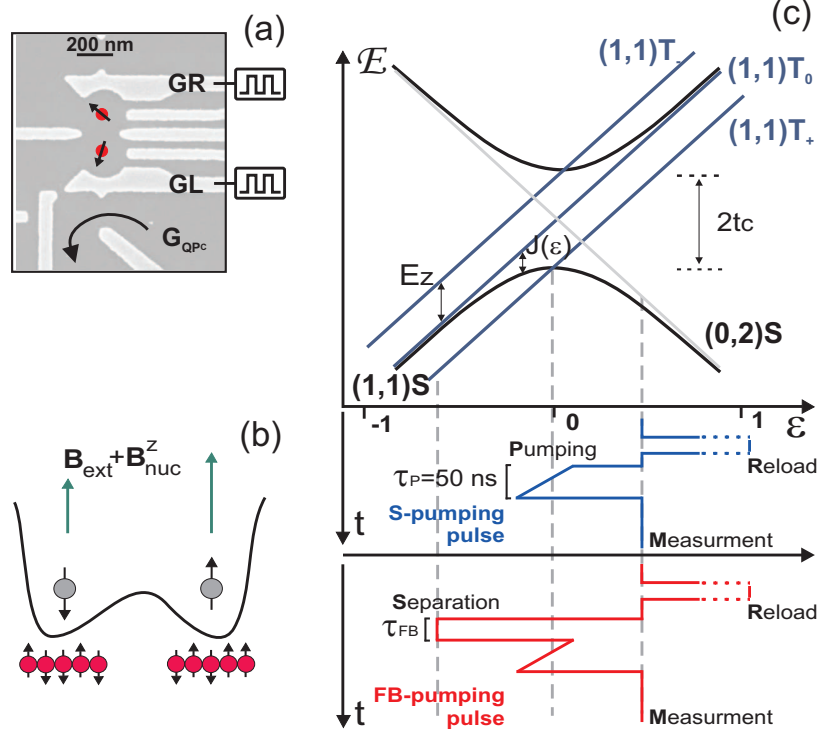


Figure 6.1: a) Scanning electron micrograph of a device similar to the one measured. The bright structures are metal gates that confine two electrons. The conductance  $G_{QPC}$  of the quantum point contact reflects the charge state of the double dot. b) Illustration of the dynamics for fully separated electrons. The energy splitting between  $|\uparrow\downarrow\rangle$  and  $|\downarrow\uparrow\rangle$  is proportional to the hyperfine field gradient across the two dots. This level splitting results in coherent oscillations between  $|S\rangle$  and  $|T_0\rangle$ . c) Top: Energies of the relevant spin states as a function of the detuning  $\varepsilon$ , which can be controlled with nanosecond time resolution by applying voltage pulses to gates GL and GR. Bottom: Schematic of  $\varepsilon(t)$  for the  $S$  and feedback pump pulses. The total duration of a single pulse is 250 ns.

dynamics arising from the spin-bath interaction [99]. Nuclear narrowing due to feedback mechanisms in quantum dots was recently inferred from resonance locking experiments under microwave [108] and optical irradiation [109, 110, 111], but an enhancement of the coherence of individual qubits has not been demonstrated so far. In these experiments, the feedback mechanism is intrinsic to the polarization dynamics [112, 113].

Here, we present a narrowing method that conditions the rate at which the bath is dynamically polarized on a previously executed, quantum limited measurement of its current polarization state. The nonzero average polarization and the associated hyperfine field

obtained with our method is essential for universal fast electrical control of the qubit (see Chap. 5). In contrast, Ref. [88] reported a complete elimination of gradients also enhancing  $T_2^*$ , but it has now become clear that there is a more likely interpretation of the experiment that does not involve suppressing nuclear fluctuations [114].

Our method is based on manipulating the environment via the very same qubit whose coherence time is to be extended. This ability allows us to condition the control of the environment on the dynamics of the qubit without the need to measure the state of the qubit. The qubit itself thus forms a feedback loop performing quantum limited measurements on the variable to be controlled.

## 6.2 Description of the system

The spin qubit studied in this work consists of two electrons confined in a double well potential. This double quantum dot is created by applying negative voltages on metallic gates that locally deplete a two dimensional electron gas (2DEG) residing 90 nm below the wafer surface (see Fig. 6.1a). Each dot is tunnel coupled to a lead and the inter-dot tunnel coupling is  $t_c \sim 10 \mu\text{eV}$ . The phase space of our qubit consists of superpositions of the singlet  $|S\rangle \equiv (|\uparrow\downarrow\rangle - |\downarrow\uparrow\rangle)/\sqrt{2}$  and the triplet state  $|T_0\rangle \equiv (|\uparrow\downarrow\rangle + |\downarrow\uparrow\rangle)/\sqrt{2}$ , where the arrows represent the orientation of each electron spin. Both these states have a vanishing  $z$ -spin. The remaining two states with a total  $z$ -spin of  $\pm 1$ ,  $|T_+\rangle \equiv |\uparrow\uparrow\rangle$  and  $|T_-\rangle \equiv |\downarrow\downarrow\rangle$ , are energetically separated by the Zeeman energy  $E_Z = g^*\mu_B B_{ext}$  induced by an external magnetic field  $B_{ext}$  and are not used for information storage.

Encoding the qubit in a logical subspace of the complete phase space of two electron spins rather than a single spin enables fast electrical control via the exchange interaction between the two spins [39, 13, 81]. This control technique relies on changing the energy

difference,  $\varepsilon$ , between states with both electrons in one dot and one electron in each dot, denoted by (0,2) and (1,1), respectively [13, 81].  $\varepsilon$  can be thought of as controlling the separation between the two electrons. The energies of the four spin states depend on this parameter as shown in Fig. 6.1c. High frequency coaxial lines connected to two gates, GL and GR, allow rapid changes of  $\varepsilon$ .

Deep in (1,1) ( $\varepsilon < 0$ ), the electrons are entirely separated, and acquire a phase at a rate proportional to the magnetic field in each dot (see Fig. 6.1b). These local fields are the sum of the homogeneous applied field  $\mathbf{B}_{ext}$  and a hyperfine field proportional to the nuclear polarization parallel to  $\mathbf{B}_{ext}$ . Any difference  $\Delta B_{nuc}^z$  between the two hyperfine fields leads to coherent oscillations of the qubit's state between  $|S\rangle$  and  $|T_0\rangle$  with a frequency  $g^* \mu_B \Delta B_{nuc}^z / h$ , where  $g^* = -0.44$  is the g-factor in GaAs,  $h = 6.6 \cdot 10^{-34}$  J·s is Planck's constant and  $\mu_B = 9.3 \cdot 10^{-24}$  J/T the Bohr magneton. Throughout this work,  $B_{ext} = 0.7$  T was applied along the  $z$ -axis, parallel to the 2DEG.

The (0,2) charge configuration ( $\varepsilon > 0$ ) is energetically accessible only for a spin singlet state because for a triplet state, Pauli exclusion would force the second electron into an excited orbital state. This energy difference allows the rapid initialization of the qubit in a singlet state  $S$  by exchange of an electron through a lead. It also enables readout of the spin states: only the singlet configuration transitions from (1,1) to (0,2) when increasing  $\varepsilon$ , whereas the triplets remain blocked in (1,1). These two charge states can be distinguished using a nearby charge sensor, in our case a quantum point contact whose conductance,  $G_{QPC}$ , depends on its electrostatic environment.

### 6.3 Probing the local nuclear magnetic field gradient

To probe the local magnetic field gradient  $\Delta B_{nuc}^z$ , we prepare a singlet state in (0,2) and then rapidly change  $\varepsilon$  to (1,1), where the electrons evolve for a variable separation time  $\tau_S$  until  $\varepsilon$  is reset to (0,2). After a measurement time of about 10  $\mu\text{s}$ , the cycle is repeated. The charge sensor signal  $G_{QPC}$  averaged over several thousand pulse repetitions varies proportional to the probability  $P_S$  of the electron being in a singlet state after the evolution time  $\tau_S$ . Repeating such measurements for a range of  $\tau_S$  enables us to probe the coherent precession of the qubit (see inset to Fig. 6.2a), whose frequency  $f$  is related to the field gradient by  $\Delta B_{nuc}^z = hf/g\mu_B$ . Fitting a sine curve every time such a  $\tau_S$  sweep is completed yields a time trace of  $\Delta B_{nuc}^z$  with a sampling rate of about 1 Hz. The fluctuations in this time trace reflect slow random variations of the nuclear polarization [115].

An improvement of our signal to noise ratio allowed us to increase the acquisition rate by a factor 30 compared to the acquisition rate used for the measurement presented in Chap. 5. The  $P_S$  vs.  $\tau_S$  curves as shown in the inset to Fig. 6.2a were sampled at a rate of 32 data points per second, so that the whole curve can be acquired within 0.55 s. The actual sample rate of  $\Delta B_{nuc}^z$  was reduced to about 1 Hz by the time required for data transfer and polarization between measurements, with the precise value depending on the polarization time.

### 6.4 $S$ and $T_+$ pumping cycles

The knowledge of the instantaneous field gradient allows us to use pump cycles that increase or decrease the gradient to compensate the fluctuations of the spin bath. These pump cycles, presented in Chap. 5 use the degeneracy point of  $|S\rangle$  and  $|T_+\rangle$ , where a combination of the

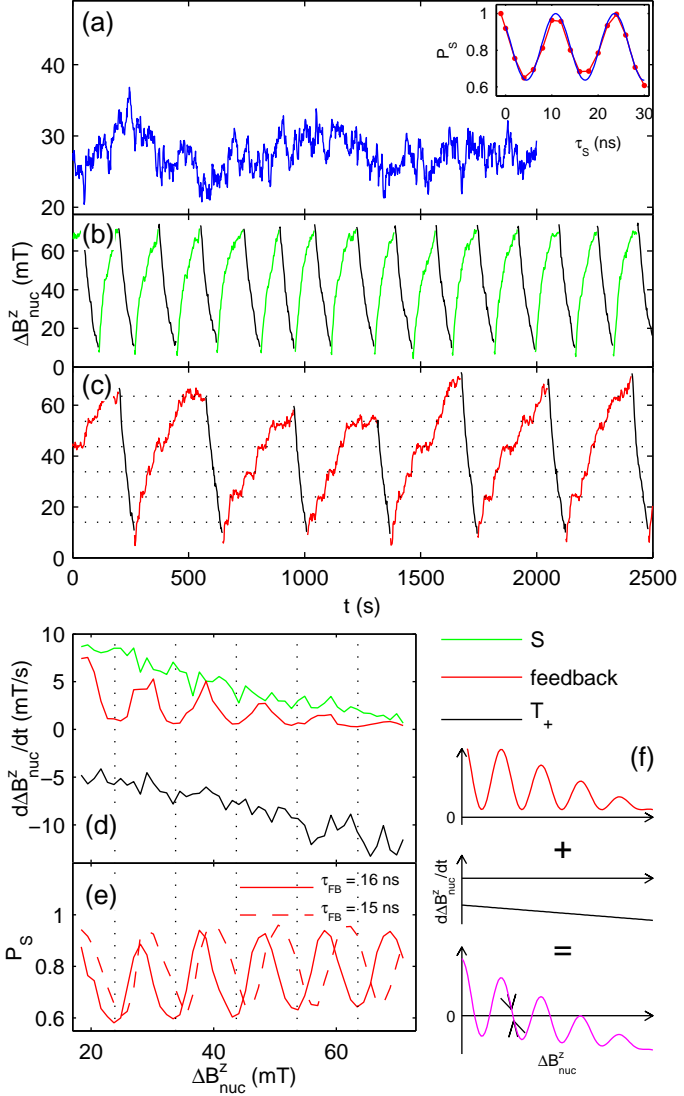


Figure 6.2: a) Time trace of  $\Delta B_{nuc}^z$  showing the fluctuations of the nuclear hyperfine field. The nonzero mean of  $\Delta B_{nuc}^z$  is due to pumping (without feedback) between measurements. Each data point reflects a fit to the  $S-T_0$  precession rate as shown in the inset. b) Same, but alternating between 0.4 s  $S$  and  $T_+$ -pumping between measurements. c) Same for a feedback pulse with  $\tau_{FB} = 15$  ns and  $T_+$ . d) Pump rates extracted by averaging over time traces such as those in panels (b) and (c), but much longer.  $d\Delta B_{nuc}^z/dt$  is normalized by the time spent pumping. e) Singlet probability  $P_S$  after a fixed mixing time  $\tau_S$  as a function of  $\Delta B_{nuc}^z$ , extracted from the same data as the red curves in panels c) and d) The polarization stagnates at the dotted lines in panels c)-e) because the qubit is swept through the  $S-T_+$  transition in a  $T_0$  state. The modulation of  $d\Delta B_{nuc}^z/dt$  for the feedback pulse between 0 and the  $S$ -pump value according to  $P_S$  for  $\tau_S \approx \tau_{FB}$  confirms the intended feedback effect. The difference between  $\tau_{FB} = 15$  ns and  $\tau_S = 16$  ns giving the best match probably reflects finite pulse rise times. f) Illustration of the feedback mechanism. Stable fixed points where  $d\Delta B_{nuc}^z/dt$  changes sign with a negative slope result from combining feedback and  $T_+$ -pumping. Fluctuations of  $\Delta B_{nuc}^z$  away from these points are quenched by a restoring pump effect (arrows).

inter-dot tunnel coupling and  $\varepsilon$  compensates the Zeeman splitting  $E_Z$  (see Fig. 6.1c). In the so called  $S$ -pumping cycle, we prepare a singlet and then sweep through the  $S-T_+$  transition, where transfer of spin from the electrons to the nuclei builds up a mean polarization  $B_{nuc}^z$  of the same sign as the applied field. In the  $T_+$ -pumping cycle, a  $T_+$  state is preferentially prepared by allowing each electron to relax to the spin-up state via coupling to the leads before sweeping through the  $S-T_+$  transition. This results in a polarization of opposite sign. How these pump cycles affect  $\Delta B_{nuc}^z$  depends on the imbalance of the nuclear spin flip probabilities in each of the dots [116], which is difficult to predict. Experimentally, we can probe their effect by running them between measurements of  $\Delta B_{nuc}^z$ . We find that starting from any nonzero field gradient, the two pump cycles change the gradient in opposite directions. If the gradient reaches zero while pumping, it immediately increases again, which suggests a sign change (as shown in Chap. 5).

## 6.5 Local magnetic field fluctuations

To characterize the effectiveness of pumping, we alternate between  $S$  and  $T_+$ -pumping in a way that causes  $\Delta B_{nuc}^z$  to oscillate between two predetermined limits, as shown in Fig. 6.2b. Averaging over many such cycles yields the mean rate of change of the gradient,  $\Delta B_{nuc}^z/dt$ , as a function of its value  $\Delta B_{nuc}^z$  (see Fig. 6.2d). The approximately linear relation between the two reflects the relaxation of the polarization due to spin diffusion.

When pumping for a fixed time with either pumping cycle,  $\Delta B_{nuc}^z$  saturates once pumping and relaxation balance each other, but continues to fluctuate on time scales of up to minutes, with an rms-amplitude  $\delta\Delta B_{nuc}^z$  of about 3 mT (see Fig. 6.2a). These fluctuations lead to a decay of coherent  $S-T_0$  oscillations after a time  $T_2^* = h/2\sqrt{2}g^*\mu_B\delta B_{nuc}^z = 14$  ns when ensemble-averaging over many  $\tau_S$  sweeps (see Fig. 6.3a).

## 6.6 Feedback schemes

### 6.6.1 Software feedback

Our ability to rapidly measure and manipulate the gradient  $\Delta B_{nuc}^z$  enables us to narrow its distribution using two feedback schemes. In the first, software based scheme, we fed the measured value of  $\Delta B_{nuc}^z$  into a standard proportional-integral feedback loop whose output determined the duration and type of pumping before the next measurement. This procedure reduced the fluctuations in the gradient,  $\delta\Delta B_{nuc}^z$ , by about a factor of two, corresponding to  $T_2^* \approx 30$  ns. Its limiting factor was the sampling rate of  $\Delta B_{nuc}^z$ . A faster readout technique [76, 67] could thus improve the performance.

For software feedback and measurements of the pump rate, we applied the pump pulses after every 10-20 measurements, each lasting 1/32 seconds. For the pulse feedback data shown in Figs. 6.3b,d (and presented in the next section), we pumped after each measurement of a single  $\tau_S$ , resulting in a total duration of the measurement-and-pump cycle of 100 ms. Slower repetition rates still work, but tend to result in larger fluctuations because of the longer time intervals of unstabilized fluctuations between pump cycles. Furthermore, the length of the pump intervals is limited by the requirement that  $\Delta B_{nuc}^z$  does not leave the region of attraction of the desired fixed point before switching the pump pulse.

### 6.6.2 Pulse feedback

While stabilizing the field from the nuclear spin bath via feedback inevitably requires measuring its instantaneous value, there is no fundamental need for the measurement outcome to be accessible to the experimenter. After evolving for a time  $\tau_S$ , the qubit itself already contains information about  $\Delta B_{nuc}^z$ . Our second feedback scheme, denoted here as 'pulse feedback', thus relies on directly incorporating the feedback mechanism into the polariza-

tion cycle by designing it such that nuclear spin flips are conditional on the dynamics of the qubit. After loading a  $|S\rangle$ ,  $\varepsilon$  is rapidly changed to (1,1) for a time  $\tau_{FB}$  (see Fig. 6.1c). During this time, the qubit's state oscillates between  $|S\rangle$  and  $|T_0\rangle$ , and the probability of ending in  $|S\rangle$  is given by  $(1 + \cos(g^* \mu_B \Delta B_{nuc}^z \tau_{FB} / h)) / 2$ . Upon sweeping  $\varepsilon$  through the  $S-T_+$  transition, a nuclear spin can only be flipped if the electron returned from (1,1) in the singlet state. Thus, one would expect the pump rate to be proportional to the singlet probability  $P_S$ . Indeed, the measured mean rate of change of the gradient,  $d\Delta B_{nuc}^z / dt$ , shows an oscillatory variation as a function of  $\Delta B_{nuc}^z$  between 0 and the maximum value obtained using a pure  $S$ -pumping pulse (see Fig. 6.2d).

### 6.6.3 Measurement of the pump rates

In order to obtain the pump rate data as plotted in Figs. 6.2b and c, we run the  $S$  or feedback pumping pulses until the gradient  $\Delta B_{nuc}^z$  exceeds a predetermined threshold, at which point the acquisition software switches to the  $T_+$ -pumping cycle. When the value of the gradient falls below a second lower threshold, the software switches back to  $S$  or feedback pumping. In the absence of fluctuations, the polarization effect of the feedback pulse would be expected to stagnate indefinitely at the plateaus visible in Fig. 6.2c. Pumping indeed tends to stop for shorter  $\tau_{FB}$ , where the pump probability varies less rapidly with  $\Delta B_{nuc}^z$ . For  $\tau_{FB} \gtrsim 15$  ns, fluctuations lead to a finite dwell time at those unstable fixed points.

The raw data obtained from repeating many of the above cycles is a series of curves of  $P_S$  vs.  $\tau_S$  as shown in the inset of Fig. 6.2a. Obtaining the oscillation frequencies by fitting a sine curve to each of them results in time traces of  $\Delta B_{nuc}^z$ , part of which are shown in Figs. 6.2b and c. Taking the difference between subsequent values yields a time trace of the pump rate,  $\Delta B_{nuc}^z(t)/dt$ , which is rather noisy because of the numerical differentiation.

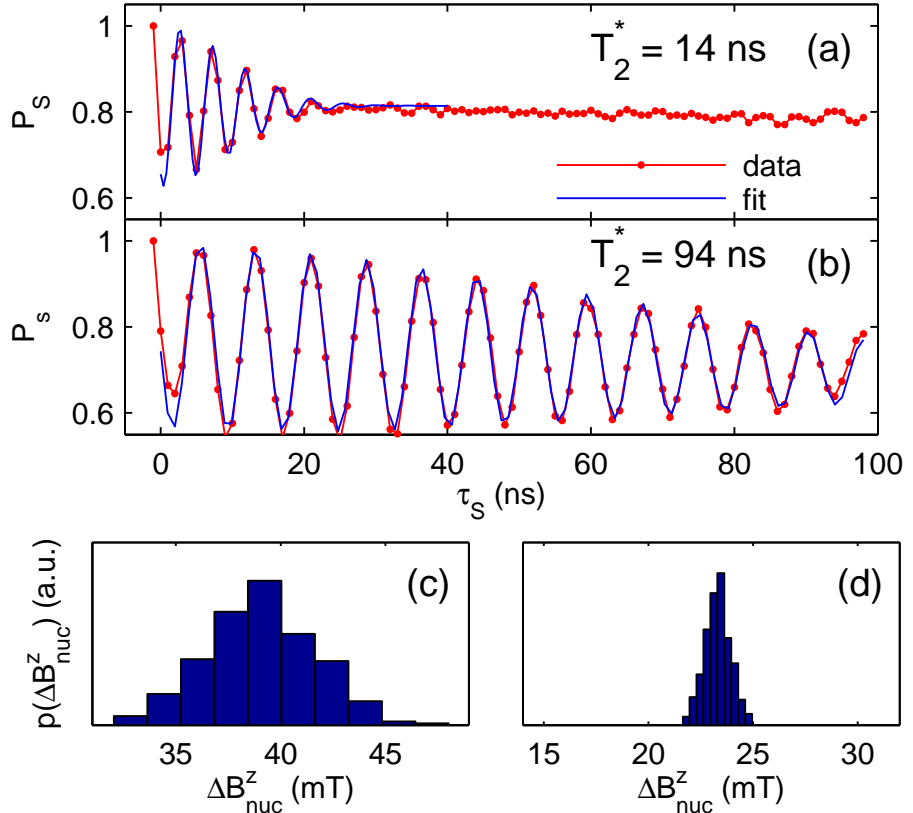


Figure 6.3: a) Ensemble average of  $S-T_0$  oscillations for fixed pumping (0.7 s  $T_+$ -pumping and 0.25 s  $S$ -pumping repeated every 2.2 s). The pumping maintains a nonzero  $\Delta B_{nuc}^z$  whose fluctuations lead to a dephasing time of  $T_2^* = 14$  ns. Other pump times give different oscillation frequencies, but similar dephasing times.  $P_S$  is normalized as in Chap. 5. b) Same measurement, but for 30 ms of feedback pumping with  $\tau_{FB} = 30$  ns and 31 ms of  $T_+$ -pumping after each 39 ms long measurement. The feedback extends  $T_2^*$  to 94 ns. The blue lines show the fits to  $1 - P_S \propto 1 + \sin(g^* \mu_B \Delta B_{nuc}^z \tau_S / h) e^{-(\tau_S/T_2^*)^2} + \alpha \tau_S$  used to extract  $T_2^*$ . The linear term in the fit model accounts for crosstalk of the gate pulses to the charge sensor. c), d) Corresponding distributions of  $\Delta B_{nuc}^z$ , obtained by extracting instantaneous values of  $\Delta B_{nuc}^z$  before ensemble averaging without c) and with pulse feedback d).

To average out this noise, we have binned this trace according to the corresponding values of  $\Delta B_{nuc}^z$ , and computed the mean  $\Delta B_{nuc}^z(t)/dt$  for each bin, as shown in Fig. 6.2d. The curves in Fig. 6.2e were obtained by applying the same binning procedure to the  $P_S$  value for  $\tau_S = 15$  and 16 ns taken from each  $\tau_S$  sweep.

The bare polarization rate, obtained at small  $\Delta B_{nuc}^z$  where relaxation is weak, can reach values of up to 40 mT/s. The relaxation rate, which determines the slope of the pump curves in Fig. 6.2d, depends on the pumping history, as expected for diffusive relaxation. The largest pump rates observed at  $B_{ext} = 0.7$  T correspond to about one nuclear spin flip per 150 cycles. While our measurements of the rate of change of  $\Delta B_{nuc}^z$  is sensitive to the difference between the flip probabilities in each dot, we found that the field gradient  $\Delta B_{nuc}^z$  and the mean hyperfine field  $B_{nuc}^z$  tend to be of the same order (see Chap. 5). Thus, the total spin flip probability should be similar to the measured differential value.

When sweeping through the  $S-T_+$  transition,  $\varepsilon$  is ramped by about 50  $\mu\text{eV}$  in 50 ns, whereas the expected hyperfine coupling is  $g^*\mu_B\delta B_{nuc}^z = 70$  neV. Setting  $dJ/d\varepsilon$  to one, which becomes accurate for large fields with a Zeeman splitting much larger than the inter-dot tunnel coupling, the Landau-Zener formula would predict a flip probability of  $1 - \exp(-2\pi(0.07\mu\text{eV})^2/(\hbar \cdot 1\mu\text{eV}/\text{ns})) \approx 0.05$ . The magnetic field used in the experiments is comparable to rather than much larger than the tunnel coupling, which would increase the actual flip probability. On the other hand, the discreteness of the ramps with steps of about 2  $\mu\text{eV}$  in  $\varepsilon$  and possibly gate noise may reduce the flip probability compared to the Landau-Zener result. Independent measurements show that the probability for the electrons' state to change from  $S$  to  $T_+$  is on the order of 1/2. The quantitative details of the electronic and nuclear spin flip probabilities are currently not well understood.

## 6.7 Stable gradients

Similar to  $S$ -pumping, the feedback cycle pumps nuclei in one direction only. When the pump rate approaches zero, polarization stagnates until a fluctuation pushes the state beyond the unstable fixed point, which results in step-like structures in the time traces of Fig. 6.2c. In order to obtain a stable gradient, the pump rate has to cross zero with a negative slope at the desired value of  $\Delta B_{nuc}^z$ . Such a sign change can be engineered by alternating between the feedback pulse and the  $T_+$ -pumping pulse (see Fig. 6.2e).

In order to obtain a stable fixed point by combining  $T_+$ -pump and feedback pulses, we initially chose the pump times such that the  $T_+$ -pumping pulse alone reduces the gradient  $\Delta B_{nuc}^z$  approximately at half the rate at which  $S$ -pumping increases it. Thus, the fixed point where the effects of the two pulses cancel should be at a singlet probability of 1/2, where the feedback gain  $\partial P_S / \partial \Delta B_{nuc}^z$  is largest. We have verified that the effect of combining different pump pulses is qualitatively additive by comparing the pump rate of the  $S$  and  $T_+$  pulses individually to the pump rate of the combination.

We typically used a  $\tau_{FB}$  between 15 and 30 ns. Larger  $\tau_{FB}$  slightly improve  $T_2^*$ , but increase the frequency of occasional jumps between adjacent fixed points due to fluctuations. The frequency of such switching events can be minimized by fine tuning the ratio of  $T_+$  and feedback pumping, and it is possible to return to the desired stable value of  $\Delta B_{nuc}^z$  by temporarily using a different pump pulse or time.

Running this pulse combination for a fixed time between measurements locks the gradient near expected values with reduced fluctuations. The data shown in Fig. 6.3b,d demonstrate a more than sixfold enhancement of  $T_2^*$  to 94 ns and the corresponding narrowing of the distribution of  $\Delta B_{nuc}^z$ . Here, the pump pulses were applied for 61 ms per 100 ms interval.

## 6.8 Conclusions

The narrowing of the nuclear environment using quantum feedback promises a substantially improved gate fidelity. Because it is more difficult to decouple gate operations from a fluctuating bath than to maintain the state of a qubit, this aspect is of great technological importance. For a 1 ns  $\pi$ -rotation generated by a gradient of 100 mT (see Chap. 5) with rms fluctuations of  $\delta\Delta B_{nuc}^z = 0.5$  mT as demonstrated here, the error per gate operation is  $\pi^2 \delta\Delta B_{nuc}^z / 4\Delta B_{nuc}^z \lesssim 10^{-4}$  [117]. However, due to the slowness of the nuclear bath, an error of order unity accumulates after only 100 such gate operations. This limitation could be overcome by implementing gates that are insensitive to  $\delta\Delta B_{nuc}^z$  to first order [118]. A pulse angle error of order  $\delta\Delta B_{nuc}^z / \Delta B_{nuc}^z \sim 10^{-4}$  would allow  $10^4$  operations per error. In either case, the improvement in gate fidelity is at least quadratic in the narrowing ratio. Thus, narrowing procedures are very effective at overcoming the limitations imposed by a fluctuating nuclear spin bath.

## Chapter 7

# Long coherence of electron spins coupled to a nuclear spin bath

Hendrik Bluhm<sup>1†</sup>, Sandra Foletti<sup>1†</sup>, Izhar Neder<sup>1</sup>, Mark S. Rudner<sup>1</sup>, Diana Mahalu<sup>2</sup>,  
Vladimir Umansky<sup>2</sup> and Amir Yacoby<sup>1</sup>

1. Department of Physics, Harvard University, Cambridge, MA 02138, USA  
2. Braun Center for Submicron Research, Department of Condensed Matter Physics,  
Weizmann Institute of Science, Rehovot 76100, Israel

† These authors contributed equally to this work.

Qubits, the quantum mechanical bits required for quantum computing, must retain their fragile quantum states over a long period of time. For many types of electron spin qubits, the primary source of decoherence arises from their interaction with the nuclear spins of the host lattice. For electrons in gate defined GaAs quantum dots, previous spin echo measurements have revealed coherence times of about 1  $\mu$ s at magnetic fields below 100 mT [13, 119]. Here, we show that coherence in such devices can actually survive to much longer times and provide a detailed understanding of nuclear induced decoherence. At fields above a

few hundred millitesla, the lifetime of a single-pulse spin echo signal extends to 30  $\mu$ s. At lower magnetic fields, the echo signal first collapses, but then revives at later times given by the period of the relative Larmor precession of different nuclear species. This behavior is quantitatively accounted for by a semi-classical model for the electron spin dynamics in the presence of a nuclear spin bath extending earlier work [14, 54]. Using a multiple-pulse Carr-Purcell-Meiboom-Gill echo sequence, the decoherence time can be extended to more than 200  $\mu$ s, which represents an improvement by two orders of magnitude compared to previous measurements [13, 119, 120]. This demonstration of effective methods to mitigate nuclear induced decoherence puts the quantum error correction threshold within reach<sup>1</sup>.

## 7.1 Introduction

The promise of quantum dot spin qubits as a solid state approach to quantum computing is demonstrated by the successful realization of initialization, control and single shot readout of electron spin qubits in GaAs quantum dots using optical [83], magnetic [34], and fully electrical [81, 96, 67] techniques. To further develop such devices, it is vital to understand and mitigate decoherence due to the interaction of the electron spin with the nuclei of the host material, which is also a very interesting problem in its own right [99, 122].

Through the hyperfine interaction, an electron spin in a GaAs quantum dot is subjected to an effective magnetic field produced by the nuclear spins. Under typical experimental conditions, this so called Overhauser field has a random magnitude and direction. When the precession of an electron spin in this field is averaged over many experimental runs and hence Overhauser field configurations, the coherence signal is suppressed for evolution

---

<sup>1</sup>This chapter is adapted from Ref. [121].

times  $\tau \gtrsim T_2^* \approx 10$  ns [13]. However, because the time evolution of the nuclear spins is much slower than that of the electrons, it is possible to partially eliminate the effect of the random nuclear field by reversing the electron spin halfway through an interval of free precession [60]. Over short durations of this so called Hahn-echo experiment, the nuclear field is (nearly) constant, and its contributions to the electron spin precession before and after the spin-reversal (approximately) cancel out, thus restoring the initial electronic state. As the evolution time becomes longer, the effective field acting on the electron spin generally changes between the two halves of the precession interval. These fluctuations lead to an eventual loss of coherence on a timescale determined by the details of the nuclear spin dynamics.

Previous Hahn-echo experiments with GaAs quantum dot spin qubits have demonstrated spin dephasing times of about 1  $\mu$ s at magnetic fields below 100 mT [13, 119]. Recent theoretical studies of decoherence due to the hyperfine interaction [97, 14, 54] are generally consistent with these experimental results, but also predict revivals of the echo signal after several microseconds. Furthermore, much longer coherence times are expected at higher external magnetic fields [86] and/or with the introduction of more advanced decoupling schemes than the simple Hahn-echo pulse sequence, such as the Carr-Purcell-Meiboom-Gill (CPMG) [62, 123], concatenated dynamic decoupling [124, 125] or Uhrig's dynamic decoupling sequences [126, 127]. The performance of such schemes generally improves as more control pulses are added [127]. Initial experimental evidence for the effectiveness of CPMG for our system was already noted in Ref. [13].

Here we present the results of Hahn-echo and CPMG experiments on a two-electron GaAs double quantum dot spin qubit in external magnetic fields of  $B_{ext} = 50\text{-}700$  mT. At high magnetic fields,  $B_{ext} \gtrsim 400$  mT, the probability of returning to the initial state

decreases monotonically with the duration of the experiment,  $\tau$ . The echo initially decays very slowly (proportional to  $\tau^4$ ) and reaches  $1/e$  after about 30  $\mu\text{s}$ . For lower magnetic fields, we observe periodic collapses and revivals of the Hahn-echo signal, with a decaying revival amplitude at long times. The time and field dependence of the signal over the entire experimental parameter range is in excellent agreement with a semi-classical model that captures the effect of coherent precession and random fluctuations of the Overhauser field and exactly reproduces the results of Refs. [14, 54]. This model indicates that the collapses and revivals reflect the relative precession of different nuclear species with different Larmor frequencies. The revivals show that the initial decay of the echo does not reflect irreversible decoherence. Rather, it arises from averaging over the initial conditions of the fast but largely deterministic relative Larmor precession of the nuclei. At low fields, the overall decay of the revivals is mainly due to an approximately 0.3 mT spread of the Larmor frequencies of each species.

At higher fields, the effect of the precessing transverse nuclear fields is reduced by the larger Zeeman splitting. Thus, fluctuations of the Overhauser field component parallel to  $B_{ext}$  due to dipolar coupling between nuclei contribute significantly [86]. We model this effect with an additional factor  $\exp \{-(\tau/T_{SD})^4\}$  and find  $T_{SD} \approx 37 \mu\text{s}$ . We also identified and eliminated an artifact associated with shifts of the electron's position that can lead to a reduction of the measured coherence times. By employing a 16- $\pi$ -pulse CPMG sequence, we obtain an echo signal that decays linearly with a time constant exceeding 200  $\mu\text{s}$ .

## 7.2 Description of the system

The spin qubit studied in this work consists of two isolated electrons confined in a double quantum dot, created by applying negative voltages to metallic gates that locally deplete a

two dimensional electron gas (2DEG) 90 nm below the wafer surface (see Fig. 7.1a). The Hilbert space of our logical qubit is spanned by the states  $|\uparrow\downarrow\rangle$  and  $|\downarrow\uparrow\rangle$ , i.e. the  $m = 0$  subspace of two separated spins. The arrows represent the alignment of the electron spins in each of the dots relative to an external magnetic field,  $B_{ext}$ , which is oriented in the plane of the 2DEG. The remaining two states,  $T_+ \equiv |\uparrow\uparrow\rangle$  and  $T_- \equiv |\downarrow\downarrow\rangle$ , are energetically separated by the Zeeman energy  $E_Z = g^* \mu_B B_{ext}$  ( $g^* = -0.44$  is the  $g$ -factor in GaAs) and are not used for information storage. Tunnel coupling to the leads is used for initialization, while a variable inter-dot tunnel coupling allows spin exchange between the dots. The spin exchange between the two dots enables fast electrical control of the qubit [39, 13, 81].

### 7.3 Experimental procedures

We now briefly describe the experimental procedures, which are explained in more detail in Refs.[13, 81]. The most important parameter,  $\varepsilon$ , is the difference between the electrostatic potentials in the two dots. It is controlled via an antisymmetric change of the voltages on gates GL and GR (see Fig.7.1) applied via high frequency coaxial lines. When  $\varepsilon$  is large and positive, the ground state is a spin singlet with both electrons residing in a single dot. As  $\varepsilon$  is swept to negative values, the electrons separate into different dots, thus preparing a singlet state  $S \equiv (|\uparrow\downarrow\rangle - |\downarrow\uparrow\rangle)/\sqrt{2}$ . For very large negative detunings,  $\varepsilon \ll 0$ , the electron spins in the two dots are decoupled, and each individually experiences a Zeeman field composed of the homogeneous external field and a fluctuating local hyperfine field. A difference  $\Delta B_{nuc}^z$  between the  $z$ -components of the hyperfine fields in the two dots leads to an energy splitting between the basis states  $|\uparrow\downarrow\rangle$  and  $|\downarrow\uparrow\rangle$ . This splitting causes a precession between the  $S$  and the triplet  $T_0 \equiv (|\uparrow\downarrow\rangle + |\downarrow\uparrow\rangle)/\sqrt{2}$ , and its fluctuations dephase the qubit. At small negative detunings,  $\varepsilon \lesssim 0$ , inter-dot tunneling leads to an exchange splitting between  $S$  and

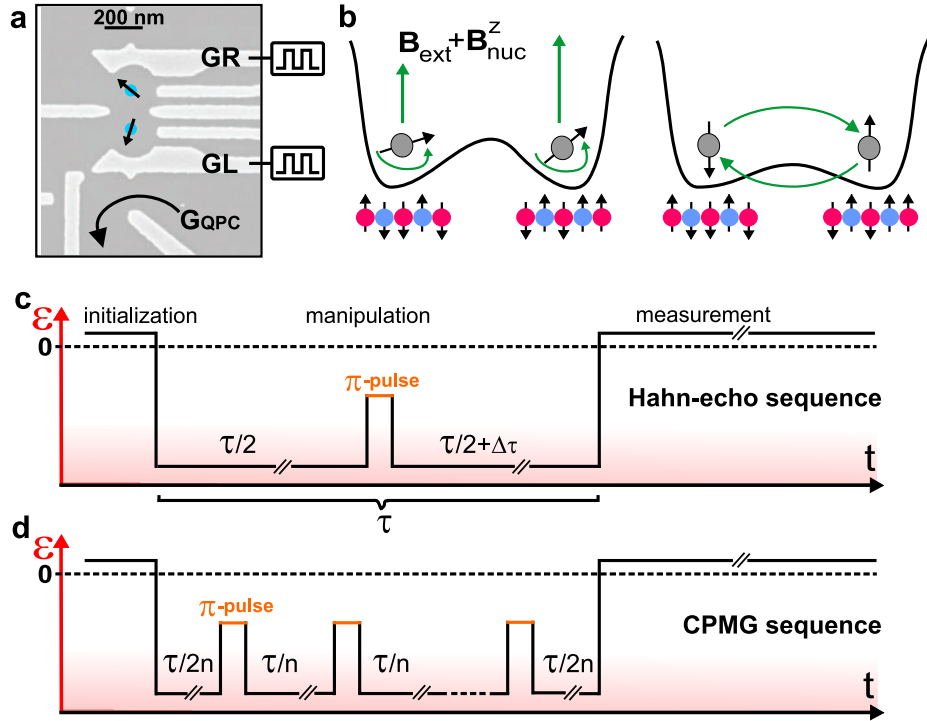


Figure 7.1: a) SEM micrograph of a device similar to the one used. Metal gates (bright structures) are negatively biased in order to confine two electrons. The charge state of the double quantum dot is determined by measuring the conductance through the capacitively coupled quantum point contact,  $G_{QPC}$ . The separation  $\varepsilon$  between the two electrons is controlled with nanosecond time resolution via the voltages on GR and GL. b) Left: an initially prepared singlet state oscillates between  $S$  and  $T_0$  at a rate given by  $g^*\mu_B\Delta B_{nuc}^z/\hbar$ , which changes over time due to slow fluctuations of the hyperfine field gradient  $\Delta B_{nuc}^z$ . Right: switching on the tunnel coupling between the two dots leads to the coherent exchange of the electron spins. c) Hahn-echo sequence: after evolving for a time  $\tau/2$ , the two electrons are exchanged with a  $\pi$ -pulse. The singlet state is recovered after further evolution for another  $\tau/2$ , i.e. for  $\Delta\tau = 0$ , for fluctuations of  $\Delta B_{nuc}^z$  slower than  $\tau$ . d) Carr-Purcell-Meiboom-Gill sequence: in this higher order decoupling sequence,  $n$   $\pi$ -pulses at time intervals  $\tau/n$  are applied.

$T_0$  that can be used to drive coherent oscillations between the states  $|\uparrow\downarrow\rangle$  and  $|\downarrow\uparrow\rangle$ . Instead of physically reversing the spins, a  $\pi$ -pulse that flips the state of the qubit is realized by swapping the electrons in the two dots with such an exchange operation. The pulse profiles for the Hahn-echo and CPMG sequence are shown in Fig. 7.1c,d.

Read-out of the final qubit state is accomplished by pulsing to positive detuning,  $\varepsilon > 0$ , where the state with both electrons sitting in the same dot is preferred for the spin singlet, but is energetically excluded for a spin-triplet due to the Pauli exclusion principle. The two spin states are thus transformed into different charge states. To sense this difference, we use a proximal quantum point contact (QPC), whose conductance depends on the local electrostatic environment [36]. After averaging over many identical pulse cycles, the mean QPC conductance,  $G_{QPC}$ , reflects the probability of finding the qubit in the singlet state at the end of each cycle. Fig. 7.2a shows the measured Hahn-echo signals for different external magnetic fields  $B_{ext}$ .

## 7.4 Hahn-echo measurements

### 7.4.1 Low magnetic field measurements

At low fields, we find periodic revivals of the echo signal at times inversely proportional to  $B_{ext}$ . These revivals were predicted in Refs. [14, 54] based on a quantum mechanical treatment of electron-mediated flip-flops between nuclei. We have reproduced this result within a semi-classical picture presented next. For a single spin, the level splitting between  $|\uparrow\rangle$  and  $|\downarrow\rangle$  is proportional to the total magnetic field  $B_{tot} = \sqrt{B_z^2 + B_\perp^2} \approx B_z + B_\perp^2/2B_z$ . The transverse hyperfine field  $B_\perp$  is a vector sum of contributions from the three nuclear species  $^{69}\text{Ga}$ ,  $^{71}\text{Ga}$  and  $^{75}\text{As}$ . Their different precession rates lead to harmonics in  $B_\perp^2(t)$  at

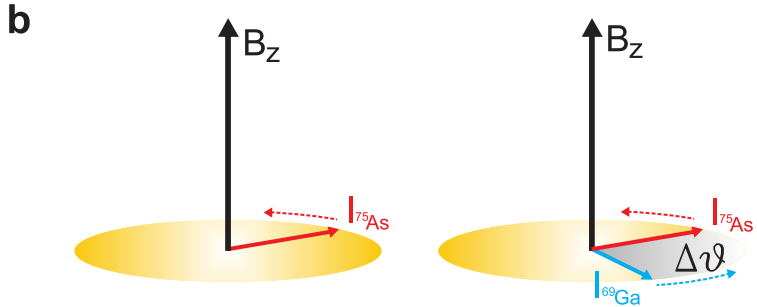
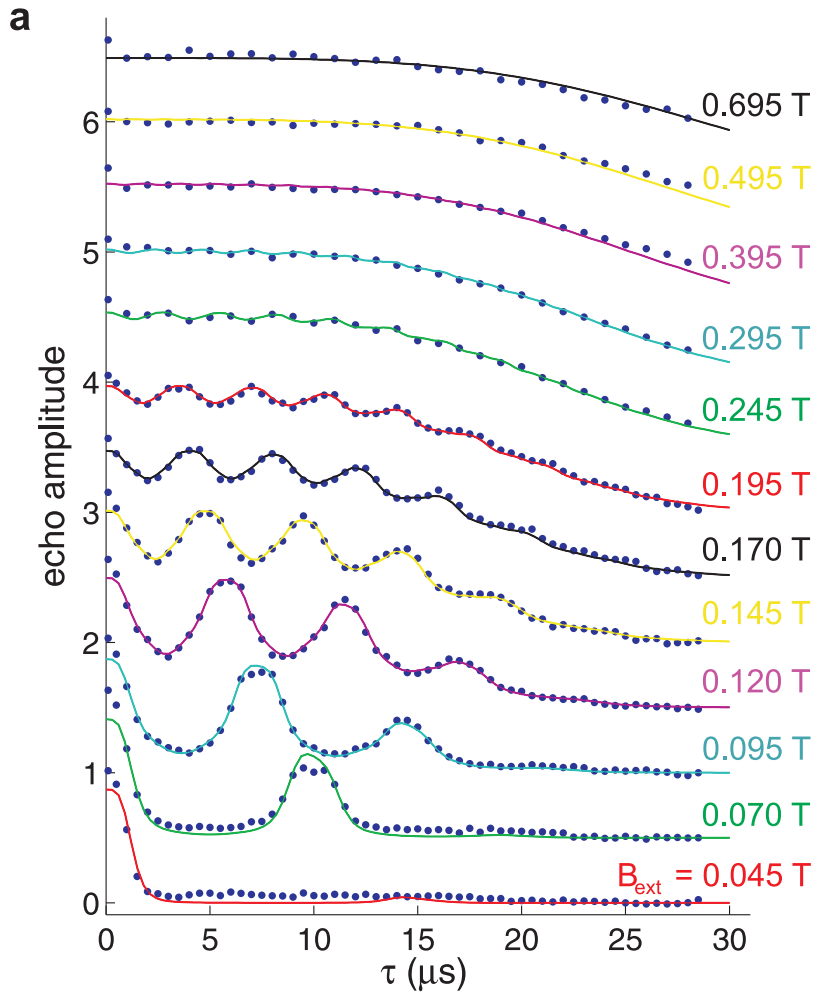


Figure 7.2: a) Echo signal as a function of the total evolution time,  $\tau$ , for different values of magnetic field. The fits to the data are obtained by extending the model of Ref. [14] to include a spread  $\delta B_{\text{loc}}$  of the nuclear Larmor frequencies and multiplying it with  $\exp\{(-\tau/T_{SD})^4\}$ . Curves are offset for clarity and normalized as discussed in Sec. 7.7. b) Illustration of the time dependence of the transverse nuclear field  $B_{\perp}^2$  for one (left side) or two nuclear species (right side) precessing with different Larmor frequencies (where the angle  $\Delta\theta$  varies as a function of time).

the three relative Larmor frequencies (Fig. 7.2 b).

If  $\tau/2$  is a multiple of all three relative Larmor periods, no net phase is accumulated by the electrons due to these oscillatory components. Non-oscillatory parts arising from single nuclear species are removed by the echo pulse. As a result, the echo amplitude shows a peak whenever the above mentioned commensurability condition is met. Otherwise, variations of the phase and magnitude of the oscillatory components over many runs randomize the electronic phase accumulated during an echo experiment. Ensemble averaging over these parameters exactly reproduces the results from Refs. [14, 54].

#### 7.4.2 High magnetic field measurements

At sufficiently high fields, the effect of the transverse hyperfine field is suppressed because  $B_z \approx B_{ext} \gg B_\perp$ . The echo decay is then expected to be dominated by fluctuations of  $B_z$  due to dipolar coupling between nuclei and predicted to be of the form  $\exp\{-(\tau/T_{SD})^4\}$  [86, 97]. Assuming statistical independence of the distributions of  $B_z$  and  $B_\perp$ , we have incorporated this decay into our model as a multiplicative factor.

#### 7.4.3 Fit to the data

The field dependence of the echo envelope decay can be accounted for by assuming a spread in the local fields determining the nuclear Larmor frequencies with a rms value of  $\delta B_{loc} = 0.3$  mT, which causes additional fluctuations of  $B_\perp$ . The measured NMR line width in pure GaAs is 0.1 mT [128]. A possible origin for the larger field inhomogeneity found here is the quadrupole splitting arising from the presence of the two localized electrons [129]. The inhomogeneity of the Knight shift has a similar but quantitatively negligible effect for our parameters.

Using the above described model, we fit all the data in Fig. 7.2 with a single set of field independent parameters  $N$ ,  $T_{SD}$  and  $\delta B_{loc}$ , which were chosen to obtain a good match with all datasets. We obtain the best fit for  $T_{SD} \approx 37 \mu\text{s}$ , which implies that  $\delta B_{loc}$  contributes significantly to the echo decay over the whole field range studied here.  $N$  is the number of nuclei coupled to each electron, which determines the depths of the dips between revivals. An independent determination of its value by measuring  $T_2^* = \sqrt{N}\hbar/g^*\mu_B \cdot 4.0 \text{ T}$  gives  $N = 4.9 \times 10^6$ , whereas the fits to the  $\tau$ -dependence in Fig. 7.2 yield  $N = 4.4 \times 10^6$ .  $T_{SD}$  is consistent with a theoretical estimate based on these numbers [86]. We have also verified that the Hahn-echo life time is not significantly affected by dynamic nuclear polarization, which can be used to increase  $T_2^*$  [100].

#### 7.4.4 Fit procedures

The fits in Fig. 7.2 were performed using the expression

$$\text{echo amplitude} = \frac{C}{\prod_j (1 + i\lambda_j)^2} e^{-(t/T_{SD})^4},$$

where  $\lambda_j$  are the eigenvalues of the  $T$  matrix from Ref. [14]. The square in the denominator accounts for the presence of two dots. We set the  $A_{kl}$  to zero and used a single  $A_k$  for each species. This approximation corresponds to neglecting the effect of the inhomogeneity of the hyperfine coupling, which can easily be taken into account, but only leads to negligible corrections for our parameters. We approximated the Gaussian distribution of  $\delta B_k$  with five discrete values. Using a finer discretization had no effect on the model. The prefactor  $C$  accounts for uncertainties in the data normalization discussed in Sec. 7.7, and the exponential models the additional dephasing due to spectral diffusion.

We first fit each dataset with several free parameters, some of which had to be kept fixed for some dataset because the fits would have been underdetermined otherwise. Based on

these initial fits, we corrected the external field by a 5 mT offset compared to the nominal value, which can be attributed to flux trapped in our superconducting magnet. From these preliminary fit parameters, we picked a single set of values and optimized it by hand to give a good overall fit to all datasets, allowing only the normalization constant  $C$  to vary independently at each field. Its values are  $C = 1.00 \pm 0.05$  except for the traces at 45, 70 and 95 mT, for which  $C \approx 0.90$ .

The physically relevant fit parameters are thus the number of nuclei per dot,  $N$ , the spectral diffusion decay time,  $T_{SD}$ , and the spread of the Larmor frequencies parametrized by  $\delta B$ .  $N$  determines the width of the revival peaks at low fields and the depth of the collapses at intermediate fields, whereas the other two parameters control the envelope decay. The best fits to the data shown in Fig. 7.2 were obtained with a  $N = 4.4 \cdot 10^6$ ,  $\delta B = 3 \cdot 10^{-4}$  T and  $T_{SD} = 37 \mu\text{s}$ .

## 7.5 Pulse design and optimization

In order to measure the long Hahn-echo decay times of up to  $30 \mu\text{s}$ , it was necessary to systematically optimize the pulses. Any difference in the gate voltage before and after the  $\pi$ -pulse shifts the electronic wave function, which leads to a change of the Overhauser field and thus an imperfect echo. We have minimized this effect by compensating for a systematic drift of  $\varepsilon$  over the course of each pulse sequence.

### 7.5.1 Pulse design

By modeling the bias lines as a lumped  $RC$  low pass filter with time constant  $\tau_{RC} \approx 25 \mu\text{s}$ , one needs to supply a voltage  $V(t) + \delta V(t)$  where  $V(t)$  is the desired signal at the gates and  $\delta V(t) = \int_0^t dt' V(t')/\tau_{RC}$  is a correction required to compensate for the finite charging time

of the filter.

The  $RC$  behavior reflects the relatively high and frequency dependent impedance of the twisted DC lines: our home made bias tees do not appear to degrade the pulse rise time, which is limited to about 2 ns by the waveform generator bandwidth and coax cables attenuation.

In many experiments, the largest fraction of a pulse cycle is spent at the measurement point. In this case, it is adequate to only apply the small corrections for the short initialization and manipulation pulses away from the measurement point according to the above shown model. As the manipulation times become comparable to  $\tau_{RC}$  and to the measurement time, larger compensations  $\delta V(t)$  have to be applied, making the manipulation more susceptible to errors.

For the very long evolution times used for the presented measurements, it is convenient

- 1) to have zero voltage of the fast pulse line at the fully separated (1,1) configuration and
- 2) to add a pulse that is approximately the opposite of the (in our case 10  $\mu\text{s}$  long) read-out pulse after the read-out stage to discharge the DC lines stray capacitance. As a result, only very small corrections are necessary during the manipulation stage, thus reducing the sensitivity to an imperfect compensation. For most measurements discussed, we used a pulse period of 50  $\mu\text{s}$ , which allows evolution times  $\tau$  of up to about 29  $\mu\text{s}$ . For the CPMG measurements of Fig. 7.5, the pulse period was 250  $\mu\text{s}$ .

We monitored the conductance of our QPC using an RF reflectometry technique presented in Chap. 4. Besides providing a large sensitivity and bandwidth, this allows activating the 230 MHz QPC excitation only during the read-out stage of each pulse cycle, which avoids a read-out related perturbation of the qubit in the manipulation stage. Furthermore, we recorded only the charge signal during the read-out stage rather than averaging over the

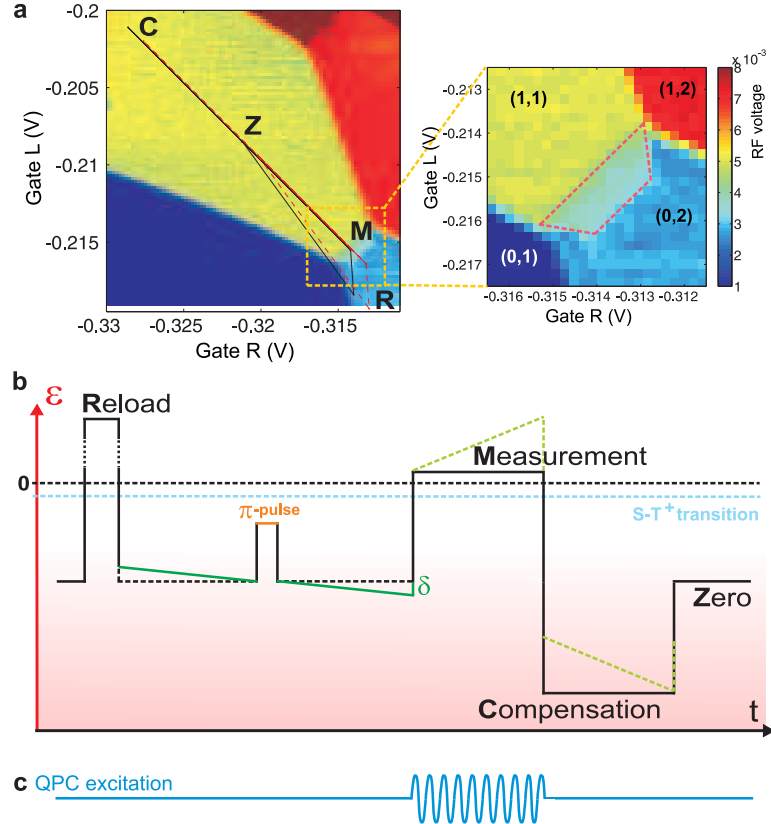


Figure 7.3: a) Scan of the QPC conductance as a function of Gates L and R. Each region corresponds to a different electron occupation number as indicated in the zoomed in plot on the right. The trapezoid in the top plot indicates the region where the (1,1) triplet state is metastable and spin-to-charge conversion is possible. The contrast in this region is the result of running a pulse that generates a mixed electronic state (see Chap. 2). The solid line in the left plot shows the trajectory of the Hahn-echo pulses in gate voltage. The dashed line represents the same pulse, but shifted such that the measurement point is outside the read-out region, thus enabling a background measurement. b) Schematic of the time dependence of the detuning  $\epsilon$  over a single Hahn-echo pulse cycle. The letters in panel a) indicate the positions of the pulse stages. The continuous green line with slope proportional to  $\delta$  shows the correction applied in order to compensate for pulse imperfections (see Sec. 7.5.2). The dashed lines show the modification of the pulse applied to compensate for the high pass filtering by the bias tees. We applied this correction to the whole pulse, but only show its effect for the read-out stage for clarity. c) The 230 MHz QPC excitation was only switched on during the measurement stage, thus avoiding backaction during the evolution stage.

whole pulse period, thus largely eliminating undesired background signals and excess noise.

### 7.5.2 Pulse optimization

Even after adjusting for the finite  $\tau_{RC}$ , Hahn-echo pulses typically do not yet show the results of Fig. 7.2 for  $\tau$  larger than a few  $\mu\text{s}$ . Relatively rapid measurements of the  $\Delta\tau$  dependence (50 data points/s) show fluctuations of the position of the maximum of the echo amplitude on a time scale typical for the nuclear hyperfine field fluctuations (see Fig. 7.4a). We attribute these fluctuations to shifts of the electronic wave function  $\psi$  in response to a drift of the gate voltages over each pulse cycle. Such a shift modifies the hyperfine coupling strength to each individual nucleus, which is proportional to  $|\psi|^2$  at the site of the nucleus. If the voltage drift is not symmetric about the  $\pi$ -pulse, the electrons will accumulate a net phase shift (depending on the nuclear state), and the echo maximum occurs at nonzero  $\Delta\tau$ . In other words, the refocusing effect of the Hahn-echo sequence is incomplete resulting in a systematic underestimate of  $T_2$ .

We found that this effect can be largely eliminated by adding a second compensation to the pulses along the  $\varepsilon$  axis. We have chosen a linear form for this correction, see Fig. 7.3b, but we believe that only the mean of the shift over each evolution interval is important.

The amplitude  $\delta$  of the compensation is iteratively optimized for each mixing time by measuring the echo amplitude at three values of  $\delta$ : one value is the best guess chosen by quadratic interpolation based on the results of the previous run and the other two are equally distant on each side of the interpolating line, see Fig. 7.4. Points at short  $\tau$  are excluded from the interpolation. Once implemented, this procedure converged within no more than 10 runs, each of which required about 30 min of averaging. Figs. 7.4c and d show the  $\delta$ -values used for the last iteration and the resulting echo amplitudes as a function of

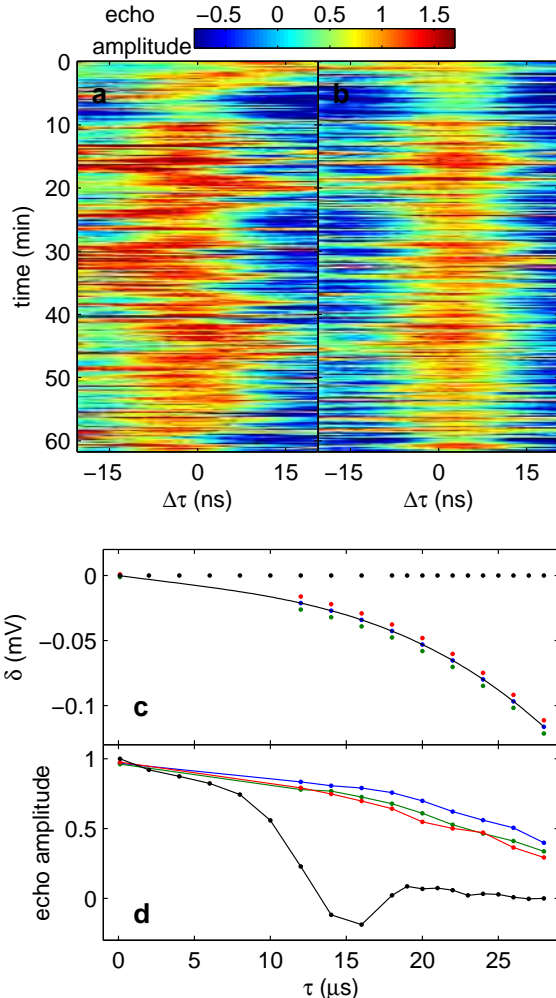


Figure 7.4: Repeated measurements of the echo signal as a function of  $\Delta\tau$  at  $B_{ext} = 0.7$  T,  $\tau = 5.4 \mu s$  with unoptimized a) and optimized b) pulses. For unoptimized pulses, the position of the maximum of the echo signal fluctuates on a timescale typical for nuclear fluctuations. After optimization, only the width of the maximum fluctuates. Without correction, the mean echo amplitude is reduced. The scaling of the data is the same in panels a)-b) and was set by hand. The asymmetry of the curve is due to a measurement background and/or a nonzero mean of the  $\Delta\tau$  maximizing the echo amplitude. c) Correction parameter  $\delta$  (see Fig. 7.3) at (blue) and near (red, green) the optimum. The black line is the cubic fit used to interpolate the correction parameter. d) Echo amplitude for  $\Delta\tau = 0$  for the parameters in panel e) and without any optimization ( $\delta = 0$ , black).

$\tau$ , a dramatical improvement compared to the unoptimized pulses. Note in Fig. 7.4d that our best guess of  $\delta$  corresponds to a local maximum of the echo amplitude. Attempts to introduce additional corrections, for example orthogonal to the  $\varepsilon$  axis or by applying pulses to other gates, led to no further improvements.

## 7.6 CPMG pulses

A better estimate of  $T_2$  is expected for more elaborate decoupling sequences [127]. We implemented the CPMG sequence [62], which consists of an  $n$ -fold repetition of the Hahn-echo, thus requiring  $n \pi$ -pulses, as shown in Fig. 7.1d. Fig. 7.5 shows data for  $n = 6, 10$  and  $16$ . For  $n = 16$ , the echo signal clearly persists for more than  $200 \mu\text{s}$ .

The linear decay of the signal in Fig. 7.5 is not well understood. The similar variation of the reference signal corresponding to a completely mixed state is suggestive of a single-electron  $T_1$  process causing leakage into the  $T_+$  and  $T_-$  states. The decay time constant is on the order of  $300 \mu\text{s}$ , and sets a lower bound for the largest achievable coherence time.

Because of the large number of potential tuning parameters, we have not optimized these CPMG pulses. Imperfect pulses are likely to limit the coherence time observed in Figs. 7.5a and b, and are responsible for the bump around  $\tau = 180 \mu\text{s}$  in Fig. 7.5 b. As we decrease the interval between  $\pi$ -pulses, these errors seem to be mostly eliminated, although we cannot rule out that they contribute to the linear reduction of the echo signal in Fig. 7.5. We expect that with improved pulses, the same extension of the coherence time could be achieved with fewer pulses.

Note that the multiple  $\pi$ -pulse sequence is equivalent to the CPMG sequence rather than the Carr-Purcell sequence even though we do not use a  $\pi/2$  pulse around the  $y$ -axis of the Bloch sphere for preparation. Instead, we rapidly switch off the exchange splitting  $J$ ,

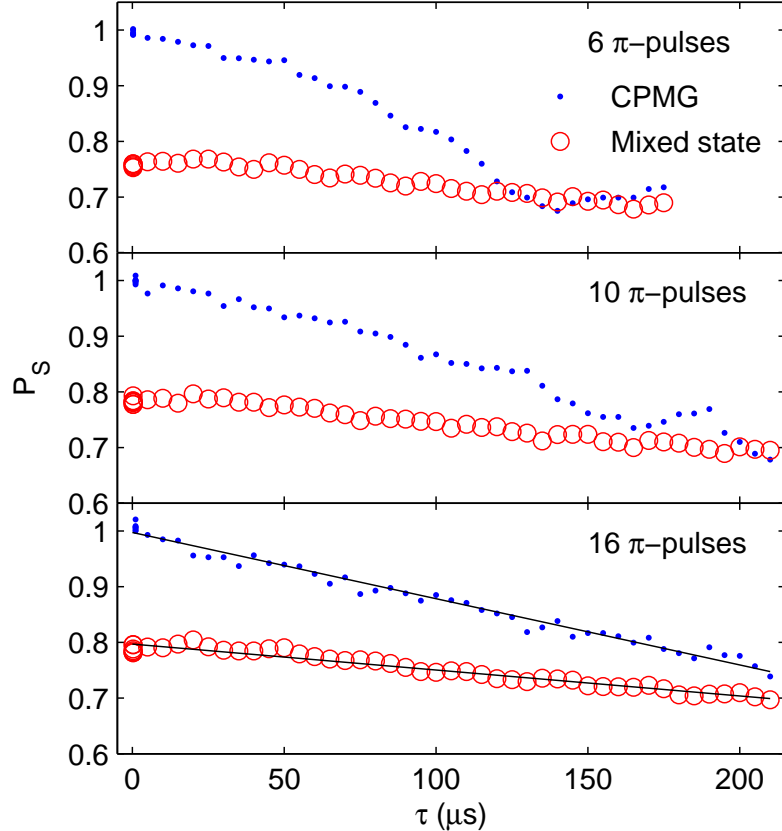


Figure 7.5: CPMG decoupling experiments with 6, 10 and 16  $\pi$ -pulses at  $B_{ext} = 0.4$  T. The blue dots show the read-out signal of the CPMG pulses, the red circles represent reference measurements with the same evolution time without any  $\pi$ -pulses (equivalent to  $T_2^*$  measurements), which produce a completely dephased state.  $P_S$  is the sensor signal normalized by the DC contrast of the (1,1) and (0,2) charge states, so that a singlet corresponds to  $P_S = 1\text{xs}$ . Inelastic decay during the read-out phase and possibly other visibility loss mechanisms increase  $P_S$  for the mixed state above the ideal value of 0.5. The linear trends in the reference and the initial decay of the CPMG signal likely reflect leakage out of the logical subspace. The linear fits to the 16-pulse data (black lines) intersect at  $\tau = 276 \mu\text{s}$ , which can be taken as a lower bound of the coherence time.

which prepares an initial state on the axis round which the exchange  $\pi$ -pulses rotate. This state is the same as the one obtained by applying a  $\pi/2$  pulse around the orthogonal  $y$ -axis after preparing a ground state  $|\uparrow\downarrow\rangle$  or  $|\downarrow\uparrow\rangle$ , as in the original CPMG sequence.

## 7.7 Normalization and background measurements

Since the QPC conductance not only depends on the electron configuration of the adjacent double dot, but also on the pulsed gate voltages, an absolute measurement of the (average) electronic state generally requires some calibration. Here, we have taken reference measurements by omitting all  $\pi$ -pulses from the Hahn-echo or CPMG sequences. The resulting pulses correspond to a  $T_2^*$  measurement which, for mixing times  $\tau$  above a few tens of nanoseconds, should produce a completely dephased state. Furthermore, we measured the response to each pulse at a point of larger detuning  $\varepsilon$ , where the (0,2) triplet state has a lower energy than the (1,1) triplet so that either spin state leads to a (0,2) charge signal.

Fig. 7.6a shows all four measurements for a typical Hahn-echo measurement as a function of  $\tau$ . The overall background common to all these measurements is due to direct coupling of the gate pulses to the QPC. Ideally, all pulses have the same gate voltage in the read-out phase but we experimentally notice a small variation of the read-out signal background for different  $\tau$ . The voltage shift causing this variation is as small as 0.2 % of the voltage jump between the working point in (1,1) and the measurement point in (0,2).

The differences between various combinations of these pulses are shown in Fig. 7.6b. From the small difference between the echo and reference pulses when outside the measurement region, we conclude that the change of the direct coupling due to the omission of the  $\pi$ -pulses has a negligible effect. Therefore subtracting the signals from identical pulses at different operating points should yield the electronic contribution (whether singlet or

triplet) at the working point, plus a constant offset due to the different DC gate voltages. For the range of  $\tau$  in Fig. 7.6, the mixed state shows a flat response, as expected. It thus provides a useful reference for the echo measurements - the echo amplitude is proportional to the difference between the signals of the measurement and corresponding reference pulse. This background measurement and subtraction procedure was applied to most data shown here. An exception are the curves for  $B_{ext} < 0.2$  T, where we took no (simultaneous) reference measurement in order to measure with a higher  $\tau$  resolution without exceeding the memory limitation of our waveform generator. Instead, we used the last few data points as a reference and checked the consistency of the two procedures by repeating the measurements at a lower resolution, but with a reference. Having thus established the signal level corresponding to a fully dephased state, we still need to determine a proportionality factor. In principle, this could be determined from the height of the (1,1) - (0,2) transition, measured by sweeping the DC gate voltages. However, the actual signal is usually smaller due to inelastic decay of the metastable (1,1) triplet state at the measurement point and possibly other preparation and read-out imperfections. While these effects could in principle be eliminated or characterized, we decided to normalized all datasets by the echo amplitude obtained for short  $\tau$ , excluding the first data point. This normalization also hides contrast losses due to systematic errors in the  $\pi$ -pulses, which would only lead to an overall contrast loss as long as they are independent of the evolution times between the  $\pi$ -pulses.

On the much longer time scale of the CPMG measurements shown in Fig. 7.5, we find a linear trend in both the reference and CPMG data. It appears to increases with larger  $B_{ext}$  and also becomes visible for short  $\tau$  at magnetic fields above 0.4 - 0.7 T. A possible explanation for this trend is a single spin  $T_1$  process, which would cause leakage into the  $T_+$  and  $T_-$  states and increase the triplet probability for longer  $\tau$ . Such a  $T_1$  process can be

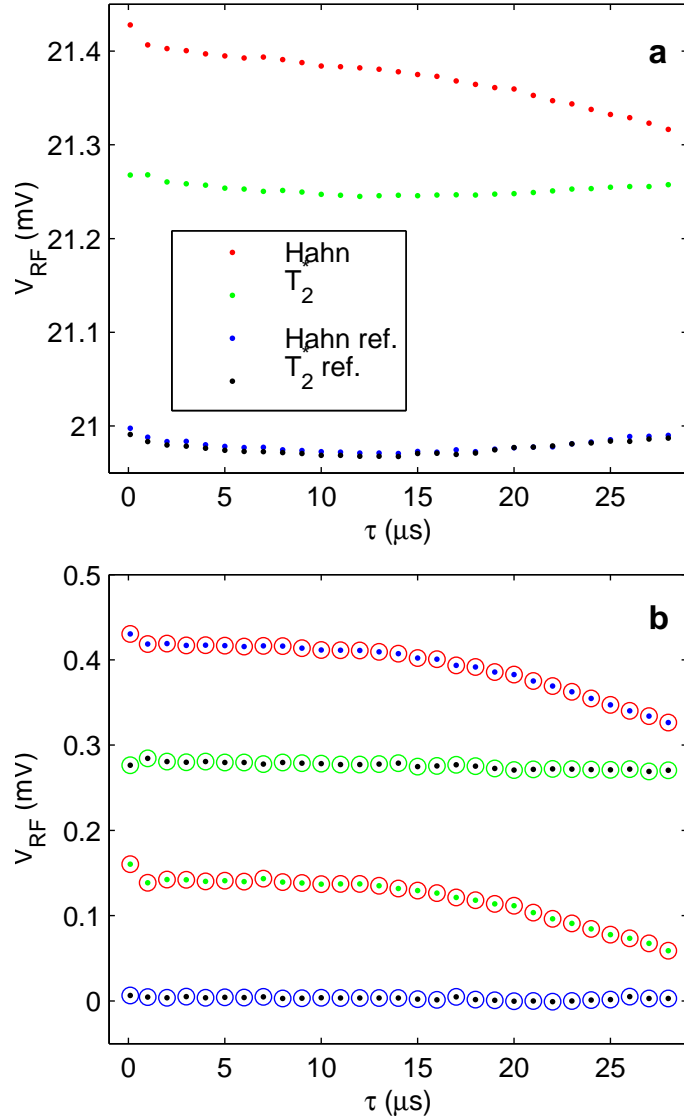


Figure 7.6: a) Raw data for the 0.4 T Hahn-echo measurement of Fig. 7.2. The  $T_2^*$  pulses are identical to the Hahn-echo pulses except for the omission of any  $\pi$ -pulses and produce a completely dephased state for the long  $\tau$  used here. The two reference measurements were taken with the same pulses, but at a working point where both singlets and triplets lead to a (0,2) charge signal. b) Differences between various pairs of curves from panel a). The colors of the circles and dots indicate the curves that were subtracted. The red/green combination corresponds to the subtraction used in Fig. 7.2 and most other  $\tau$ -dependence measurements.

expected to be exponential and thus would be consistent with a linear initial decay. To avoid ambiguities due to this poorly understood background, we only subtracted a measurement at the large- $\varepsilon$  working point and normalized by the DC charge transition to generate the plots of  $P_S$  in Fig. 7.5. The overall offset was chosen so that small  $\tau$  give a singlet probability  $P_S = 1$ . In the absence of inelastic decay and other effects discussed above, this procedure would lead to  $P_S = 0.5$  for the mixed state.

## 7.8 Conclusions

Our measurements demonstrate coherence times of GaAs spin qubits of at least  $200\ \mu\text{s}$ , two orders of magnitude larger than previously shown. The duration of each of the  $\pi$ -pulses could easily be reduced below the 6 ns used here. Thus, more than  $10^5$  operations could be carried out within the coherence time, well in excess of the commonly quoted error correction threshold of  $\sim 10^4$ . Furthermore, one may hope to achieve millisecond scale coherence times with improved decoupling sequences [127] without adding complexity. While we have greatly extended the memory time of our qubit, more effort is required to find pulse sequences that achieve high fidelities for short, nontrivial operations [130, 118]. The excellent agreement with the model for the field and time dependence of the echo revivals shows that many aspects of the dephasing of electron spins due to the nuclear hyperfine interaction are now well understood. The insight gained may also level the way towards probing macroscopic quantum effects in a mesoscopic ensemble of a few million nuclear spins.

## Chapter 8

# Observation of dynamic nuclear polarization using a single pair of electrons

Sandra Foletti<sup>1</sup>, Jens Martin<sup>1</sup>, Merav Dolev<sup>2</sup>, Diana Mahalu<sup>2</sup>, Vladimir Umansky<sup>2</sup> and Amir Yacoby<sup>1</sup>

1. Department of Physics, Harvard University, Cambridge, MA 02138, USA  
2. Braun Center for Submicron Research, Department of Condensed Matter Physics,  
Weizmann Institute of Science, Rehovot 76100, Israel

We study dynamic nuclear polarization in a GaAs double dot system containing two electrons that are never exchanged with the reservoir. By periodically driving the system towards the singlet and triplet  $T_+$  degeneracy point, excess polarization is built up. The pumping procedure is observed to be most effective when the duty cycle equals a multiple of the Larmor precession time of the Ga and As nuclei. The induced polarization corresponds to cooling of the underlying nuclear system. The dependence on the dwell time at the mixing

point is found to be non-monotonic. We interpret this effect arising from the coherent interplay between hyperfine coupling and electron spin orbit coupling<sup>1</sup>.

## 8.1 Introduction

Single electron spins in a solid state environment constitute a promising candidate for storing and manipulating quantum information [12]. Recent experiments in few electron quantum dots in GaAs have demonstrated that both spin and charge can be manipulated electrostatically with electron spin coherence times in excess of a few microseconds [51, 95]. While the measured spin coherence time  $T_2$  is much longer than the time it takes to perform a single quantum operation, the inhomogeneous spin relaxation time  $T_2^*$  is short and exceeds the time required for gate operations only by approximately one to two orders of magnitude [13, 121]. We have recently shown that nuclear spins in GaAs double quantum dots can be used to enable full quantum control of the two-electron spin qubit by pumping and controlling the local difference in nuclear magnetic fields between the two dots (see Chap. 5), thereby turning to our advantage what was considered an obstacle [59, 132, 133, 86, 46] to the achievement of a large number of coherent manipulations. Little attention however has been paid so far to the coherent dynamics of the nuclear spin bath: understanding them is of major importance in the field of solid state quantum computation [107, 82, 113, 134, 135, 136].

We first consider a simple model to explain dynamic nuclear polarization: at finite magnetic field the double dot two-electron spin states singlet  $S$  and triplet  $T_+$  cross at a well defined gate voltage setting, and mix due only to the presence of hyperfine coupling. Dynamic nuclear polarization is achieved by repeatedly driving the two electrons from  $S$

---

<sup>1</sup>This chapter is adapted from Ref. [131].

to  $T_+$ . In this limit the conservation of angular momentum necessitates a spin flip in the nuclear sub system thereby producing a single nuclear spin flip per cycle. As the sequence is repeated over a large number of cycles, nuclear polarizations slightly larger than 1-5 % have been achieved [49, 81].

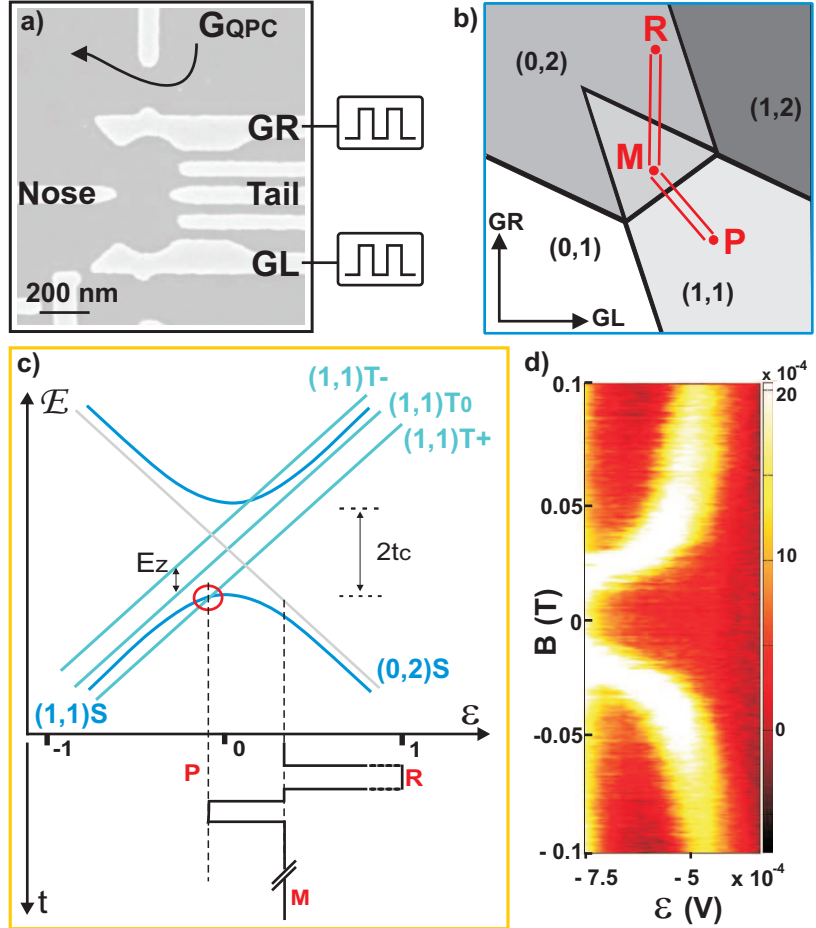


Figure 8.1: a) SEM micrograph of the device. GL and GR control the energy detuning,  $\epsilon$ , related to the equilibrium occupation of the dot, while gates Nose and Tail allow to change the interdot tunnel coupling. The average occupation of the dot is sensed by the nearby quantum point contact as a variation of its conductance. b) Pulse sequence shown within the double dot charge stability diagram. R indicates the reload point, M the measurement point and P the probing point. c) Relevant energy levels at the  $(0,2)$ - $(1,1)$  charge transition as a function of detuning. The  $S-T_+$  crossing point is marked by a red circle. The pulse sequence sketched as a function of detuning and time is used to measure the position of the  $S-T_+$  transition as a function of magnetic field. d) Measurement of the position of the  $S-T_+$  transition as a function of detuning  $\epsilon$  and external magnetic field  $B_{ext}$ .

In Petta *et al.* and in Chap. 5 discarding the two electrons and reloading the system

into a singlet state after each pump cycle is essential for building up polarization. If the two electrons are never exchanged with the reservoir, one expects that the two electron system is periodically driven from the  $S$  to the  $T_+$  state approximately half of the pump cycles, while during the other half, transition from  $T_+$  to  $S$  occur.

In this Chapter, we show that nuclear polarization can be induced with a single pair of electrons, in contrast with the argument outlined above. Moreover we find that the pumping cycle works most effectively when the duty cycle of the polarization pulse equals a multiple of the nuclear Larmor precession time. Under these conditions cooling of the nuclear subsystem is observed.

As shown by Rudner *et al.* [137], effects of this type can arise from a coherent interplay between electron-nuclear hyperfine coupling and electron spin-orbit coupling. The spin-orbit interaction selects a particular direction in the  $xy$ -plane relative to which the absolute phase of the nuclear precession can be measured. Due to this coupling, the electron spin maintains a non-zero average transverse projection, which drives nuclear polarization via the Knight field. The effect is sensitive to the phase of the transverse nuclear polarization and thus can be modulated by the nuclear Larmor precession. Our observation of modulations of the nuclear spin pumping efficiency controlled by the nuclear Larmor precession period indicated that we are now in a position to explore this new and interesting regime.

## 8.2 Description of the system

Our measurements are conducted on a GaAs double dot system that is tuned to contain only two electrons. We restrict the phase space to two charge configurations: two electrons in one dot (schematically represented as (0,2)) and one electron in each dot (represented as (1,1)). The double quantum dot (dQD) is created using e-beam patterned PdAu gates that

are evaporated on the surface of a GaAs/AlGaAs heterostructure containing a 2 dimensional electron gas (2DEG) situated 91 nm below the surface with density=  $1.3 \cdot 10^{15} \text{ m}^{-2}$  and mobility=  $4.9 \cdot 10^6 \text{ cm}^2/\text{V}\cdot\text{s}$ . Gate R (GR) and gate L (GL) control the number of electrons in the right and left dot respectively while gates Nose and Tail allow for an independent control of the tunnel coupling ( $t_c$ ) between the dots (see Fig. 8.1a). Both GR and GL are connected via attenuated coaxial cables to a Tektronix AWG520 arbitrary waveform generator (with a rise time of 1.5 ns) that allows fast pulsing of these gates.

The nearby quantum point contact (QPC) allows the measurement of the double dot charge configurations [36]. We tune the QPC conductance to about  $0.8e^2/h$ , where it is most sensitive to changes of the surrounding electrostatic potentials. A change of the dot's average occupancy is reflected in a change of the QPC conductance. This is measured in a current bias scheme (5 nA excitation) with standard lock-in technique at a frequency of 137 Hz and 300 ms time constant. The device is placed in a dilution refrigerator with  $T_{base} = 10 \text{ mK}$  and  $T_e = 100 \text{ mK}$  established by measuring the width of Coulomb blockade peaks. An external magnetic field of  $\lesssim 150 \text{ mT}$  is applied perpendicular to the 2DEG.

Measurements presented here focus on the (0,2)-(1,1) charge transition. A particular combination of the voltage applied to gates GL and GR, denoted here by  $\epsilon$ , allows continuous detuning from one charge configuration to the other. In the absence of spin dependent terms, the ground state in all possible charge configurations is the singlet state. A weak external magnetic field induces a splitting of the three triplet,  $T_-$ ,  $T_0$  and  $T_+$ . While in the (0,2) charge configuration the triplet states are separated from the ground state by a large singlet-triplet energy, in the (1,1) configuration the Zeeman energy lowers the  $T_+$  state below that of the singlet, as shown in Fig. 8.1c. A degeneracy point between  $S$  and  $T_+$ , marked by the red circle, is thereby generated at a particular value of  $\epsilon$  that depends on the Zeeman

energy.

It is important to notice that the total magnetic field entering the Zeeman energy is  $\mathbf{B}_{\text{tot}} = \mathbf{B}_{\text{ext}} + \mathbf{B}_{\text{nuclei}}$ .  $\mathbf{B}_{\text{nuclei}}$  is a linear combination of the left and right dots nuclear fields,  $\mathbf{B}_{\text{nuc},\mathbf{R}}$  and  $\mathbf{B}_{\text{nuc},\mathbf{L}}$ , with a weight that is proportional to the occupation of the two dots.

### 8.3 Measurement of the $S-T_+$ degeneracy point

The measurement of the  $S-T_+$  degeneracy point is done using the pulse sequence presented in Fig. 8.1b and c. The cycle begins by loading two electrons into the (0,2) singlet state (at point **R**). The loading procedure requires typically 200 ns. Then  $\epsilon$  is moved adiabatically with respect to the tunnel coupling ( $t_{\text{tunneling}} = \hbar/t_c \approx 0.1$  ns) to point **P** where the  $S-T_+$  transition is probed for  $t_P = 100$  ns. When point **P** coincides with the  $S-T_+$  degeneracy point a transition from the singlet into the  $T_+$  state may occur together with a nuclear spin flip. The typical time for a  $S-T_+$  transition is approximately  $t_{\text{mixing}} \approx 10$  ns [95].

The system is then brought back to the measurement point **M** for the read-out of the final state  $|f\rangle$ . Since the tunneling between the two charge configurations conserves spin there are two possible outcomes: if  $|f\rangle$  is a singlet the transition to (0,2)S is allowed and the QPC detects two electrons in dot R. If  $|f\rangle$  is the triplet  $T_+$  state, it will be blocked in (1,1) $T_+$  since (0,2) $T_+$  is energetically not allowed and the QPC detects only one electron in dot R. This behavior is coined spin-blockade [138, 139] and occurs in the triangular region in Fig. 8.1b. A similar *spin to charge* conversion technique has been previously employed [140, 33]. After the measurement stage the system is reinitialized at point R and the cycle repeats itself. The measured signal at the QPC is a time-averaged measurement of the dot occupation throughout the entire cycle. Since  $t_M > 90\%$  of the total pulse time (here  $t_M = 10 - 20\ \mu\text{s}$ ) we primarily obtain information on the charge state at point M.

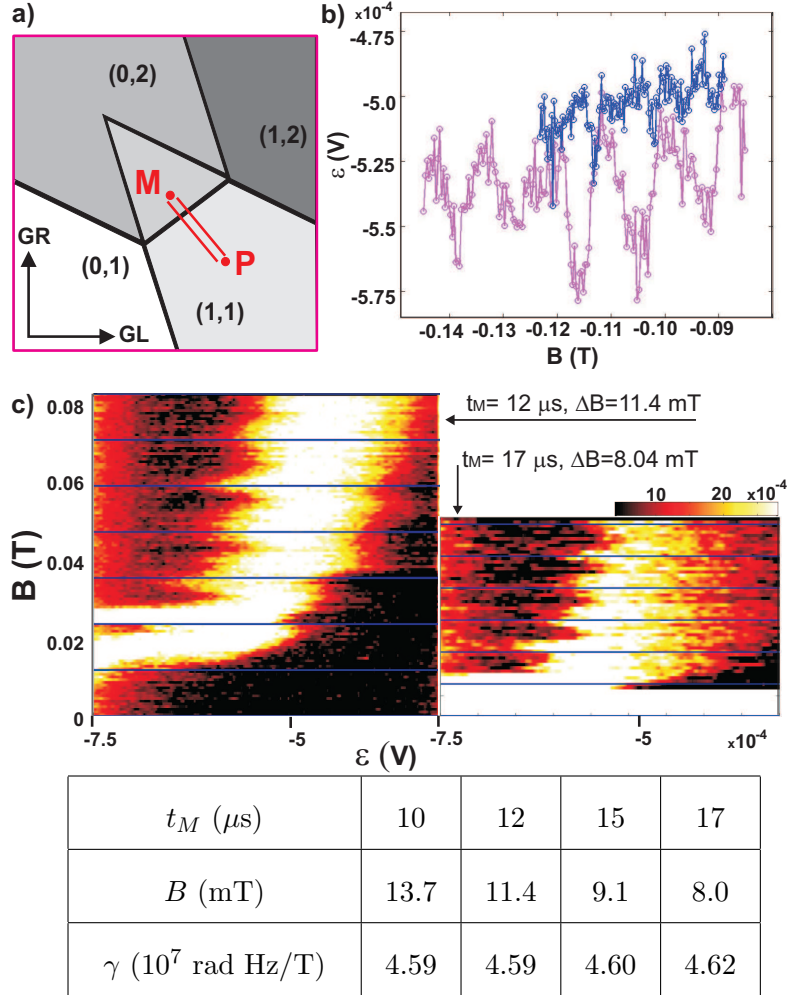


Figure 8.2: a) New pulse sequence used to measure the position of the  $S$  to  $T_+$  transition when the reload part is left out. In order to probe the  $S$ - $T_+$  transition the system is moved to point **P** for a typical time  $t_P=100$  ns, then it is brought back to the measurement position **M** for a time  $t_M = 10 - 20 \mu\text{s} > 90\%$  of the total pulse time. b) Measurement of the position of the  $S$ - $T_+$  transition as a function of magnetic field taken with two different pulse sequences: one including a reload part (blue line) and one without reload part (magenta line). c) Measurements of  $S$ - $T_+$  transition taken with two different measurement times. The periodicity in magnetic field shows  $\Delta B = 11.4 \text{ mT}$  for  $t_M = 12 \mu\text{s}$  and  $\Delta B = 8 \text{ mT}$  for  $t_M = 17 \mu\text{s}$ . The blue lines are a guide to the eye helping to compare periodicities.

Fig.8.1d shows a measurement of the position of the  $S$ - $T_+$  transition as a function of  $\epsilon$  and  $B_{ext}$ . The plotted QPC conductance reflects the return probability as a singlet. Dark regions indicate that no mixing occurred and the system remained in a singlet state. The bright funnel shaped feature maps the position of the  $S$ - $T_+$  transition as a function of  $B_{ext}$

and  $\epsilon$  reflecting a finite probability of being blocked in  $T_+$ .

## 8.4 Dynamic nuclear polarization using a single pair of electrons

What happens if we leave out the reload part from the pulse sequence? Now one must account for the history in order to know the initial state of each cycle. However, given that the relaxation time between the triplet and singlet states (of the order of ms) is shorter than our averaging time (300 ms), when the detuning is away from the  $S-T_+$  degeneracy point the system will relax to the singlet (0,2) state and remain there [33]. Hence, only when the detuning is at the  $S-T_+$  degeneracy point there will be a finite probability to observe a (1,1) charge state. Therefore a funnel similar to the case with reload should be observed.

We record an oscillatory behaviour of the  $S-T_+$  transition as a function of  $B_{ext}$ . In Fig. 8.2b we plot the values of  $B_{ext}$  and  $\epsilon$  delimiting the left-most side of the  $S-T_+$  transition as determined from the QPC conductance plots (see Fig. 8.1d and Fig. 8.2c) in the presence and absence of reload. Whereas the measurement with repeated reload (blue line) shows no magnetic field dependence, in the measurement without reload (magenta line) the position of the  $S-T_+$  transition dips below the blue line at periodic values in  $B_{ext}$ . The dips show that the  $S-T_+$  transition shifts towards more negative values of  $\epsilon$ . From the energy diagram in Fig. 8.1c we see that this corresponds to a decrease of the Zeeman energy, happening when  $\mathbf{B}_{tot} = \mathbf{B}_{ext} + \mathbf{B}_{HF}$  decreases. For a fixed  $\mathbf{B}_{ext}$ , blue points and magenta points are positioned at different values of  $\epsilon$ , meaning that  $\mathbf{B}_{HF}$  changed. The measured change in  $\mathbf{B}_{HF}$  is opposite the external magnetic field, thus an accumulation of nuclei with spin up has been created. Such population corresponds to cooling the nuclei.

The shift of the funnel to more negative detuning can be quantitatively translated to a change in total field using the local slope of the bare funnel (with reload shown in Fig. 8.1d) at the measurement field. The shift in detuning is translated to approximately 30-50 mT, which corresponds to 1 % of the total nuclear polarization [45].

In order to build up such nuclear polarization we need to repeat the pulse cycle at the  $S-T_+$  degeneracy point for a few minutes. When measuring the decay time of the created polarization we observe its full decay after about 15 minutes. The pulses are switched off during this time and just briefly turned on at the end in order to measure the actual position of the  $S-T_+$  transition.

#### 8.4.1 Total measurement time dependence

We also analyze the dependence of the oscillatory behaviour as a function of the measurement time  $t_M = 10 - 17 \mu\text{s}$  and the probing time  $t_P = 100 - 300 \text{ ns}$ ,  $t_M + t_P$  being the total pulse duration. The two scans in Fig. 8.2c show the period of the oscillations in magnetic field  $\Delta B(t_M)$  for two different measurement times  $t_M = 12 \mu\text{s}$  and  $t_M = 17 \mu\text{s}$ , while  $t_P = 200 \text{ ns}$  is kept fixed. We measure  $\Delta B$  for four different values of  $t_M$ , and find that the gyromagnetic factor  $\gamma = 2\pi/(\Delta B \cdot t_M)$  is constant and equals  $\gamma = 4.6 \cdot 10^7 \text{ rad Hz/T}$ , consistent with the gyromagnetic factor tabulated for  $^{75}\text{As}$  [65]. To further confirm this fact, we measured a portion of the funnel with higher trace resolution (see Fig. 8.3a): the whole scan of four oscillations takes about 24 hours.

Fourier analysis, Fig. 8.3b, clearly shows a peak at the Larmor frequency of  $^{75}\text{As}$ . Furthermore, the characteristic frequency of  $^{69}\text{Ga}$  is also visible. Its other isotope  $^{71}\text{Ga}$  is however hidden by the large second harmonic of  $^{75}\text{As}$ , because of the low resolution in Fourier space. We note that the intensities of the peaks corresponding to the different

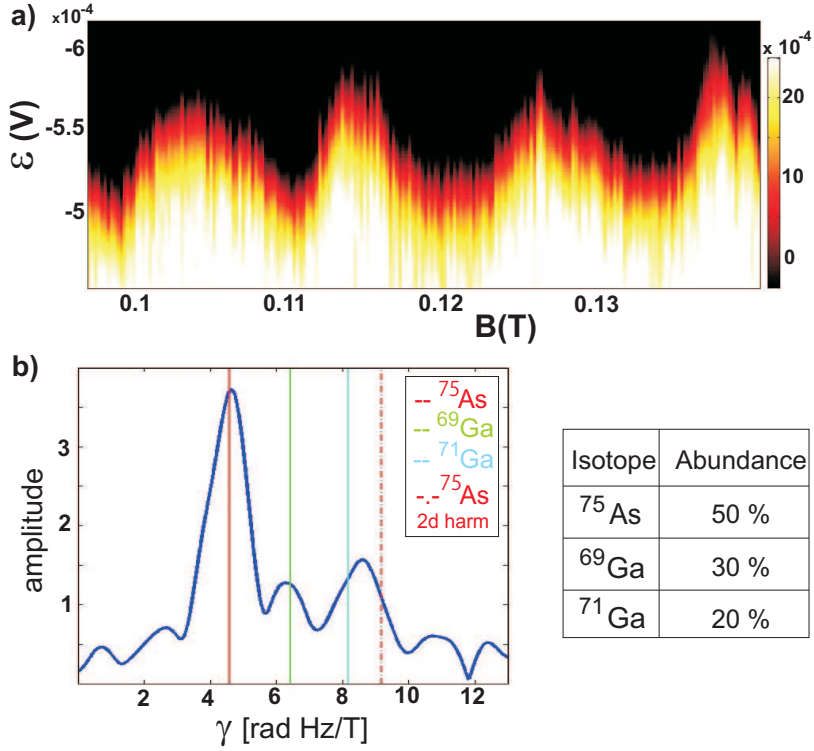


Figure 8.3: a) Detailed measurement of the position of the  $S-T_+$  transition as a function of  $\epsilon$  and  $B_{ext}$  ( $t_M=12\ \mu\text{s}$ ). b) Fourier transform of detailed measurements. The red, green and blue lines indicate the tabulated value for the gyromagnetic factor of the three isotopes  $^{75}\text{As}$ ,  $^{69}\text{Ga}$  and  $^{71}\text{Ga}$  [65]. Since the resolution in Fourier space is low, the peak corresponding to  $^{71}\text{Ga}$  is not clearly distinguishable from the second harmonic of  $^{75}\text{As}$  (dotted red line). The table lists the abundance of each species.

nuclei is also consistent with their relative abundance inside GaAs [65]. We can conclude that within the error bars of the measurement, the nuclei of all three species are polarized with similar efficiency.

#### 8.4.2 Variation of the probing time

When changing the probing time while  $t_M$  is kept fix to  $12\ \mu\text{s}$ , we observed a change in the amplitude of the oscillations. The maximal amplitude is measured for  $t_P = 100\ \text{ns}$ . At short times the effect vanishes. One possible reason is that the probing time in this case is comparable or shorter than the typical mixing time needed for an  $S-T_+$  transition.

The decrease in amplitude at longer times may indicate that the longer dwell times with a disappearance of the oscillations at about 300 ns introduces a third important time scale. The first two time scales mentioned are the  $S-T_+$  mixing time ( $\approx 10$  ns) and the nuclear Larmor precession time ( $\approx 1 \mu\text{s}$  at 100 mT). This third time scale maybe the decoherence or relaxation time at the  $S-T_+$  transition. Theoretical and experimental effort for further investigations are planned.

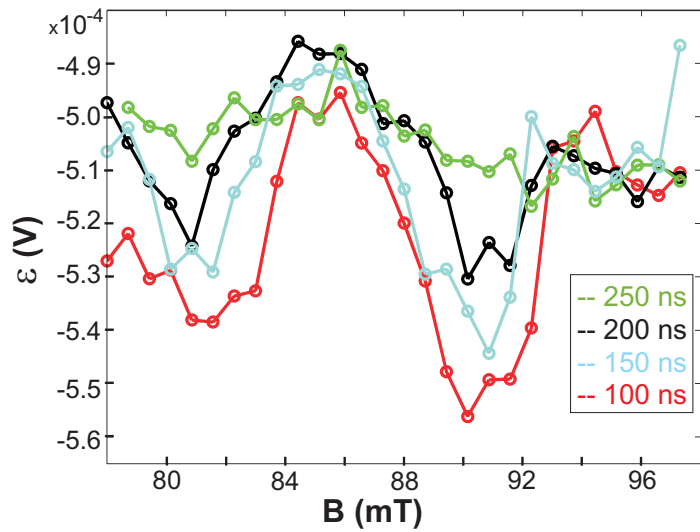


Figure 8.4: Position of the  $S-T_+$  transition as a function of  $\epsilon$  and  $B_{ext}$  measured with different probing times. The amplitude changes, being maximal for 100 ns and decreasing for longer times as well as shorter ones (not shown here).

## 8.5 Conclusions

In conclusion, we have shown that a periodically driven single pair of electrons through the  $S-T_+$  transition in a GaAs double quantum dot induces dynamic polarization of the underlying nuclei. The pumping cycle is most efficient when the cycle time corresponds to a multiple of the nuclear Larmor precession time. The gyromagnetic factor of all three nuclear species ( $^{75}\text{As}$ ,  $^{69}\text{Ga}$  and  $^{71}\text{Ga}$ ) extracted from the measurements confirmed the

partial polarization of all three isotopes. We have also shown that the probing time directly influences the amplitude of the polarization, with a peak at  $t_P = 100$  ns. The maximal polarization we have obtained is approximately 1 % of the total nuclear polarization, and its direction being opposite the external magnetic field corresponds to cooling of the nuclei. This indicates that we are now able to explore a new regime of coherent nuclear dynamics that has not been studied before.

## **Appendix A**

# **Double dot fabrication recipe**

The fabrication recipe presented in this appendix was developed and used at the Weizmann Institute of Science for the fabrication of the devices used in this thesis.

### **Preliminary preparation**

- Cover the wafer with photoresist S1805, soft bake for 2 min and cut it with a scribe: debris from cutting stick permanently to the GaAs wafer and cannot be removed with sonication.
- Remove resist with acetone and methanol.

### **Mesa**

- Clean the wafer with TCA, acetone and methanol for 5 min in each solvent, on a hot plate at 100 °C, in Petri-dishes. Careful! the flash point of acetone is *below* 100 °C.
- Spin photoresist S1805 for 40 s at 5000 rpm.
- Soft bake the resist on a hot plate at 80 °C for 5 min. Let the wafer cool before proceeding.

- In the mask aligner, expose the wafer for 5 s.
- Develop in MF-319 for 9 s, rinse in water and blow dry.
- Hard bake at 100 °C for 5 min.
- Check the pattern under an optical microscope.
- Clean the optical mask in a resist stripper solution for 5 min and rinse with water.

### **Mesa etching**

- Wet etch of the mesa (the rate is approximately 860 Å/min), rinse in water and blow dry. Etching solution is 200 mL of water, 4 mL H<sub>2</sub>O<sub>2</sub>, 4 mL H<sub>3</sub>PO<sub>4</sub> in a 250 mL beaker.
- Wash off the resist with acetone and methanol for 5 min each on a hot plate at 100 °C.
- Measure the height of the mesa with a profilometer.

### **Ohmic contacts**

- Clean the wafer in TCA (5 min hot) and methanol (5 min hot) and blow dry.
- Clean the wafer in acetone (5 min hot) and methanol (5 min hot) and blow dry.
- Spin image reversal AZ-5214E for 40 s at 5000 rpm.
- Soft bake the resist for 45 s at 100 °C, let it cool and clean the edges and the back side of the wafer using a q-tip with acetone.
- Align the wafer to the mask and expose for 5 s.
- Hard bake for 45 s at 120 °C with *vacuum* (and let cool).

- Flood expose (i.e. expose without mask) for 1.3 min.
- Develop in AZ-726 for 22 s, then flush in water and blow dry.
- UV-ozone at 67 °C for 5 min to remove residues of organic resist.
- Clean the optical mask in a resist stripper solution for 5 min and rinse with water.

### **Ohmic contact evaporation**

- HCl-dip (HCl:H<sub>2</sub>O 1:1) for 20 s, flush quickly with water, blow dry, mount in the evaporator and pump as quickly as possible.
- Evaporation in a thermal evaporator: Ni 50 Å (rate: 0.06 Å/s), Au 2000 Å (rate: 0.3 Å/s), Ge 1000 Å (rate: 0.25 Å/s), Ni 750 Å (rate: 0.2 Å/s).
- Lift-off in warm acetone.
- Rapid thermal annealing (RTA) in forming gas (Ar/H<sub>2</sub>): 150 °C for 60 s , 330 °C for 40 sec, ramp to 460 °C in 10 sec , 460 °C for 50 sec.

### **E-beam gates**

- Spin the first layer of PMMA: 200 K 3% for 1 min at 5000 rpm.
- Bake the sample in the oven at 180 °C for 1 h.
- Spin the second layer of PMMA: 495 K 5% for 1 min at 8000 rpm.
- Bake the sample in the oven at 180 °C for 1 h.
- After e-beam writing, develop in MIBK:IPA 1:3 for 1 min and rinse in IPA.

- Standard recipe for evaporation in an e-gun evaporator: PdAu 150 Å(rate: 0.7 Å/s), Au 150 Å(rate: 1.5 Å/s)
- Lift-off in warm acetone.

### **Optical gates**

- Clean the wafer in acetone (5 min hot) and methanol (5 min hot) and blow dry.
- Spin image reversal AZ-5214E for 40 s at 5000 rpm.
- Soft bake for 45 s at 100 °C (let cool).
- Align the wafer to the mask and expose for 3 s.
- Hard bake for 45 s at 120 °C with vacuum.
- Flood expose for 1.3 min.
- Develop in AZ-726 for 22 s and then flush in water and blow dry.
- UV-ozone at 67 °C for 5 min.
- Clean the optical mask in a resist stripper solution for 5 min and rinse.

### **Optical gates evaporation**

- NH<sub>4</sub>OH dip (1:20) for 6 sec, flush quickly with water, blow dry, mount in the evaporator and pump as quickly as possible.
- Evaporation in a thermal evaporator: Ti 250 Å(rate: 0.1 Å/s), Au 2000 Å(rate: 0.25-0.35 Å/s).
- Lift-off in warm acetone.

## Appendix B

# Double dot tuning procedure

We present here a step-by-step recipe to tune the double quantum dot. One of the difficulties is that almost each gate influences the electrostatics of the whole dot, so that compensation with the other gates may be required.

- Once cooled to base temperature, the double quantum dot is ready to be tuned. The first step is to determine the depletion and pinch-off of the different gates pairwise (for example nose and tail, then nose and pL, nose and GL and so on). Then apply a voltage close to the depletion voltage to pL, tail and pR. On nose, GL and GR apply voltages near pinch-off (see Fig. B.1a for gate definitions).
- Apply a  $V_{SD}$  of 10  $\mu$ V across the dot and set up a two dimensional scan monitoring the conductance through the dot as a function of voltages on GR and GL (set voltage changes over a range of several tens of mV). When the tunnel barriers between the dot and source and the dot and drain are almost pinched off and with similar transmissions, you should observe Coulomb blockade peaks (see Fig. B.1b). If the dot conductance is still too high, apply a larger negative voltage (“close”) to nose, GL and GR.

- In the region in gate space where the Coulomb blockade peaks are hardly visible, start to monitor the conductance through the QPC. This is done in the following way: apply a voltage to the QPC gate such that the conductance through the QPC is about half the conductance quantum  $G_0 = \frac{2e^2}{h}$ , i.e. about half way on the first conductance step. Assuming GL is the second gate defining the QPC (see Fig. B.1), you need to compensate its voltage change during the 2D scan with the QPC gate to keep the QPC conductance constant. For this reason it is better to sweep GR and step GL. If the QPC near GR is used, the opposite applies. In any case, one detecting QPC at the time suffices. Details about the measurement circuits are illustrated in Chap. 4.
- You are now ready to create the double quantum dot by closing tail, pL and pR while monitoring  $G_{QPC}$  with 2D scans of GL and GR. As the double dot is formed, the boundaries delimiting different charge configuration regions assume honeycomb-like shapes (as introduced in Chap. 2) and current through the dot flows only at the triple points. As the voltages on the two plunger gates ( $V_{GL}$  and  $V_{GR}$ ) are made more negative the dot is emptied. The (0,0) charge state is reached when no more jumps in  $\frac{dG_{qpc}}{dGR}$  are measured for large changes in gate voltages.
- Once you identified the (0,2)–(1,1) or the (2,0)–(1,1) charge transition, adjust the tunnel barrier transparencies by playing with the voltages on all the gates (GL, GR, nose, tail, pL and pR). Appropriate tuning is reached when the tunneling rates from the right and left dots to the leads,  $\Gamma_R$  and  $\Gamma_L$ , are approximately the same. To determine this, measure the current at the triple points and keep it to about 1 pA (which corresponds to a tunneling rate just larger than 10 MHz) when applying a

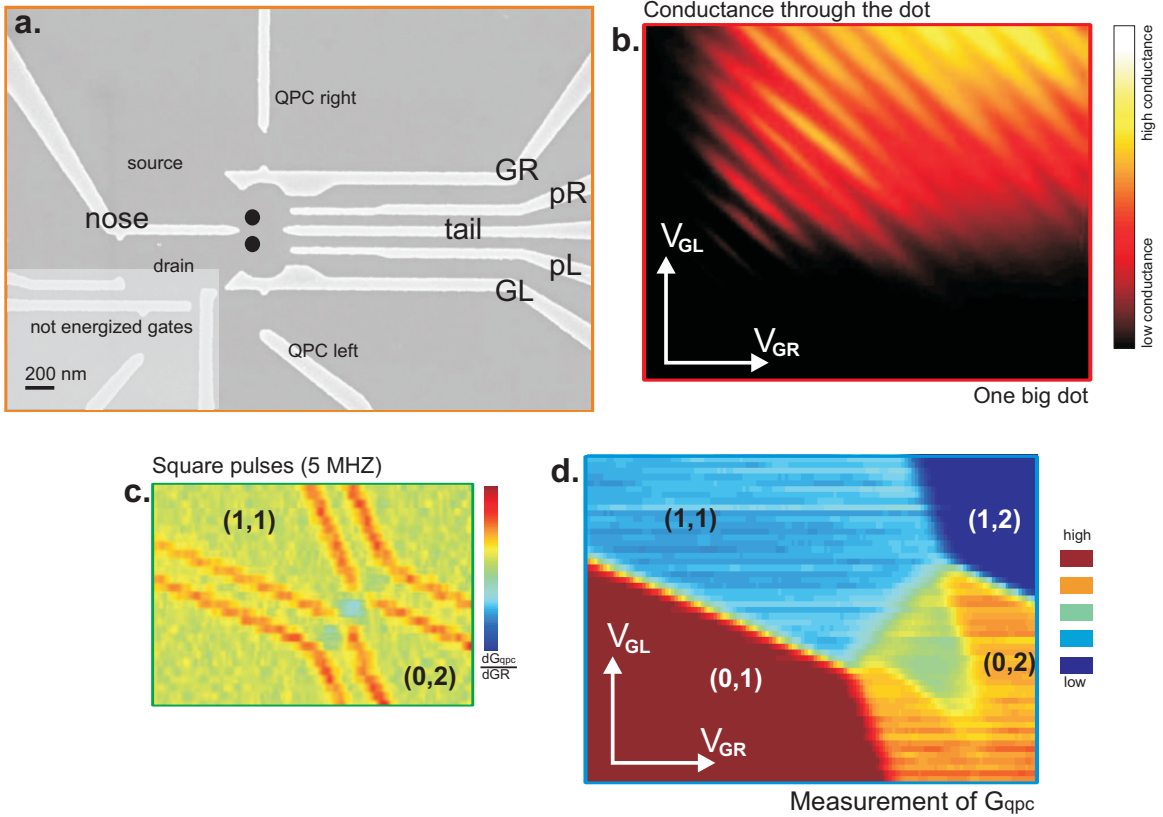


Figure B.1: a) SEM micrograph of the sample with labeling if the different gates. b) Transport measurement through the double quantum dot structure. The two dots are in the limit of one single dot. c) Two replicas of the charge stability diagram when applying square pulses to GR and GL. d) Spin blockade triangle.

forward source-drain bias of about  $400 \mu\text{V}$ . Forward source-drain bias induces the electrons to cycle from  $(0, 2)$  to  $(1, 1)$  to  $(0, 1)$ . The barriers have similar transparencies when the triple point biased triangles are uniform. Monitor also  $G_{QPC}$  and make sure that the charge signal at each triple point corresponds to the average of the charge signals of the three charge states surrounding the particular triple point.

- Determine the singlet-triplet energy difference at  $B_{\text{ext}} = 100 \text{ mT}$ : apply 100–500  $\mu\text{V}$  reverse source-drain bias ( $(0, 1) \rightarrow (1, 1) \rightarrow (0, 2)$ ) and measure for what value of  $V_{SD}$  the spin blockade is lifted.
- To calibrate the RF voltage applied to the gates, use the square pulses generated by

the AWG at a frequency of 1–5 MHz. When square pulses are applied to the gates, one obtains two replicas of the charge stability diagram shifted diagonally one from the other by the voltage applied to the gates (see Fig. B.1c). The ratio between this shift in voltage and the AWG output is the attenuation of the RF lines. Calibrate the conversion factors for the two gates separately, by applying square pulses first only to GR and then only to GL.

- During manipulations,  $V_{SD}$  across the double dot is kept at zero. The charge configuration is determined with lock-in measurements of the QPC conductance ( $I_{QPC} = 1 - 5$  nA, applied as shown in Fig. 4.2) or reflectometry measurements (as introduced in Chap. 4). The final check is the measurement of the spin-blockade triangle in the (0,2) charge configuration using the pulse cycle introduced in Chap. 2. At this point you are ready to take data.

# Bibliography

- [1] D. DiVincenzo, <http://mitworld.mit.edu/video/411>.
- [2] R. P. Feynman, *Simulating physics with computers*, International Journal of Theoretical Physics **21**, 467 (1982).
- [3] S. Lloyd, *Quantum information matters*, Science **319**, 1209 (2008).
- [4] C. H. Bennett and G. Brassard, *Quantum cryptography: public key distribution and coin tossing*, in *Proceedings of IEEE International Conference on Computers, Systems and Signal Processing*, 175 (1984).
- [5] G. Burkard, *Quantum Computation and Communication using Electron Spins in Quantum Dots and Wires* (PhD thesis, University of Basel, 2001).
- [6] P. W. Shor, *Algorithms for quantum computation: Discrete log and factoring*, Proceedings of the 25th Annual Symposium on Foundations of Computer Science (1994).
- [7] L. K. Grover, *A fast quantum mechanical algorithm for database search*, in *Proceedings of 28th Annual ACM Symposium on Theory of Computing (STOC)*, 212 (1996).
- [8] G. K. Brennen, C. M. Caves, P. S. Jessen, and I. H. Deutsch, *Quantum logic gates in optical lattices*, Phys. Rev. Lett. **82**, 1060 (1998).
- [9] L. M. K. Vandersypen, M. Steffen, G. Breyta, C. S. Yannoni, M. H. Sherwood, and I. L. Chuang, *Experimental realization of Shor's quantum factoring algorithm using nuclear magnetic resonance*, Nature **414**, 883 (2001).
- [10] L. Childress, M. V. Gurudev Dutt, J. M. Taylor, A. S. Zibrov, F. Jelezko, J. Wrachtrup, P. R. Hemmer, and M. D. Lukin, *Coherent dynamics of coupled electron and nuclear spin qubits in diamond*, Science **314**, 281 (2006).
- [11] I. Chiorescu, Y. Nakamura, C. J. P. M. Harmans, and J. E. Mooij, *Coherent quantum dynamics of a superconducting flux qubit*, Science **299**, 1869 (2003).
- [12] D. Loss and D. P. DiVincenzo, *Quantum computation with quantum dots*, Phys. Rev. A **57**, 120 (1998).
- [13] J. R. Petta, A. C. Johnson, J. M. Taylor, E. A. Laird, A. Yacoby, M. D. Lukin, C. M. Marcus, M. P. Hanson, and A. C. Gossard, *Coherent manipulation of coupled electron spins in semiconductor quantum dots*, Science **309**, 2180 (2005).

- [14] L. Cywinski, W. M. Witzel, and S. Das Sarma, *Pure quantum dephasing of a solid-state electron spin qubit in a large nuclear spin bath coupled by long-range hyperfine mediated interactions*, Phys. Rev. B **79**, 245314 (2009).
- [15] D. DiVincenzo, *The physical implementation of quantum computation*, Fortschr. Phys. **48**, 771 (2000).
- [16] M. Nielsen and I. Chuang, *Quantum Computation and Quantum Information* (Cambridge University Press, 2000).
- [17] P. W. Shor, *Scheme for reducing decoherence in quantum computer memory*, Phys. Rev. A **52**, 2493 (1995).
- [18] A. M. Steane, *Error correcting codes in quantum theory*, Phys. Rev. Lett. **77**, 793 (1996).
- [19] C. P. Slichter, *Principles of magnetic resonance* (Springer, 1990).
- [20] J. H. Davies, *The physics of low-dimensional semiconductors* (Cambridge University Press, 1998).
- [21] A. Yacoby, *Interference and dephasing by electron-electron interactions in the ballistic transport regime* (PhD thesis, Weizmann Institute of Science, 1995).
- [22] A. C. Johnson, *Charge Sensing and Spin Dynamics in GaAs Quantum Dots* (PhD thesis, Harvard University, 2005).
- [23] L. P. Kouwenhoven, *Transport of electron-waves and single-charges in semiconductor nanostructures* (PhD thesis, Delft University of Technology, 1992).
- [24] M. Ciorga, A. S. Sachrajda, P. Hawrylak, C. Gould, P. Zawadzki, S. Jullian, Y. Feng, and Z. Wasilewski, *Addition spectrum of a lateral dot from Coulomb and spin-blockade spectroscopy*, Phys. Rev. B **61**, R16315 (2000).
- [25] S. Tarucha, D. G. Austing, T. Honda, R. J. van der Hage, and L. P. Kouwenhoven, *Shell filling and spin effects in a few electron quantum dot*, Phys. Rev. Lett. **77**, 17 (1996).
- [26] T. Ihn, *Electronic Quantum Transport in Mesoscopic Semiconductor Structures* (Springer, 2003).
- [27] L. P. Kouwenhoven, C. M. Marcus, P. L. McEuen, S. Tarucha, R. M. Westervelt, and N. S. Wingreen, *Electron transport in quantum dots*, in *Mesoscopic Electron Transport* (Kluwert, 1997).
- [28] W. G. van der Wiel, S. De Franceschi, J. M. Elzerman, T. Fujisawa, S. Tarucha, and L. P. Kouwenhoven, *Electron transport through double quantum dots*, Rev. Mod. Phys **75**, 1 (2003).
- [29] N. Ashcroft and N. Mermin, *Solid state physics* (Harcourt College Publisher, 1976).
- [30] D. D. Awschalom, D. Loss, and N. Samarth, *Semiconductor spintronics and quantum computation* (Springer, 2002).

- [31] L. P. Kouwenhoven, D. G. Austing, and S. Tarucha, *Few-electron quantum dots*, Rep. Prog. Phys. **64**, 701 (2001).
- [32] A. C. Johnson, J. R. Petta, C. M. Marcus, M. P. Hanson, and A. C. Gossard, *Singlet-triplet spin blockade and charge sensing in a few-electron double quantum dot*, Phys. Rev. B **72**, 165308 (2005).
- [33] A. C. Johnson, J. R. Petta, J. M. Taylor, A. Yacoby, M. D. Lukin, C. M. Marcus, M. P. Hanson, and A. C. Gossard, *Triplet-singlet spin relaxation via nuclei in a double quantum dot*, Nature **435**, 925 (2005).
- [34] F. H. L. Koppens, J. A. Folk, J. M. Elzerman, R. Hanson, L. H. Willems van Beveren, I. T. Vink, H. P. Tranitz, W. Wegscheider, L. P. Kouwenhoven, and L. M. K. Vandersypen, *Control and detection of singlet-triplet mixing in a random nuclear field*, Science **309**, 1346 (2005).
- [35] B. J. van Wees, H. van Houten, C. W. J. Beenakker, J. G. Williamson, L. P. Kouwenhoven, D. van der Marel, and C. T. Foxon, *Quantized conductance of point contacts in a two-dimensional electron gas*, Phys. Rev. Lett. **60**, 848 (1988).
- [36] M. Field, C. G. Smith, M. Pepper, D. A. Ritchie, J. E. F. Frost, G. A. C. Jones, and D. G. Hasko, *Measurements of Coulomb blockade with a noninvasive voltage probe*, Phys. Rev. Lett. **70**, 1311 (1993).
- [37] B. E. Kane, N. S. McAlpine, A. S. Dzurak, R. G. Clark, G. J. Milburn, H. B. Sun, and H. Wiseman, *Single-spin measurement using single-electron transistors to probe two-electron systems*, Phys. Rev. B **61**, 2961 (2000).
- [38] D. Sprinzak, Y. Ji, M. Heiblum, D. Mahalu, and H. Shtrikman, *Charge distribution in a Kondo-correlated quantum dot*, Phys. Rev. Lett. **88**, 176805 (2002).
- [39] J. Levy, *Universal quantum computation with spin-1/2 pairs and Heisenberg exchange*, Phys. Rev. Lett. **89**, 147902 (2002).
- [40] D. A. Lidar, I. L. Chuang, and K. B. Whaley, *Decoherence-free subspace for quantum computation*, Phys. Rev. Lett. **81**, 2594 (1998).
- [41] J. M. Taylor, H.-A. Engel, W. Dür, A. Yacoby, C. M. Marcus, P. Zoller, and M. D. Lukin, *Fault-tolerant architecture for quantum computation using electrically controlled semiconductor spins*, Nature Physics **1**, 177 (2005).
- [42] G. Salis, Y. Kato, K. Ensslin, D. C. Driscoll, A. C. Gossard, and D. D. Awschalom, *Electrical control of spin coherence in semiconductor nanostructures*, Nature **414**, 619 (2001).
- [43] M. Pioro-Ladriere, T. Obata, Y. Tokura, Y. S. Shin, T. Kubo, K. Yoshida, T. Taniyama, and S. Tarucha, *Electrically driven single electron spin resonance in a slanting Zeeman field*, Nature Physics **4**, 776 (2008).
- [44] K. Yosida, *Theory of magnetism* (Springer, 1998).
- [45] D. Paget, G. Lampel, B. Sapoval, and V. I. Safarov, *Low field electron-nuclear spin coupling in gallium arsenide under optical pumping conditions*, Phys. Rev. B **15**, 5780 (1977).

- [46] J. M. Taylor, J. R. Petta, A. C. Johnson, A. Yacoby, C. M. Marcus, and M. D. Lukin, *Relaxation, dephasing, and quantum control of electron spins in double quantum dots*, Phys. Rev. B **76**, 035315 (2007).
- [47] J. M. Taylor, *Electron spin and charge in semiconductor quantum dots* (PhD thesis, Harvard University, 2006).
- [48] J. J. Krich, *Electron and nuclear spins in semiconductor quantum dots* (PhD thesis, Harvard University, 2009).
- [49] J. R. Petta, J. M. Taylor, A. C. Johnson, A. Yacoby, M. D. Lukin, C. M. Marcus, M. P. Hanson, and A. C. Gossard, *Dynamic nuclear polarization with single electron spins*, Phys. Rev. Lett. **100**, 067601 (2008).
- [50] H.-A. Engel, *private communication*.
- [51] R. Hanson, L. P. Kouwenhoven, J. R. Petta, S. Tarucha, and L. M. K. Vandersypen, *Spins in few-electron quantum dots*, Rev. Mod. Phys. **79**, 1217 (2007).
- [52] D. M. Zumbühl, J. B. Miller, C. M. Marcus, K. Campman, and A. C. Gossard, *Spin-orbit coupling, antilocalization, and parallel magnetic fields in quantum dots*, Phys. Rev. Lett. **89**, 276803 (2002).
- [53] A. Messiah, *Quantum mechanics* (Dover publications, Inc., 1999).
- [54] L. Cywinski, W. M. Witzel, and S. Das Sarma, *Electron spin dephasing due to hyperfine interactions with a nuclear spin bath*, Phys. Rev. Lett. **102**, 057601 (2009).
- [55] I. T. Vink, *Manipulation and Read-out of Spins in Quantum Dots* (PhD thesis, Delft University of Technology, 2008).
- [56] C. Deng and X. Hu, *Analytical solution of electron spin decoherence through hyperfine interaction in a quantum dot*, Phys. Rev. B **73**, 241303R (2006).
- [57] K. C. Nowack, *Electrical Manipulation and Detection of Single Electron Spins in Quantum Dots* (PhD thesis, Delft University of Technology, 2009).
- [58] R. G. Shulman, B. J. Wyluda, and H. J. Hrostowski, *Nuclear magnetic resonance in semiconductors*, Phys. Rev. **109**, 808 (1958).
- [59] A. V. Khaetskii, D. Loss, and L. Glazman, *Electron spin decoherence in quantum dots due to interaction with nuclei*, Phys. Rev. Lett. **88**, 186802 (2002).
- [60] E. L. Hahn, *Spin echoes*, Phys. Rev. **80**, 580 (1950).
- [61] H. Y. Carr and E. M. Purcell, *Effects of diffusion on free precession in nuclear magnetic resonance experiments*, Phys. Rev. **94**, 630 (1954).
- [62] S. Meiboom and D. Gill, *Modified spin-echo method for measurement of relaxation times*, Rev. Sci. Instrum. **29**, 6881 (1958).
- [63] [http://microchemicals.net/technical\\_information/image\\_reversal\\_resists.pdf](http://microchemicals.net/technical_information/image_reversal_resists.pdf).

- [64] P. Rabinzhon, M. Kobayashi, S. Goto, M. Kawata, and T. Usagawa, *On the determination of the specific contact resistance of alloyed contacts to n-GaAs*, J. Journal of Appl. Phys. **29**, 1896 (1990).
- [65] <http://www.webelements.com>.
- [66] I. Neder, *private communication*.
- [67] C. Barthel, D. J. Reilly, C. M. Marcus, M. P. Hanson, and A. C. Gossard, *Rapid single-shot measurement of a singlet-triplet qubit*, Phys. Rev. Lett. **103**, 160503 (2009).
- [68] C. Buizert, F. H. L. Koppens, M. Pioro-Ladriere, H. Tranitz, I. T. Vink, S. Tarucha, W. Wegscheider, and L. M. K. Vandersypen, *Insitu reduction of charge noise in GaAs/Al<sub>x</sub>Ga<sub>1-x</sub>As Schottky-gated devices*, Phys. Rev. Lett. **101**, 226603 (2008).
- [69] G. Frossati, *private communication*.
- [70] D. M. Pozar, *Microwave engineering* (John Wiley & Sons, Inc., 1998).
- [71] L. Di Carlo, *Mesoscopic electronics beyond DC transport* (PhD thesis, Harvard University, 2007).
- [72] F. Pobel, *Matter and methods at low temperatures* (Springer, 1992).
- [73] J. H. Love, *Resolved dynamics of single electron tunneling using the RF-SET* (PhD thesis, Yale University, 2007).
- [74] L. J. Taskinen, R. P. Starrett, T. P. Martin, A. P. Micolich, A. R. Hamilton, M. Y. Simmons, D. A. Ritchie, and M. Pepper, *Radio-frequency reflectometry on large gated two-dimensional systems*, Rev. Sci. Inst. **79**, 123901 (2008).
- [75] R. J. Schoelkopf, P. Wahlgren, A. A. Kozhevnikov, P. Delsing, and D. E. Prober, *The radio-frequency single-electron transistor (RF-SET): a fast and ultrasensitive electrometer*, Science **280**, 1238 (1998).
- [76] D. J. Reilly, C. M. Marcus, M. P. Hanson, and A. C. Gossard, *Fast single-charge sensing with a RF quantum point contact*, Appl. Phys. Lett. **91**, 162101 (2007).
- [77] M. C. Cassidy, A. S. Dzurak, R. G. Clark, K. D. Petersson, I. Farrer, D. A. Ritchie, and C. G. Smith, *Single shot charge detection using a radio-frequency quantum point contact*, Appl. Phys. Lett. **91**, 222104 (2007).
- [78] R. Brenner, T. M. Buehler, and D. J. Reilly, *Radio-frequency operation of a double-island single-electron transistor*, J. Appl. Phys. **97**, 034501 (2005).
- [79] J. D. Teufel, *Superconducting Tunnel Junctions as Direct Detectors for Submillimeter Astronomy* (PhD thesis, Yale University, 2007).
- [80] U. Kemiktarak, T. Ndukum, K. C. Schwab, and K. L. Ekinci, *Radio-frequency scanning tunneling microscopy*, Nature **450**, 85 (2007).
- [81] S. Foletti, H. Bluhm, D. Mahalu, V. Umansky, and A. Yacoby, *Universal quantum control in two-electron spin quantum bits using dynamic nuclear polarization*, Nature Physics **5**, 903 (2009).

- [82] W. A. Coish and D. Loss, *Exchange-controlled single-electron-spin rotations in quantum dots*, Phys. Rev. B **75**, 161302 (2007).
- [83] D. Press, T. D. Ladd, B. Zhang, and Y. Yamamoto, *Complete quantum control of a single quantum dot spin using ultrafast optical pulses*, Nature **456**, 218 (2008).
- [84] D. Aharonov and M. Ben-Or, *Fault-tolerant quantum computation with constant error rate* (1999), arXiv:9906129v1.
- [85] I. A. Merkulov, A. L. Efros, and M. Rosen, *Electron spin relaxation by nuclei in semiconductor quantum dots*, Phys. Rev. B **65**, 205309 (2002).
- [86] W. M. Witzel and S. Das Sarma, *Quantum theory for electron spin decoherence induced by nuclear spin dynamics in semiconductor quantum computer architecture*, Phys. Rev. B **74**, 035322 (2006).
- [87] W. Zhang, V. Dobrovitski, K. Al-Hassanieh, E. Dagotto, and B. Harmon, *Hyperfine interaction induced decoherence of electron spins in quantum dots*, Phys. Rev. B **74**, 205313 (2006).
- [88] D. J. Reilly, J. M. Taylor, J. Petta, C. M. Marcus, M. P. Hanson, and A. C. Gossard, *Suppressing spin qubit dephasing by nuclear state preparation*, Science **321**, 817 (2008).
- [89] D. J. Reilly, J. M. Taylor, J. Petta, C. M. Marcus, M. P. Hanson, and A. C. Gossard, *Exchange control of nuclear spin diffusion in double quantum dots* (2008).
- [90] D. J. Reilly, *Private communication*.
- [91] E. A. Laird, J. R. Petta, A. C. Johnson, C. M. Marcus, A. Yacoby, M. P. Hanson, and A. C. Gossard, *Effect of exchange interaction on spin dephasing in a double quantum dot*, Phys. Rev. Lett. **97**, 056801 (2006).
- [92] M. Stopa, J. J. Krich, and A. Yacoby, *Inhomogeneous nuclear spin flips* (2009), arXiv:0905.4520v1.
- [93] P. Maletinsky, A. Badolato, and A. Imamoglu, *Dynamics of quantum dot nuclear spin polarization*, Phys. Rev. Lett. **99**, 056804 (2007).
- [94] A. Greilich, S. E. Economou, S. Spatzek, D. R. Yakovlev, D. Reuter, A. D. Wieck, T. L. Reinecke, and M. Bayer, *Ultrafast optical rotations of electron spins in quantum dots*, Nature Physics **5**, 262 (2009).
- [95] F. H. L. Koppens, C. Buizert, K. J. Tielrooij, I. T. Vink, K. C. Nowack, T. Meunier, L. P. Kouwenhoven, and L. M. K. Vandersypen, *Driven coherent oscillations of a single electron spin in a quantum dot*, Nature **442**, 766 (2006).
- [96] K. C. Nowack, F. H. L. Koppens, Y. V. Nazarov, and L. M. K. Vandersypen, *Coherent control of a single electron spin with electric fields*, Science **318**, 1430 (2007).
- [97] W. Yao, R. B. Liu, and L. J. Sham, *Theory of electron spin decoherence by interacting nuclear spins in a quantum dot*, Phys. Rev. B **74**, 195301 (2006).
- [98] L. Cywinski, W. M. Witzel, and S. Das Sarma, *Electron spin dephasing due to hyperfine interactions with a nuclear spin bath*, Phys. Rev. Lett. **102**, 057601 (2009).

- [99] W. A. Coish, J. Fischer, and D. Loss, *Exponential decay in a spin bath*, Phys. Rev. B **77**, 125329 (2008).
- [100] H. Bluhm, S. Foletti, D. Mahalu, V. Umansky, and A. Yacoby, *Enhancing the coherence of spin qubits by narrowing the nuclear spin bath with a quantum feedback loop* (2010), (submitted to Phys. Rev. Lett.).
- [101] T. D. Ladd, D. Maryenko, Y. Yamamoto, E. Abe, and K. M. Itoh, *Coherence time of decoupled nuclear spins in silicon*, Phys. Rev. B **71**, 014401 (2005).
- [102] A. M. Tyryshkin, S. A. Lyon, A. V. Astashkin, and A. M. Raitsimring, *Electron spin relaxation times of phosphorus donors in silicon*, Phys. Rev. B **68**, 193207 (2003).
- [103] J. M. Elzerman, R. Hanson, L. H. Willems van Beveren, B. Witkamp, L. M. K. Vandersypen, and L. P. Kouwenhoven, *Single-shot read-out of an individual electron spin in a quantum dot*, Nature **430**, 431 (2004).
- [104] J. Fischer, W. A. Coish, D. V. Bulaev, and D. Loss, *Spin decoherence of a heavy hole coupled to nuclear spins in a quantum dot*, Phys. Rev. B **78**, 155329 (2008).
- [105] S. Takahashi, R. Hanson, J. van Tol, M. S. Sherwin, and D. D. Awschalom, *Quenching spin decoherence in diamond through spin bath polarization*, Phys. Rev. Lett. **101**, 047601 (2008).
- [106] W. A. Coish and D. Loss, *Hyperfine interaction in a quantum dot: Non-markovian electron spin dynamics*, Phys. Rev. B **70**, 195340 (2004).
- [107] D. Klauser, W. A. Coish, and D. Loss, *Nuclear spin state narrowing via gate-controlled Rabi oscillations in a double quantum dot*, Phys. Rev. B **73**, 205302 (2006).
- [108] I. T. Vink, K. C. Nowack, F. H. L. Koppens, J. Danon, Y. V. Nazarov, and L. M. K. Vandersypen, *Locking electron spins into magnetic resonance by electron-nuclear feedback*, Nature Physics **5**, 764 (2009).
- [109] X. Xu, W. Yao, B. Sun, D. G. Steel, A. S. Bracker, D. Gammon, and L. J. Sham, *Optically controlled locking of the nuclear field via coherent dark-state spectroscopy*, Nature **459**, 1105 (2009).
- [110] C. Latta, A. Högele, Y. Zhao, A. N. Vamivakas, P. Maletinsky, M. Kroner, J. Dreiser, I. Carusotto, A. Badolato, D. Schuh, W. Wegscheider, M. Atatüre, and A. Imamoglu, *Confluence of resonant laser excitation and bi-directional quantum dot nuclear spin polarization*, Nature Physics **5**, 758 (2009).
- [111] A. Greilich, A. Shabaev, D. R. Yakovlev, A. L. Efros, D. R. I. A. Yugova, A. D. Wieck, and M. Bayer, *Nuclei-induced frequency focusing of electron spin coherence*, Science **317**, 1896 (2007).
- [112] J. Danon, I. T. Vink, F. H. L. Koppens, K. C. Nowack, L. M. K. Vandersypen, and Y. V. Nazarov, *Multiple nuclear polarization states in a double quantum dot*, Phys. Rev. Lett. **103**, 046601 (2009).
- [113] M. S. Rudner and L. S. Levitov, *Resonant cooling of nuclear spins in quantum dots*, arXiv:0705.2177v1.

- [114] C. Barthel, J. Medford, H. Bluhm, A. Yacoby, C. M. Marcus, M. P. Hanson, and A. C. Gossard, *Singlet-triplet qubit relaxation and initialization in a magnetic field gradient*, in preparation.
- [115] D. J. Reilly, J. M. Taylor, E. A. Laird, J. R. Petta, C. M. Marcus, M. P. Hanson, and A. C. Gossard, *Measurement of temporal correlations of the Overhauser field in a double quantum dot*, Phys. Rev. Lett. **101**, 236803 (2008).
- [116] M. Gullans, J. J. Krich, J. M. Taylor, H. Bluhm, B. I. Halperin, C. M. Marcus, M. Stopa, A. Yacoby, and M. D. Lukin, *Dynamic nuclear polarization in double quantum dots* (2010), arXiv:1003.4508.
- [117] L. M. K. Vandersypen and I. L. Chuang, *NMR techniques for quantum control and computation*, Rev. Mod. Phys. **76**, 1037 (2004).
- [118] K. Khodjasteh and L. Viola, *Dynamically error-corrected gates for universal quantum computation*, Phys. Rev. Lett. **102**, 080501 (2009).
- [119] F. H. L. Koppens, K. C. Nowack, and L. M. K. Vandersypen, *Spin echo of a single spin in a quantum dot*, Phys. Rev. Lett. **100**, 236802 (2008).
- [120] A. Greilich, D. R. Yakovlev, A. Shabaev, A. L. Efros, I. A. Yugova, R. Oulton, V. Stavarache, D. Reuter, A. D. Wieck, and M. Bayer, *Mode locking of electrons spin coherence in singly charged quantum dots*, Science **313**, 341 (2006).
- [121] H. Bluhm, S. Foletti, I. Neder, M. S. Rudner, D. Mahalu, V. Umansky, and A. Yacoby, *Long coherence of electron spins coupled to a nuclear spin bath* (2010), (in preparation).
- [122] G. Chen, D. L. Bergman, and L. Balents, *Semiclassical dynamics and long-time asymptotics of the central-spin problem in a quantum dot*, Phys. Rev. B **76**, 045312 (2007).
- [123] W. M. Witzel and S. Das Sarma, *Multiple-pulse coherence enhancement of solid state spin qubits*, Phys. Rev. Lett. **98**, 077601 (2007).
- [124] K. Khodjasteh and D. A. Lidar, *Performance of deterministic dynamical decoupling schemes: Concatenated and periodic pulse sequences*, Phys. Rev. A **75**, 062310 (2007).
- [125] W. M. Witzel and S. Das Sarma, *Concatenated dynamical decoupling in a solid-state spin bath*, Phys. Rev. B **76**, 241303 (2007).
- [126] G. S. Uhrig, *Keeping a quantum bit alive by optimizing  $\pi$ -pulse sequences*, Phys. Rev. Lett. **98**, 100504 (2007).
- [127] B. Lee, W. M. Witzel, and S. Das Sarma, *Universal pulse sequence to minimize spin dephasing in the central spin decoherence problem*, Phys. Rev. Lett. **100**, 160505 (2008).
- [128] R. K. Sundfors, *Exchange and quadrupole broadening of nuclear acoustic resonance line shapes in the III-V semiconductors*, Phys. Rev. **185**, 458 (1969).
- [129] R. K. Hester, A. Sher, J. F. Soest, and G. Weisz, *Nuclear-magnetic-resonance detection of charge defects in gallium arsenide*, Phys. Rev. B **10**, 4262 (1974).

- [130] L. Viola, S. Lloyd, and E. Knill, *Universal control of decoupled quantum systems*, Phys. Rev. Lett. **83**, 4888 (1999).
- [131] S. Foletti, J. Martin, M. Dolev, D. Mahalu, V. Umansky, and A. Yacoby, *Observation of dynamic nuclear polarization using a single pair of electrons* (2010), (in preparation).
- [132] W. A. Coish and D. Loss, *Singlet-triplet decoherence due to nuclear spins in a double quantum dot*, Phys. Rev. B **72**, 125337 (2005).
- [133] S. I. Erlingsson, Y. V. Nazarov, and V. I. Fal'ko, *Nucleus-mediated spin-flip transitions in GaAs quantum dots*, Phys. Rev. B **64**, 195306 (2001).
- [134] A. Imamoglu, E. Knill, L. Tian, and P. Zoller, *Optical pumping of quantum-dot nuclear spins*, Phys. Rev. Lett. **91**, 017402 (2003).
- [135] C. W. Lai, P. Maletinsky, A. Badolato, and A. Imamoglu, *Knight-field-enabled nuclear spin polarization in single quantum dots*, Phys. Rev. Lett. **96**, 167403 (2006).
- [136] A. S. Bracker, E. A. Stinaff, D. Gammon, M. E. Ware, J. T. Tischler, A. Shabaev, A. L. Efros, D. Park, D. Gershoni, V. L. Korenev, and I. A. Merkulov, *Optical pumping of the electronic and nuclear spin of single charge-tunable quantum dots*, Phys. Rev. Lett. **94**, 047402 (2005).
- [137] M. S. Rudner, I. Neder, L. S. Levitov, and B. I. Halperin, *Phase-sensitive probes of nuclear polarization in spin-blockaded transport*, arXiv:0909.0060.
- [138] D. Weinmann, W. Haeusler, W. Pfaff, B. Kramer, and U. Weiss, *Spin blockade in non-linear transport through quantum dots*, Europhys. Lett. **26**, 467 (1994).
- [139] K. Ono, D. G. Austing, Y. Tokura, and S. Tarucha, *Current rectification by Pauli exclusion in a weakly coupled double quantum dot system*, Science **297**, 1313 (2002).
- [140] J. M. Elzerman, R. Hanson, L. H. Willems van Beveren, L. M. K. Vandersypen, and L. P. Kouwenhoven, *Excited-state spectroscopy on a nearly closed quantum dot via charge detection*, Appl. Phys. Lett. **84**, 4617 (2004).